

Supplementary Material for “Nonreciprocal Topological Phonon Transfer Independent of both Exceptional-Point Encircling Direction and Device Mass”

Deng-Gao Lai,^{1,2} Adam Miranowicz,^{1,3} and Franco Nori^{1,2,4}

¹Theoretical Quantum Physics Laboratory, Cluster for Pioneering Research, RIKEN Wako shi, Saitama 351-0198, Japan

²Physics Department, University of Michigan, Ann Arbor, Michigan 48109-1040, USA

³Institute of Spintronics and Quantum Information, Faculty of Physics, Adam Mickiewicz University, 61-614 Poznań, Poland

⁴RIKEN Center for Quantum Computing (RQC), 2-1 Hirosawa, Wako-shi, Saitama 351-0198, Japan

In this Supplementary Material, we present the detailed results on both mass-insensitive and speed-controllable one-way topological phonon transport, which is fully independent of the directions of the encirclement around the exceptional point (EP). Specifically, this document consists of three sections: (i) Effective non-Hermitian Hamiltonian and its EP; (ii) Topological-energy-transfer quality factor and unidirectional topological phononics independent of both the direction of the EP-including control loop and the mass of quantum device, which is enabled by the Fizeau light-dragging effect; (iii) Innovativeness, importance and timeliness of our proposal, (iv) Underlying physical mechanism of our work, (v) Detailed discussions on the experimental feasibility of the proposed physical model, and (vi) Application of our approach to non-Hermitian N -state systems and its combination with non-Abelian nature.

Contents

I. Effective non-Hermitian Hamiltonian of the system and its exceptional point	2
A. Effective non-Hermitian Hamiltonian	2
B. Exceptional point	7
II. One-way topological phononics independent of the encircling direction of the EP	9
A. Topological-energy-transfer quality factor	9
B. Unidirectional Topological control independent of the EP-encircling direction	10
C. Detailed comparison of standard and our methods	11
D. Speed-tunable topological phonon transfer	13
E. Topological energy transfer immune to device quality factors	15
F. Strength-dependent topological transfer of energy	18
G. Eigenvalue distributions and transient behaviors around EP for different laser powers	19
H. Temperature effect on the nonreciprocal topological phonon transfer	21
I. Clarifying the relationship between energy bands and topological phonon transfer	23
III. Innovativeness, importance and timeliness of our proposal	24
IV. Physical mechanism of our approach	24
A. Mechanism of light-induced vibrations	24
B. Underlying physics behind our results	25
V. Detailed discussions on experimental feasibility using realistic state-of-the-art experiments	31
A. Experimental feasibility analysis using realistic state-of-the-art experimental conditions	31
B. Detailed analysis of the “self-adjustment” effect	34
C. Detailed analysis of the microscopic-level forces	36
VI. Application of our approach to non-Hermitian N-state systems and its combination with non-Abelian nature	37
References	39

I. EFFECTIVE NON-HERMITIAN HAMILTONIAN OF THE SYSTEM AND ITS EXCEPTIONAL POINT

In this section, we derive in detail the equations of motion for the optical and phononic modes in a three-mode optomechanical system, which consists of two motional modes coupled to a common spinning optical cavity via radiation-pressure interactions [S1–S3]. We also detailedly calculate an effective Hamiltonian of our system by adiabatically eliminating the optical mode, and analyze an exceptional point (EP) of the physical system.

A. Effective non-Hermitian Hamiltonian

We here study the mass-tolerant and speed-tunable unidirectional topological transfer of energy between two vibrational normal modes using multi-vibration optomechanical platforms. Specifically, we analyze, as shown in Fig. 1(a) of the main text, a uniform optical mode is supported by a spinning silica microsphere with an external driving field, and the radiation-pressure effect leads to the coupling of the optical mode to the two vibrational modes [S1–S3]. To further control the optical degrees of freedom, a mechanical rotating is applied to the optical microsphere cavity, which is evanescently coupled to a tapered fiber. Note that such a mechanical-spinning device had been demonstrated to achieve one-way optical signals and quantum entanglement in recent experiments and proposals [S4–S9].

Let us detailedly consider a multimode optomechanical device, where a spinning silica-microsphere cavity coupled to two motions is positioned close to a tapered region of a single-mode telecommunication fibre. The evanescent coupling of the light into this spinning setup is caused by the tapered region of the fibre, and via the same coupler, the light can be coupled out through the other side of the fibre [S4]. Consequently, both input and output ports can be simultaneously served by each side of the fibre, and relying on the input port, the light circulates in the silica sphere in either clockwise or counter-clockwise direction, resulting in an optical mode a_R or a_L (with resonance frequencies $\omega_c^{R,L}$), respectively. Then, the Hamiltonian of the physical system associated with spinning reads (with $\hbar = 1$):

$$\mathcal{H} = \omega_c^{R,L} a_{R,L}^\dagger a_{R,L} + \sum_{j=1,2} [\omega_j b_j^\dagger b_j + g_j a_{R,L}^\dagger a_{R,L} (b_j^\dagger + b_j)] + \mathcal{H}_{\text{driv}}^{R,L}, \quad (\text{S1a})$$

$$\mathcal{H}_{\text{driv}}^{R,L} = i \sqrt{\kappa_{\text{in}}} \epsilon_{\text{in}} (a_{R,L}^\dagger e^{-i\omega_{R,L}t} - a_{R,L} e^{i\omega_{R,L}t}), \quad (\text{S1b})$$

where $a_{R,L}^\dagger$ ($a_{R,L}$) and b_j^\dagger (b_j) are, respectively, the creation (annihilation) operators of the optical mode (with optical resonance frequency $\omega_c^{R,L}$) and the j th vibrational mode (with vibrational resonance frequency ω_j). The light-vibration interactions between the optical mode and the two vibrational modes are described by the radiation-pressure-coupling g_j terms, with g_j being the strengths of single-excitation coupling rates. The term $\mathcal{H}_{\text{driv}}$ depicts the driving of the system, where $\epsilon_{\text{in}} = \sqrt{P/(\hbar\omega_{R,L})}$ is the driving-field amplitude of the optical mode, with P and $\omega_{R,L}$ being the power and frequency of the driving laser for the cavity, respectively. Experimentally, the aerodynamic process plays a vital role in fiber-resonator interactions in a rotating setup, which drags air into the region between the sphere and tapered fiber, yielding an air-lubrication layer in this region. The thin air film then lets the fiber fly at a few nanometres above the sphere. Owing to the “self-adjustment” process, the taper floats back to its initial position, once it is caused to rise higher than the stable-equilibrium height by any perturbation. The critical coupling of light into the silica sphere is enabled via the self-adjustment behavior, whereby an optical drag, identical in size but opposite in sign, is experienced by the countercirculating light (see the detailed deviations and analysis in Sec. V).

For conventional optomechanical devices consisting of an optical mode linearly coupled to a vibrational mode, a pair of coupled differential equations for both optical and vibrational modes are resulted from an input–output approach to these systems. Then, these equations of motion can be easily treated in the Fourier domain for better understand the optical modification of the vibrational susceptibilities. We here focus on a simple extension of these standard models, by considering two motional modes, each coupled to a common optical mode. Subsequently, this yields the following equations of motion for both optical and vibrational modes:

$$\dot{a}_{R,L} = -\left(\frac{\kappa}{2} + i\omega_c^{R,L}\right) a_{R,L} - ig_1 a_{R,L} z_1 - ig_2 a_{R,L} z_2 + \sqrt{\kappa_{\text{in}}} \epsilon_{\text{in}}, \quad (\text{S2a})$$

$$\dot{b}_1 = -\left(\frac{\gamma_1}{2} + i\omega_1\right) b_1 - ig_1 a_{R,L}^\dagger a_{R,L} + \sqrt{\gamma_1} \eta_1, \quad (\text{S2b})$$

$$\dot{b}_2 = -\left(\frac{\gamma_2}{2} + i\omega_2\right) b_2 - ig_2 a_{R,L}^\dagger a_{R,L} + \sqrt{\gamma_2} \eta_2, \quad (\text{S2c})$$

where the parameter κ is the dissipation rate corresponding to the linewidth, the parameter κ_{in} is the input coupling rate of the cavity field, and the position operate $z_j = b_j^\dagger + b_j$ describes the j th mechanical mode. In addition, the parameters ω_j , γ_j , and g_j denote the motional resonance frequency, mechanical dissipation rate, and single-photon coupling strength, respectively. The

optical and mechanical modes are, respectively, driven by input fields ϵ_{in} and η_j . The parameter $\omega_c^{R,L}$ denotes the effective optical resonance frequency experiencing the Sagnac-Fizeau shift [S4–S9]. Note that owing to the spinning of the silica sphere with an angular velocity S , a Sagnac-Fizeau shift is experienced by the light, i.e., $\omega_c \rightarrow \omega_c + \delta_s$, where ω_c is the nonspinning (i.e., standard) system and $\delta_s = \pm SA$ denotes the Sagnac-Fizeau shift of the driving detuning, with $\Lambda = \zeta r \omega_c [1 - 1/\zeta^2 - (\lambda/\zeta) d\zeta/d\lambda]/c$, where the parameters r , ζ , c , and λ are the silica-sphere radius, the refractive index, the speed of light in vacuum, and the wavelength of light, respectively. The relativistic origin of the Sagnac effect is characterized by the dispersion term (i.e., $dn/d\lambda$), which is small in typical materials (up to $\sim 1\%$). By rotating the silica sphere along only in the clockwise direction, the resulting $\delta_s > 0$ ($\delta_s < 0$) corresponds to the case, where the driving laser is injected from its left-hand side (LHS) or right-hand side (RHS) of the fibre, leading to an optical mode a_L or a_R , respectively. Therefore, the clockwise (a_R) and anticlockwise (a_L) optical frequencies are, respectively, defined as $\omega_c^{R,L} = \omega_c \pm |\delta_s|$. Note that $\delta_s = 0$ (i.e., $S = 0$) denotes the nonspinning (i.e., standard) case, where we obtain $a_{R,L} = a$ and $\omega_c^{R,L} = \omega_c$.

Next, we apply a linearization procedure to simplify the physical model, and this is realized by considering the strong-driving regime of the quantum system. Specifically, we express both optical and mechanical operators used in Eq. (S2) as the sums of their steady-state mean values and quantum fluctuations, i.e.,

$$a_{R,L} = \bar{a}_{R,L} + \delta a_{R,L}, \quad b_j = \bar{b}_j + \delta b_j. \quad (\text{S3})$$

By separating the classical motion from their quantum fluctuations, we obtain the equations of motion for the classical-motion variables and then, the steady-state mean of the optical dynamical variable is obtained as:

$$\bar{a}_{R,L} = \frac{\sqrt{\kappa_{\text{in}}} \epsilon_{\text{in}}}{\kappa/2 - i\Delta_{R,L}}, \quad (\text{S4})$$

where we introduce the normalized driving detuning

$$\Delta_{R,L} \approx \Delta \mp |\delta_s|, \quad (\text{S5})$$

with the driving detuning $\Delta = \omega_{R(L)} - \omega_c$ for $\omega_R = \omega_L$. Meanwhile, the linearized equations of motion for these quantum fluctuations are given by:

$$\delta \dot{a}_{R,L} = -\left(\frac{\kappa}{2} - i\Delta_{R,L}\right) \delta a_{R,L} - iG_{1,R,L} \delta z_1 - iG_{2,R,L} \delta z_2, \quad (\text{S6a})$$

$$\delta \dot{b}_1 = -\left(\frac{\gamma_1}{2} + i\omega_1\right) \delta b_1 - i\left(G_{1,R,L}^* \delta a_{R,L} + G_{1,R,L} \delta a_{R,L}^\dagger\right) + \sqrt{\gamma_1} \eta_1, \quad (\text{S6b})$$

$$\delta \dot{b}_2 = -\left(\frac{\gamma_2}{2} + i\omega_2\right) \delta b_2 - i\left(G_{2,R,L}^* \delta a_{R,L} + G_{2,R,L} \delta a_{R,L}^\dagger\right) + \sqrt{\gamma_2} \eta_2, \quad (\text{S6c})$$

where $\delta a_{R,L}$ ($\delta a_{R,L}^\dagger$) and δb_j (δb_j^\dagger) are the quantum fluctuation annihilation (creation) operators of the optical mode and the j th vibrational mode, respectively. The parameters $G_{j,R,L} = g_j \bar{a}_{R,L}$ are the linearized optomechanical-coupling strength between the optical mode and the j th vibrational mode. Note that, in the following discussions, $\bar{a}_{R,L}$ is assumed to be real, which is accessible by choosing a proper driving amplitude. This indicates that the linearized optomechanical-coupling strengths $G_{j,R,L}$ are real too.

The topological energy transfer can be solved by finding the solution of Eq. (S6), and this can be realized by transforming these variables into the frequency domain with the Fourier transformation, which is used to understand better the optical modification of the mechanical susceptibilities. Under the definition for an operator o and its conjugate o^\dagger , i.e.,

$$o(t) = \frac{1}{\sqrt{2\pi}} \int_{-\infty}^{\infty} e^{i\omega t} o(\omega) d\omega, \quad o^\dagger(t) = \frac{1}{\sqrt{2\pi}} \int_{-\infty}^{\infty} e^{-i\omega t} o^\dagger(\omega) d\omega, \quad (\text{S7})$$

where the operators $o = a_R, a_L, b_1$, and b_2 . The equations of motion shown in Eq. (S6), by performing the Fourier transformation in Eq. (S7), can be expressed in the frequency domain as:

$$-i\omega \delta a_{R,L}(\omega) = -\left(\frac{\kappa}{2} - i\Delta_{R,L}\right) \delta a_{R,L}(\omega) - iG_{1,R,L} \delta z_1(\omega) - iG_{2,R,L} \delta z_2(\omega), \quad (\text{S8a})$$

$$-i\omega \delta a_{R,L}^\dagger(\omega) = -\left(\frac{\kappa}{2} + i\Delta_{R,L}\right) \delta a_{R,L}^\dagger(\omega) + iG_{1,R,L}^* \delta z_1^\dagger(\omega) + iG_{2,R,L}^* \delta z_2^\dagger(\omega), \quad (\text{S8b})$$

$$-i\omega \delta b_1(\omega) = -\left(\frac{\gamma_1}{2} + i\omega_1\right) \delta b_1(\omega) - i\left[G_{1,R,L}^* \delta a_{R,L}(\omega) + G_{1,R,L} \delta a_{R,L}^\dagger(\omega)\right] + \sqrt{\gamma_1} \eta_1, \quad (\text{S8c})$$

$$-i\omega \delta b_2(\omega) = -\left(\frac{\gamma_2}{2} + i\omega_2\right) \delta b_2(\omega) - i\left[G_{2,R,L}^* \delta a_{R,L}(\omega) + G_{2,R,L} \delta a_{R,L}^\dagger(\omega)\right] + \sqrt{\gamma_2} \eta_2. \quad (\text{S8d})$$

Based on the above Eq. (S8), we subsequently obtain:

$$\left[\frac{\kappa}{2} - i(\omega + \Delta_{R,L})\right] \delta a_{R,L}(\omega) = -iG_{1,R,L} \delta z_1(\omega) - iG_{2,R,L} \delta z_2(\omega), \quad (\text{S9a})$$

$$\left[\frac{\kappa}{2} + i(\Delta_{R,L} - \omega)\right] \delta a_{R,L}^\dagger(\omega) = iG_{1,R,L}^* \delta z_1^\dagger(\omega) + iG_{2,R,L}^* \delta z_2^\dagger(\omega), \quad (\text{S9b})$$

$$\left[\frac{\gamma_1}{2} - i(\omega - \omega_1)\right] \delta b_1(\omega) = -i\left[G_{1,R,L}^* \delta a_{R,L}(\omega) + G_{1,R,L} \delta a_{R,L}^\dagger(\omega)\right] + \sqrt{\gamma_1} \eta_1, \quad (\text{S9c})$$

$$\left[\frac{\gamma_2}{2} - i(\omega - \omega_2)\right] \delta b_2(\omega) = -i\left[G_{2,R,L}^* \delta a_{R,L}(\omega) + G_{2,R,L} \delta a_{R,L}^\dagger(\omega)\right] + \sqrt{\gamma_2} \eta_2, \quad (\text{S9d})$$

where the optical susceptibility $\chi_{R,L}(\omega)$ is defined as:

$$\chi_{R,L}(\omega) = \left[\frac{\kappa}{2} - i(\omega + \Delta_{R,L})\right]^{-1}. \quad (\text{S10})$$

Thus, we can easily obtain

$$\delta a_{R,L}(\omega) = -iG_{1,R,L} \chi_{R,L}(\omega) (\delta b_1^\dagger + \delta b_1) - iG_{2,R,L} \chi_{R,L}(\omega) (\delta b_2^\dagger + \delta b_2), \quad (\text{S11})$$

where the introduced position operators z_j is defined as

$$z_j = b_j^\dagger + b_j. \quad (\text{S12})$$

By substituting Eq. (S12) into Eq. (S11), we obtain

$$\left[\frac{\kappa}{2} + i(\Delta - \omega)\right] \delta a_{R,L}^\dagger(\omega) = iG_{1,R,L}^* \delta z_1^\dagger + iG_{2,R,L}^* \delta z_2^\dagger = iG_{1,R,L}^* \delta z_1 + iG_{2,R,L}^* \delta z_2. \quad (\text{S13})$$

We then easily have

$$\delta a_{R,L}^\dagger(\omega) = iG_{1,R,L}^* \chi_{R,L}^*(-\omega) \delta z_1 + iG_{2,R,L}^* \chi_{R,L}^*(-\omega) \delta z_2, \quad (\text{S14})$$

where all the optical susceptibilities used are given by:

$$\chi_{R,L}(\omega) = \left[\frac{\kappa}{2} - i(\omega + \Delta_{R,L})\right]^{-1}, \quad (\text{S15a})$$

$$\chi_{R,L}^*(\omega) = \left[\frac{\kappa}{2} + i(\omega + \Delta_{R,L})\right]^{-1}, \quad (\text{S15b})$$

$$\chi_{R,L}(-\omega) = \left[\frac{\kappa}{2} - i(-\omega + \Delta_{R,L})\right]^{-1}, \quad (\text{S15c})$$

$$\chi_{R,L}^*(-\omega) = \left[\frac{\kappa}{2} + i(\Delta_{R,L} - \omega)\right]^{-1}. \quad (\text{S15d})$$

Consequently, we have

$$\delta a_{R,L}(\omega) = -i\alpha_1 \chi_{R,L}(\omega) (\delta b_1^\dagger + \delta b_1) - i\alpha_2 \chi_{R,L}(\omega) (\delta b_2^\dagger + \delta b_2), \quad (\text{S16a})$$

$$\delta a_{R,L}^\dagger(\omega) = i\alpha_1^* \chi_{R,L}^*(-\omega) (\delta b_1^\dagger + \delta b_1) + i\alpha_2^* \chi_{R,L}^*(-\omega) (\delta b_2^\dagger + \delta b_2). \quad (\text{S16b})$$

The next step, we substitute the expressions of $\delta a_{R,L}$ and $\delta a_{R,L}^\dagger$ [i.e., Eqs. (S16)] into Eqs. (S9c) and (S9d) and then, we obtain

$$\begin{aligned} \left[\frac{\gamma_1}{2} - i(\omega - \omega_1)\right] \delta b_1(\omega) = & -iG_{1,R,L}^* \left[-iG_{1,R,L} \chi_{R,L}(\omega) (\delta b_1^\dagger + \delta b_1) - iG_{2,R,L} \chi_{R,L}(\omega) (\delta b_2^\dagger + \delta b_2)\right] \\ & - iG_{1,R,L} \left[iG_{1,R,L}^* \chi_{R,L}^*(-\omega) (\delta b_1^\dagger + \delta b_1) + iG_{2,R,L}^* \chi_{R,L}^*(-\omega) (\delta b_2^\dagger + \delta b_2)\right] + \sqrt{\gamma_1} \eta_1, \end{aligned} \quad (\text{S17a})$$

$$\begin{aligned} \left[\frac{\gamma_2}{2} - i(\omega - \omega_2)\right] \delta b_2(\omega) = & -iG_{2,R,L}^* \left[-iG_{1,R,L} \chi_{R,L}(\omega) (\delta b_1^\dagger + \delta b_1) - iG_{2,R,L} \chi_{R,L}(\omega) (\delta b_2^\dagger + \delta b_2)\right] \\ & - iG_{2,R,L} \left[iG_{1,R,L}^* \chi_{R,L}^*(-\omega) (\delta b_1^\dagger + \delta b_1) + iG_{2,R,L}^* \chi_{R,L}^*(-\omega) (\delta b_2^\dagger + \delta b_2)\right] + \sqrt{\gamma_2} \eta_2, \end{aligned} \quad (\text{S17b})$$

$$\begin{aligned} \left[\frac{\gamma_1}{2} - i(\omega - \omega_1)\right] \delta b_1(\omega) = & G_{1,R,L} G_{1,R,L}^* \left[-\chi_{R,L}(\omega) + \chi_{R,L}^*(-\omega)\right] (\delta b_1^\dagger + \delta b_1) \\ & + \left[-G_{1,R,L}^* G_{2,R,L} \chi_{R,L}(\omega) + G_{1,R,L} G_{2,R,L}^* \chi_{R,L}^*(-\omega)\right] (\delta b_2^\dagger + \delta b_2) + \sqrt{\gamma_1} \eta_1, \end{aligned} \quad (\text{S17c})$$

$$\begin{aligned} \left[\frac{\gamma_2}{2} - i(\omega - \omega_2)\right] \delta b_2(\omega) = & \left[-G_{2,R,L}^* G_{1,R,L} \chi_{R,L}(\omega) + G_{2,R,L} G_{1,R,L}^* \chi_{R,L}^*(-\omega)\right] (\delta b_1^\dagger + \delta b_1) \\ & + \left[-G_{2,R,L}^* G_{2,R,L} \chi_{R,L}(\omega) + G_{2,R,L} G_{2,R,L}^* \chi_{R,L}^*(-\omega)\right] (\delta b_2^\dagger + \delta b_2) + \sqrt{\gamma_2} \eta_2. \end{aligned} \quad (\text{S17d})$$

Now, we can safely drop the counter-rotating terms (i.e., δb_1^\dagger and δb_2^\dagger) and the mechanical drive terms η_j , which are not necessary for our physical model, as the system operates far from the ultrastrong coupling regime. This is mostly attributed to the fact that we drive the system to a particular initial state, turn off the drive, and then, focus on the evolution of the system without any mechanical drive applied. Therefore, the above equations shown in Eqs. (S17) become

$$\left[\frac{\gamma_1}{2} - i(\omega - \omega_1)\right] \delta b_1(\omega) = G_{1,R,L} G_{1,R,L}^* \left[-\chi_{R,L}(\omega) + \chi_{R,L}^*(-\omega)\right] \delta b_1(\omega) + \left[-G_{1,R,L}^* G_{2,R,L} \chi_{R,L}(\omega) + G_{1,R,L} G_{2,R,L}^* \chi_{R,L}^*(-\omega)\right] \delta b_2(\omega), \quad (\text{S18a})$$

$$\left[\frac{\gamma_2}{2} - i(\omega - \omega_2)\right] \delta b_2(\omega) = \left[-G_{1,R,L} G_{2,R,L}^* \chi_{R,L}(\omega) + G_{1,R,L}^* G_{2,R,L} \chi_{R,L}^*(-\omega)\right] \delta b_1(\omega) + G_{2,R,L}^* G_{2,R,L} \left[-\chi_{R,L}(\omega) + \chi_{R,L}^*(-\omega)\right] \delta b_2(\omega), \quad (\text{S18b})$$

and then, based on Eqs. (S18), we can easily have

$$\left[\frac{\gamma_1}{2} - i(\omega - \omega_1)\right] \delta b_1(\omega) = |G_{1,R,L}|^2 \left[\chi_{R,L}^*(-\omega) - \chi_{R,L}(\omega)\right] \delta b_1(\omega) + G_{1,R,L}^* G_{2,R,L} \left[\chi_{R,L}^*(-\omega) - \chi_{R,L}(\omega)\right] \delta b_2(\omega), \quad (\text{S19a})$$

$$\left[\frac{\gamma_2}{2} - i(\omega - \omega_2)\right] \delta b_2(\omega) = G_{1,R,L}^* G_{2,R,L} \left[\chi_{R,L}^*(-\omega) - \chi_{R,L}(\omega)\right] \delta b_1(\omega) + |G_{2,R,L}|^2 \left[\chi_{R,L}^*(-\omega) - \chi_{R,L}(\omega)\right] \delta b_2(\omega). \quad (\text{S19b})$$

We below rewrite Eq. (S19) as a standard form:

$$-i\omega \delta b_1(\omega) = -\left(\frac{\gamma_1}{2} + i\omega_1\right) \delta b_1(\omega) + |G_{1,R,L}|^2 \left[\chi_{R,L}^*(-\omega) - \chi_{R,L}(\omega)\right] \delta b_1(\omega) + G_{1,R,L}^* G_{2,R,L} \left[\chi_{R,L}^*(-\omega) - \chi_{R,L}(\omega)\right] \delta b_2(\omega), \quad (\text{S20a})$$

$$-i\omega \delta b_2(\omega) = -\left(\frac{\gamma_2}{2} + i\omega_2\right) \delta b_2(\omega) + G_{1,R,L}^* G_{2,R,L} \left[\chi_{R,L}^*(-\omega) - \chi_{R,L}(\omega)\right] \delta b_1(\omega) + |G_{2,R,L}|^2 \left[\chi_{R,L}^*(-\omega) - \chi_{R,L}(\omega)\right] \delta b_2(\omega). \quad (\text{S20b})$$

Therefore, the matrix form based on Eq. (S20) can be obtained as

$$-i\omega \begin{pmatrix} \delta b_1(\omega) \\ \delta b_2(\omega) \end{pmatrix} = \begin{pmatrix} -\left(\frac{\gamma_1}{2} + i\omega_1\right) & 0 \\ 0 & -\left(\frac{\gamma_2}{2} + i\omega_2\right) \end{pmatrix} \begin{pmatrix} \delta b_1(\omega) \\ \delta b_2(\omega) \end{pmatrix} + \begin{pmatrix} |G_{1,R,L}|^2 & G_{1,R,L}^* G_{2,R,L} \\ G_{1,R,L}^* G_{2,R,L} & |G_{2,R,L}|^2 \end{pmatrix} \left[\chi_{R,L}^*(-\omega) - \chi_{R,L}(\omega)\right] \begin{pmatrix} \delta b_1(\omega) \\ \delta b_2(\omega) \end{pmatrix}. \quad (\text{S21})$$

In a traditional optomechanical system, the single-mode optomechanical self-energy can be obtained as

$$\sum_{R,L}(\omega) = i |G_{j,R,L}|^2 \left[\chi_{R,L}^*(-\omega) - \chi_{R,L}(\omega)\right]. \quad (\text{S22})$$

Note that $\sum_{R,L}(\omega)$ is often called the optomechanical ‘‘self-energy’’, and represents the optical modification of the mechanical resonance. This arises from the self-interaction occurring via the dynamical system formed by the optics/mechanics. From the definition of $\sum_{R,L}(\omega)$, we see that it will be a complex quantity depending on the laser power and detuning (through its dependence on cavity photon numbers $\bar{a}_{R,L}$ and optical susceptibility $\chi_c^{R,L}$). We also note here that the dependence on ω comes only through the cavity susceptibility, which varies with ω on a scale of κ . Since we are considering only a weak interaction, we can assume that the width of the mechanical resonance will be significantly less than κ . Thus, we can assume that $\chi_c^{R,L}(\omega)$ and hence $\sum_{R,L}(\omega)$ will be constant with respect to ω over the relevant mechanical bandwidth. Therefore, we can eliminate the frequency dependence and simply evaluate the self-energy at the mechanical frequency: $\sum_{R,L}(\omega) \approx \sum_{R,L}(\omega_0) = \sum_{R,L}$.

By inspecting the appearance of $\sum_{R,L}$ in the effective susceptibility, we see that the real part of $\sum_{R,L}$ corresponds to a shift in the mechanical frequency (‘‘optical spring’’), while the imaginary part results in a change in the effective damping rate of the oscillator (‘‘optical damping’’). This dynamical backaction is the mechanism by which one is able to control the motion in an optomechanical system, by exploiting and controlling the radiation pressure force. We will now explore this control in more detail, to better understand its limitations and tunability.

Specifically, the above equation shown in Eq. (S22) can be rewritten as:

$$\begin{aligned} \sum_{R,L}(\omega) &= \begin{pmatrix} i|G_{1,R,L}|^2 & i|G_{1,R,L}^*G_{2,R,L}| \\ i|G_{1,R,L}^*G_{2,R,L}| & i|G_{2,R,L}|^2 \end{pmatrix} [\chi_{R,L}^*(-\omega) - \chi_{R,L}(\omega)] \\ &= \begin{pmatrix} -ig_1^2\sigma_{R,L} & -ig_1g_2\sigma_{R,L} \\ -ig_1g_2\sigma_{R,L} & -ig_2^2\sigma_{R,L} \end{pmatrix}, \end{aligned} \quad (\text{S23})$$

where the complex vibrational susceptibilities $\sigma_{R,L}$, which are introduced by the laser driving, are defined as

$$\sigma_{R,L} = \frac{P\kappa_{\text{in}}}{\hbar\omega_{R,L} \left[\left(\frac{\kappa}{2}\right)^2 + \Delta_{R,L}^2 \right]} \left[\frac{1}{\frac{\kappa}{2} - i(\omega_0 + \Delta_{R,L})} - \frac{1}{\frac{\kappa}{2} + i(-\omega_0 + \Delta_{R,L})} \right]. \quad (\text{S24})$$

Now, we can have

$$-i\omega \begin{pmatrix} \delta b_1(\omega) \\ \delta b_2(\omega) \end{pmatrix} = \begin{pmatrix} -\left(\frac{\gamma_1}{2} + i\omega_1\right) & 0 \\ 0 & -\left(\frac{\gamma_2}{2} + i\omega_2\right) \end{pmatrix} \begin{pmatrix} \delta b_1(\omega) \\ \delta b_2(\omega) \end{pmatrix} - i \sum_{R,L}(\omega) \begin{pmatrix} \delta b_1(\omega) \\ \delta b_2(\omega) \end{pmatrix}, \quad (\text{S25})$$

and, then, Eq. (S25) can be rewritten as a matrix form as:

$$-i\omega \mathbf{B}(\omega) = - \begin{pmatrix} \left(\frac{\gamma_1}{2} + i\omega_1\right) & 0 \\ 0 & \left(\frac{\gamma_2}{2} + i\omega_2\right) \end{pmatrix} \mathbf{B}(\omega) - i \sum_{R,L}(\omega) \mathbf{B}(\omega), \quad (\text{S26})$$

where the matrix $\mathbf{B}(\omega)$ is defined as

$$\mathbf{B}(\omega) = \begin{pmatrix} \delta b_1(\omega) \\ \delta b_2(\omega) \end{pmatrix}. \quad (\text{S27})$$

Before moving back to the time domain, we note that $\sum_{R,L}(\omega)$ varies on the scale of κ , whereas the vibrational modes are susceptible to the drives only within their linewidth, which is substantially smaller than κ , by our assumption. Therefore, it is both safe and sufficient to consider the following assumptions:

$$\sum_{R,L}(\omega) \approx \sum_{R,L}(\omega_1) \approx \sum_{R,L}(\omega_2) \equiv \sum_{R,L}, \quad (\text{S28})$$

where

$$\sum_{R,L} = \sum_{R,L}(\omega_0) = \sum_{R,L} \left(\frac{\omega_1 + \omega_2}{2} \right), \quad (\text{S29})$$

for

$$\omega_0 = \frac{\omega_1 + \omega_2}{2}. \quad (\text{S30})$$

We note that the motional modes are also assumed to be nearly degenerate. Therefore, owing to the fact that $\sum_{R,L}$ is not a function of ω , we can easily move back to the time domain and then, we obtain:

$$\dot{\mathbf{B}}(t) = - \begin{pmatrix} \left(\frac{\gamma_1}{2} + i\omega_1\right) & 0 \\ 0 & \left(\frac{\gamma_2}{2} + i\omega_2\right) \end{pmatrix} \mathbf{B}(t) - i \sum_{R,L} \mathbf{B}(t). \quad (\text{S31})$$

Mathematically, by adiabatically eliminating the optical mode, an effective Hamiltonian only for the two motional modes b_1 and b_2 can be obtained as:

$$i\dot{\mathbf{B}}(t) = \mathcal{H}_{\text{eff}}^{R,L} \mathbf{B}(t), \quad (\text{S32})$$

and

$$\mathcal{H}_{\text{eff}}^{R,L} = \begin{pmatrix} \omega_1 - \frac{i\gamma_1}{2} - ig_1^2\sigma_{R,L} & -ig_1g_2\sigma_{R,L} \\ -ig_1g_2\sigma_{R,L} & \omega_2 - \frac{i\gamma_2}{2} - ig_2^2\sigma_{R,L} \end{pmatrix}, \quad (\text{S33})$$

where the simplified complex vibrational susceptibilities $\sigma_{R,L}$, introduced by the laser driving and based on Eq. (S24), are defined as:

$$\sigma_{R,L} = \frac{P_{\text{kin}} [\chi_{R,L}(\omega_0) - \chi_{R,L}^*(-\omega_0)]}{\hbar\omega_{R,L} [(\kappa/2)^2 + \Delta_{R,L}^2]}, \quad (\text{S34})$$

with the optical susceptibilities

$$\chi_{R,L}(\omega_0) = \left[\frac{\kappa}{2} - i(\omega_0 + \Delta_{R,L}) \right]^{-1}. \quad (\text{S35})$$

Below, we derive in detail the exceptional point of the physical system, and analyze the performance of energy transfer based on the Hamiltonian $\mathcal{H}_{\text{eff}}^{R,L}$, shown in Eq. (S33).

B. Exceptional point

Here we study a multimode optomechanical system consisting of two vibrational modes, each of which is linearly coupled to a common optical mode, i.e., the two motional modes are uncoupled to each other. By adiabatically removing the optical mode, the driving-laser field can generate a *tunable effective* interaction between these two motional modes that are exploited for inducing an EP. Specifically, in the following detailed analysis, it is safe to eliminate the common evolution, with the average frequency ω_0 defined as in Eq. (S30), and the average decay rate Γ of the two vibrational modes defined as

$$\Gamma = (\gamma_1 + \gamma_2)/2. \quad (\text{S36})$$

Specifically, the parameters ω_1 , ω_2 , γ_1 , and γ_2 can be smoothly replaced with the redefined parameters ω_0 , Ω , Γ , and γ . Thus the effective Hamiltonian $\mathcal{H}_{\text{eff}}^{R,L}$ shown in Eq. (S33) becomes:

$$\mathcal{H}_{\text{eff}}^{R,L} = \begin{pmatrix} \omega_0 - i\frac{\Gamma}{2} - \Omega - i\frac{\gamma}{2} - ig_1^2\sigma_{R,L} & -ig_1g_2\sigma_{R,L} \\ -ig_1g_2\sigma_{R,L} & \omega_0 - i\frac{\Gamma}{2} + \Omega + i\frac{\gamma}{2} - ig_2^2\sigma_{R,L} \end{pmatrix}, \quad (\text{S37})$$

where the introduced new parameters Ω and γ are, respectively, defined as:

$$\Omega = (\omega_2 - \omega_1)/2, \quad (\text{S38})$$

and

$$\gamma = (\gamma_1 - \gamma_2)/2. \quad (\text{S39})$$

Below, we can easily have the following equations:

$$\begin{aligned} i\frac{d}{dt} \begin{pmatrix} b_1(t) \\ b_2(t) \end{pmatrix} &= \begin{pmatrix} \omega_0 - i\frac{\Gamma}{2} - \Omega - i\frac{\gamma}{2} - ig_1^2\sigma_{R,L} & -ig_1g_2\sigma_{R,L} \\ -ig_1g_2\sigma_{R,L} & \omega_0 - i\frac{\Gamma}{2} + \Omega + i\frac{\gamma}{2} - ig_2^2\sigma_{R,L} \end{pmatrix} \begin{pmatrix} b_1(t) \\ b_2(t) \end{pmatrix}, \\ &= \begin{pmatrix} \omega_0 - i\frac{\Gamma}{2} & 0 \\ 0 & \omega_0 - i\frac{\Gamma}{2} \end{pmatrix} \begin{pmatrix} b_1(t) \\ b_2(t) \end{pmatrix} + \begin{pmatrix} -\Omega - i\frac{\gamma}{2} - ig_1^2\sigma_{R,L} & -ig_1g_2\sigma_{R,L} \\ -ig_1g_2\sigma_{R,L} & \Omega + i\frac{\gamma}{2} - ig_2^2\sigma_{R,L} \end{pmatrix} \begin{pmatrix} b_1(t) \\ b_2(t) \end{pmatrix}, \\ &= \begin{pmatrix} \omega_0 - i\frac{\Gamma}{2} & 0 \\ 0 & \omega_0 - i\frac{\Gamma}{2} \end{pmatrix} \begin{pmatrix} b_1(t) \\ b_2(t) \end{pmatrix} + i\frac{d}{dt} \begin{pmatrix} b_+(t) \\ b_-(t) \end{pmatrix}, \end{aligned} \quad (\text{S40})$$

where

$$i\frac{d}{dt} \begin{pmatrix} b_+(t) \\ b_-(t) \end{pmatrix} = \begin{pmatrix} -\Omega - i\frac{\gamma}{2} - ig_1^2\sigma_{R,L} & -ig_1g_2\sigma_{R,L} \\ -ig_1g_2\sigma_{R,L} & \Omega + i\frac{\gamma}{2} - ig_2^2\sigma_{R,L} \end{pmatrix} \begin{pmatrix} b_+(t) \\ b_-(t) \end{pmatrix}. \quad (\text{S41})$$

Based on Eq. (S37) and using the mathematics, the eigenvalues of our effective physical system can be obtained:

$$\lambda_{\mp}^{R,L} = -\frac{i}{2} (g_1^2 + g_2^2) \sigma_{R,L} \mp \lambda_{R,L}, \quad (\text{S42})$$

where the parameter $\lambda_{R,L}$ is defined as

$$\lambda_{R,L} = i\sqrt{g_1^2g_2^2\sigma_{R,L}^2 + \frac{1}{4}[\gamma + (g_1^2 - g_2^2)\sigma_{R,L}]^2 - \Omega^2 - i\Omega[\gamma + (g_1^2 - g_2^2)\sigma_{R,L}]}. \quad (\text{S43})$$

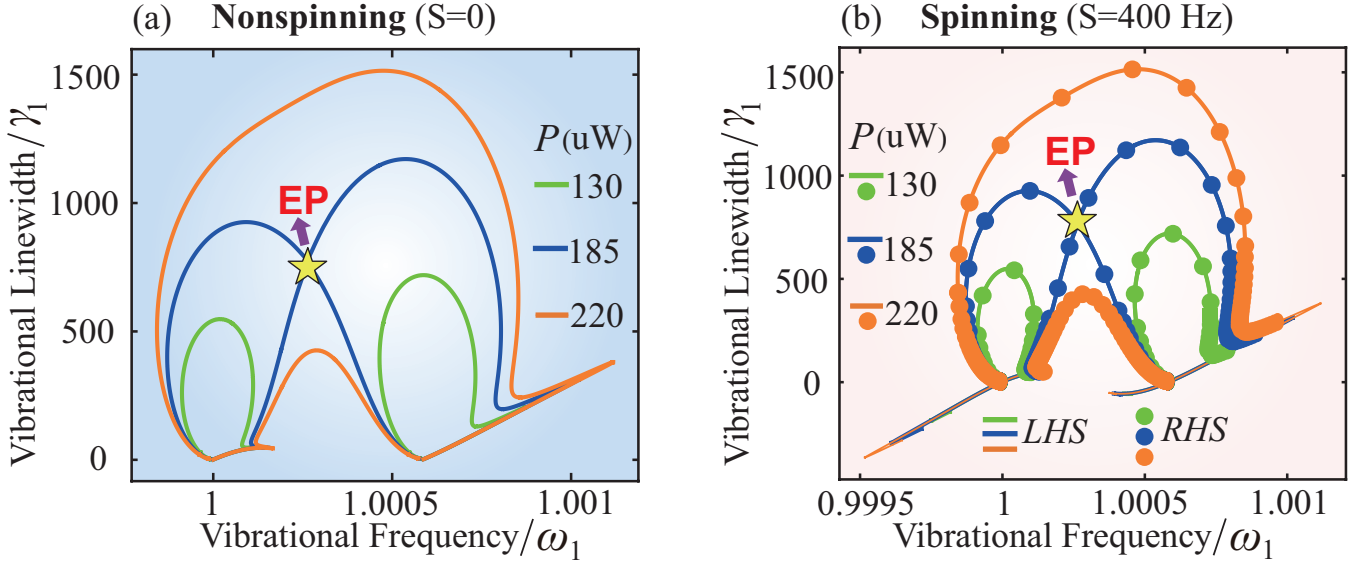


FIG. S1: Complex eigenvalues of the two motional normal modes. The vibrational decay rate (see the vertical axis) and the vibrational resonance frequency (see the horizontal axis) of the two motional normal modes as functions of the driving detuning Δ and the driving laser power P when the system operates in both (a) nonspinning (i.e., $S = 0$) and (b) spinning (i.e., $S \neq 0$) cases. That is for the spinning case, we consider the situations where the rotating silica sphere is driven from the LHS or RHS of the fibre. Here the values of the laser power $P = 130$ uW, 185 uW, and 220 uW are, respectively, described by the green, blue, and orange; and the complex eigenvalues of the quantum system are varied with the driving detuning $\Delta \in [-2\omega_1, 0]$ at fixed $P = 130$ uW (green), 185 uW (blue), and 220 uW (orange). Note that for lower values of the laser power P , each eigenvalue follows a closed trajectory, which ends and begins at the same point. In stark contrast to the case of the low powers, for higher values of the driving power P , the eigenvalues follow open trajectories, each of which ends at the starting point of the other. By tuning the laser power P and the driving detuning Δ , the EP which is described by the yellow star occurs. In our simulations, to ensure the system stability, we choose experimentally feasible parameters [S4, S10], as shown in main text.

Therefore, we have

$$\tilde{\lambda}_{\pm}^{R,L} = \omega_0 - \frac{i\Gamma}{2} - \frac{i}{2} (g_1^2 + g_2^2) \sigma_{R,L} \mp \lambda_{R,L}. \quad (\text{S44})$$

By just simply tuning the complex vibrational susceptibilities $\sigma_{R,L}$, the system possesses an EP. Thus, one needs to control over both $\text{Re}(\sigma_{R,L})$ and $\text{Im}(\sigma_{R,L})$. The real and imaginary parts of the complex eigenvalues of the two motional normal modes (i.e., b_{\pm}) are the resonance frequencies $\omega_{\pm}^{R,L}(\Delta, P) = \text{Re}(\lambda_{\pm}^{R,L})$ and the linewidths $\gamma_{\pm}^{R,L}(\Delta, P) = -2\text{Im}(\lambda_{\pm}^{R,L})$, respectively. Note that in our model, the control of the optomechanical system is achieved by a separate laser, and its driving power P and driving detuning Δ are set by an acousto-optic modulator. We can measure the vibration spectra of the mechanical motions as functions of the driving detuning Δ and the driving power P , so that the presence of the EP in our system can be accurately established. In addition, these spectra are acquired by driving the vibrations and monitoring its response via a heterodyne signal. We fit each spectrum to determine the two motional damping rates, $\gamma_{\pm}^{R,L}(\Delta, P)$, and the two vibrational resonance frequencies, $\omega_{\pm}^{R,L}(\Delta, P)$. Note that the subscripts “ \pm ” refer to the vibrational normal modes of the resonators, when the optical field is introduced to the physical system.

We show measurements of the real and imaginary parts of the corresponding complex eigenvalues for the two vibrational normal modes over a narrow range of the driving detuning Δ and the driving power P , which are centred at Δ_{EP} and P_{EP} . Here the parameters Δ_{EP} and P_{EP} denote the parameter position on the emergence of the EP. These measurements show the characteristic features of an EP. In the vicinity of this point, they exhibit the same structure as the Riemann sheets of the complex square-root function. The surfaces are such that if the driving-laser detuning Δ and the driving-laser power P were varied to execute a single closed loop, the resulting smooth evolution of the eigenvalue manifold would return to its starting point only if the loop does not enclose the EP. By contrast, a loop enclosing the EP would result in a trajectory starting on one sheet, but ending on the other.

The complex eigenvalues of the two vibrational normal modes are shown in Fig. S1. Specifically, we plot the motional decay rates [$\gamma_{\pm}^{R,L}(\Delta, P)$, see the vertical axis] and the vibrational resonance frequencies [$\omega_{\pm}^{R,L}(\Delta, P)$, see the horizontal axis] of the two normal modes of the vibrations as functions of the driving detuning Δ and the driving laser power P , when the system operates in both non-spinning and spinning cases. Note that the values of the driving laser power P are described by the different colors, and the eigenvalues of the system are varied with the driving detuning Δ from $-2\omega_1$ to 0 at a fixed P . We find from Figs. S1(a) and S1(b) that for a lower value of the driving-laser power P , each eigenvalue follows an enclosed path, which begins and ends

at the same point; and that for a higher value of the driving power P , the eigenvalues follow open paths, each one starting at the ending point of the other.

In particular, we reveal that the EP (see the yellow star in Fig. S1), where the eigenstates coalesce, occurs by just tuning the laser power P and the driving detuning Δ . More specifically, we see from Eqs. (S33) and (S34) that in the resolved-sideband regime, i.e.,

$$\kappa < \omega_0, \quad (\text{S45})$$

both reaching and encircling the EP require just to tune the driving power P and the driving detuning Δ , without the need of any complicated arrangements [S11]. This is due to the fact that the parameters P and Δ in our system can be easily steered in situ with timing accuracy, a high-precision degree, and dynamic range. In addition, we reveal that when the rotating silica sphere is driven from the LHS or RHS of the fibre, the circumference of the trajectory in the LHS driving is larger than that in the RHS driving, because a profoundly different influence from the Fizeau-drag shift of the light emerges in these two cases.

Though the circumferences of the trajectory are different, the location of the EP actually keeps unchanged, as marked by the yellow star in Fig. S1. Especially, the circumference in the LHS-driving case is larger than that in the non-spinning case, which is also larger than that of the RHS injecting. Physically, the driving laser injected from the LHS of the fibre experiences a Sagnac-Fizeau shift, whereas the light entering from the RHS of the fibre leads to the opposite shift. Owing to the existence of the Fizeau light-dragging effect, the energy-transfer performance is significantly suppressed or even completely blocked in a chosen entering direction of the fibre while enhanced in the other side. This nonreciprocal transfer is fully independent of the encircling direction of the EP, which is otherwise unattainable in the previously established demonstrations [S12–S26].

II. ONE-WAY TOPOLOGICAL PHONONICS INDEPENDENT OF THE ENCIRCLING DIRECTION OF THE EP

In this section, we define a topological-phonon-transfer quality factor to quantify the energy transfer between the two motional normal modes, and show in detail the topological unidirectional control without depending on the EP-encircling direction, the speed-tunable phonon transfer, the tolerance against both masses and quality factors of quantum devices, and the strength-dependent topological transfer of thermal phonons.

A. Topological-energy-transfer quality factor

The projection onto the instantaneous eigenbasis is necessary to see the state evolution during the applied perturbations. Allow $\vec{v}_{\pm}(t)$ to serve as the instantaneous eigenvectors of $\mathcal{H}_{\text{eff}}^{R,L}$. Whenever necessary, the solution $\vec{b}(t) = (b_1(t), b_2(t))^T$ can be written as a projection based on this basis:

$$\vec{b}(t) = b_-(t)\vec{v}_-(t) + b_+(t)\vec{v}_+(t). \quad (\text{S46})$$

If the perturbation is slow compared to the energy gap ($\lambda_+ - \lambda_-$), one naive and unjustified approach to thinking about this system would be to assume that adiabaticity (in the sense of smooth evolution along the eigenvalue surface) would occur as long as the perturbation is slow. That is, if we were to prepare $b_-(0) = 1$ and $b_+(0) = 0$, then for all time t , $b_-(t) = 1$ would remain the dominant projection. We can use standard computational techniques to numerically integrate the linear differential equations to see if this happens. The calculation provides a complete solution for the system's time-dependent nature, $\vec{b}(t)$. It's worth pointing out that this result is based on the differential equation, not the eigenbasis. (i.e. $b_{1,2}(t)$ not $b_{\pm}(t)$). A change of basis defined by a matrix of instantaneous eigenvectors is necessary to find the projection into the instantaneous eigenbasis:

$$\begin{pmatrix} b_+(t) \\ b_-(t) \end{pmatrix} = \mathbf{N}(t) \begin{pmatrix} b_1(t) \\ b_2(t) \end{pmatrix}. \quad (\text{S47})$$

where

$$\mathbf{N}(t) = \left[\begin{pmatrix} \vec{v}_+(t) & \vec{v}_-(t) \end{pmatrix}^T \right]^{-1}, \quad (\text{S48})$$

We have already mentioned that this energy transfer is a result of an adiabatic-like process, and should be influenced by the geometry of the loop, in relation to the topology of the eigenvalue manifolds. A metric for quantifying energy transfer would be beneficial, in order to systematically characterize this behavior. *Essentially, if we initialize the system into a particular mode, i.e., $b_{\pm}(t=0) = 1$, we would like to know the amplitude of the other mode at the end of the loop, i.e., $b_{\mp}(t) = 1$.* Normalizing the

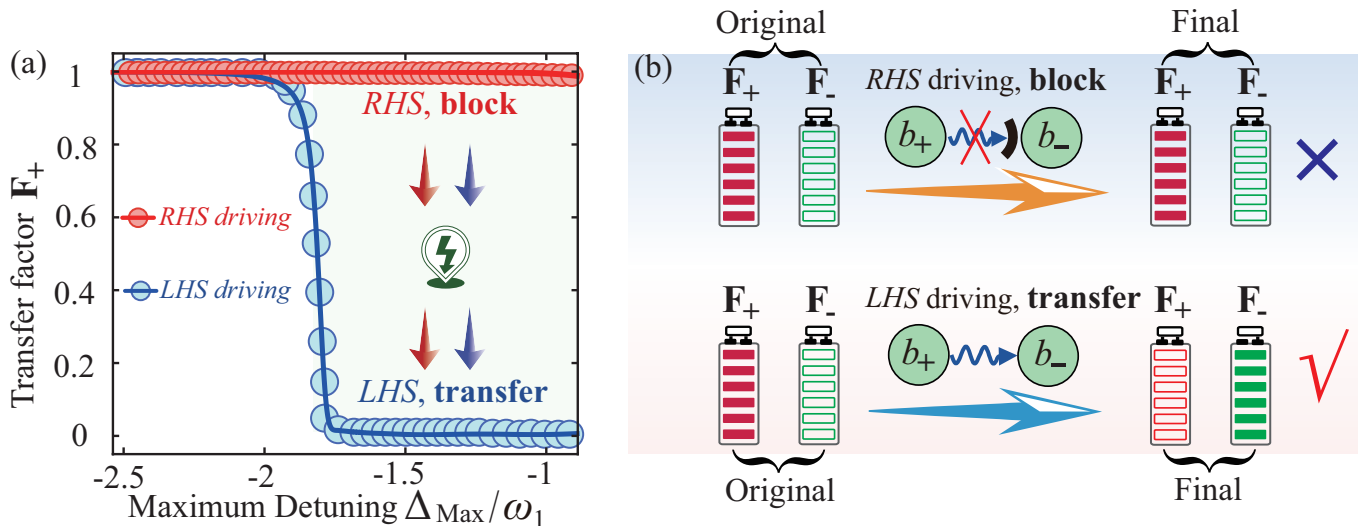


FIG. S2: (a) Topological energy-transfer quality factor \mathbf{F}_+ versus the maximal driving detuning Δ_{Max} , when the light enters from the LHS of the fibre (i.e., a_L , see the blue curves and symbols) or the RHS of the fiber (i.e., a_R , see the red curves and symbols), for the angular velocity $S = 400$ Hz of the spinning silica sphere. (b) Diagram of the topological energy-transfer quality factor \mathbf{F}_+ when the spinning silica sphere is driven from the RHS (i.e., a_R , see the upper half part) and LHS (i.e., a_L , see the downer half part) of the fibre. We see that the topological phonon transfer occurs when the silica sphere is driven in one chosen side but not in the other, and this leads to a unique topological energy-transfer nonreciprocity, without depending on the direction of winding around the EP.

total energy at the end of the loop is necessary, owing to the growth/decay of the overall system energy. To quantify the energy transfer from one motional normal mode (b_+) to the other (b_-), we define a quality factor of topological phonon transfer:

$$\mathbf{F}_+ = \frac{|b_+(\tau)|^2}{|b_+(\tau)|^2 + |b_-(\tau)|^2}, \quad (\text{S49})$$

denoting the fraction of the remaining energy in the b_+ mode after executing the control loops. Note that before performing all the control loops, the definition of \mathbf{F}_+ needs to satisfy the condition that all the energy remains in b_+ . For example, when we prepare the system in the b_+ mode at $t = 0$, the definition $\mathbf{F}_- = (1 - \mathbf{F}_+)$ describes how much energy has been transferred to the b_- mode at $t = \tau$ (relative to the total energy at this time).

So, for the b_+ initialization, if b_- is the dominant projection at the end, then we find $\mathbf{F}_- = (1 - \mathbf{F}_+) = 1$, whereas if the dominant projection is still b_+ , then we have $\mathbf{F}_+ = 0$. Specifically, we see from Eq. (S49) that

$$\mathbf{F}_+ \rightarrow 1 \quad (\text{S50})$$

indicates that *no* energy transfer occurs from the vibrational mode b_+ to b_- ; while a *perfect* energy transfer happens from b_+ to b_- when

$$\mathbf{F}_+ \rightarrow 0. \quad (\text{S51})$$

That is before the adiabatic control loop, 100% of the energy is in the b_+ mode, whereas after the adiabatic loop, 100% of the remaining energy is the b_- mode. We here should emphasize that our analysis and numerical simulations were all made assuming injecting the initial drive to the motional normal mode b_+ , and subsequently, performing a control loop only in the counter-clockwise direction. In this case, the adiabatic paths enclosing the EP correspond to the less-damped eigenmode for the majority of the control loop. On the contrary, executing clockwise the same control loop leads to an adiabatic path, which corresponds primarily to the more-damped eigenmode. Next, we will study in detail the one-way Topological control independent of the EP-encircling direction.

B. Unidirectional Topological control independent of the EP-encircling direction

In this subsection, we show in detail how to achieve the topological energy transfer, which is independent of the encircling direction of the EP.

We here execute the case where the dynamical encirclement around the EP is adiabatically carried out *only* anticlockwise, i.e., the encircling-EP adiabatic trajectory *does not* need to be traversed in the opposite direction. In this case, we find that by splitting the counter-propagating lights of a spinning silica microsphere via the Fizeau light-dragging effect, an one-way topological transfer of thermal phonons between two vibrational normal modes still can be achieved, i.e.,

$$\mathbf{F}_+ = 1 \rightarrow 0. \quad (\text{S52})$$

This is clearly seen in Fig. S2. Concretely, in this case, the laser injected from the LHS of the fibre experiences a Sagnac-Fizeau shift, which engenders an optimal energy transfer, whereas the light entering from the RHS of the fibre leads to an opposite shift, which yields no transfer of phonons. Contrary to the previously established demonstrations, the resulting nonreciprocal transport of phonons is fully independent of the encircling direction of the EP, which is otherwise *unattainable* in the well-known protocols [S12–S26].

Specifically, the angular velocity of the spinning silica microsphere is set at $S = 400$ Hz, which is experimentally accessible. Physically, the laser entering from one chosen side of the fibre experiences a Sagnac-Fizeau shift and however, the light entering from the other side leads to an opposite shift. In Fig. S2, we display \mathbf{F}_+ versus the maximal driving detuning Δ_{Max} for both LHS-driving (i.e., a_L) and RHS-driving (i.e., a_R) cases. It is revealed that by injecting light from the RHS of the fibre, *no* energy transfer is observed, i.e.,

$$\mathbf{F}_+ \rightarrow 1; \quad (\text{S53})$$

while by injecting it from the LHS of the fibre, an excellent topological transfer of phonons occurs, i.e.,

$$\mathbf{F}_+ \rightarrow 0, \quad (\text{S54})$$

without the need of any switch to the opposite direction of the EP-enclosing adiabatic control loops. This nonreciprocal transfer does not depend on the direction of the EP encirclement, that has no counterpart in the previously established demonstrations [S12–S26]. We point out that in our simulations, both the application of the initial drive to the mode b_+ and the execution of an anticlockwise EP-enclosing adiabatic control have been applied.

In fact, the resulting topological nonreciprocity here is different from that found in the previous studies, because in the standard schemes of generating the topological nonreciprocal transfer of energy, the encircling-EP adiabatic paths could result in a less-decayed eigenmode for the majority of the loop, and in stark contrast to this, the performing of the same control loop with clockwise encircling the EP leads to an adiabatic path, which indicates primarily the more-decayed eigenmode.

C. Detailed comparison of standard and our methods

The previous one-way topological behaviors [S12–S26] are naturally limited by the strict dependence on the encirclement direction of the EP in the parameter space, and this leads to a strong *suppression* effect on both the topological responses and their non-reciprocities. Specifically, for an initial excitation in a chosen mode, an efficient topological behavior (e.g., topological transfer of energy or state) is observed when executing an adiabatic trajectory enclosing clockwise an EP; while for counterclockwise encircling, no topological response happens [S12, S13]. This means that for the previous schemes, switching to the other encircling direction of the EP-enclosing control loop will result in no topological behaviors [S12, S13], and that the standard topological nonreciprocity relying on the EP-encircling direction will be generally suppressed or even fully destroyed in a very wide parameter region [S12, S13]. Here, we break these long-standing limitations and suppression effects, and build an excellent topological energy transfer and its nonreciprocity, independent of the EP-encircling direction, by just employing the Fizeau light-dragging effect [S4–S6].

Now, we compare in detail the topological-energy-transfer nonreciprocity based on the standard method and that using our proposal. Specifically, in the standard EP-encircling-direction-dependent nonreciprocity case, the topological-phonon-transfer factor \mathbf{F}_+ is plotted as a function of the maximal driving detuning Δ_{Max} , when the EP-enclosing control loop is counter-clockwise (\cup , see the blue solid curve) or clockwise (\cup , the red solid curve), as shown in Fig. S3(a). Meanwhile, based on our method, we plot \mathbf{F}_+ versus Δ_{Max} , when the light enters from the LHS (the blue solid curve) or the RHS (the red dashed curve) of the fiber, as shown in Fig. S3(b). We clearly see from Fig. S3(a) that in the standard-scheme case, there exists a valley around $-2.1 < \Delta_{\text{Max}}/\omega_1 < -1.3$ (see the left area of the black dashed vertical line, i.e., the red shadow area), which denotes the emergence of a strong suppression effect on the topological non-reciprocity (i.e., $\mathbf{F}_+^{\cup} \rightarrow 0$ and $\mathbf{F}_+^{\cup} \rightarrow 0$), and that an excellent topological non-reciprocity (i.e., $\mathbf{F}_+^{\cup} \rightarrow 0$ and $\mathbf{F}_+^{\cup} \rightarrow 1$) can be observed *only when* $\Delta_{\text{Max}}/\omega_1 > -1.3$. However, for our proposal [see Fig. S3(b)], no suppression effect on the topological nonreciprocity occurs in all the areas, which depicts an excellent topological nonreciprocity (i.e., $\mathbf{F}_+^{\text{LHS}} \rightarrow 0$ and $\mathbf{F}_+^{\text{RHS}} \rightarrow 1$).

To further elucidate this suppression-immune topological nonreciprocity realized by our method, we compare the performance of the nonreciprocity achieved by both the standard method and our proposal, in a wide frequency-detuning range ($-2.1 <$

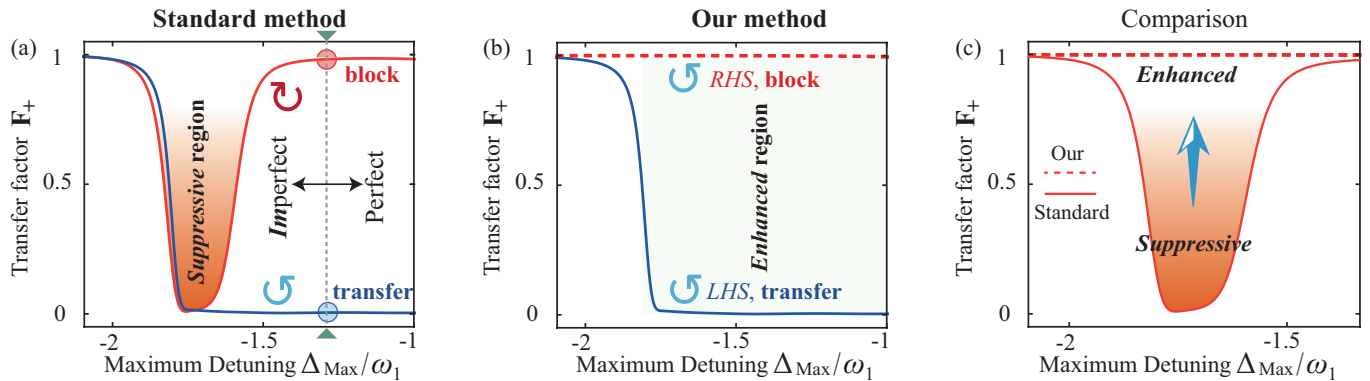


FIG. S3: (a) Topological-phonon-transfer factor F_+ versus the maximal driving detuning Δ_{Max} , when the EP is fully encircled in the counter-clockwise (\odot , the blue solid curve) or clockwise (\ominus , the red solid curve) direction, when $S = 400$ Hz. The red shadow area in (a) denotes the suppression region of the topological nonreciprocity, corresponding to an imperfect topological nonreciprocity ($F_+^{\odot} \rightarrow 0$ and $F_+^{\ominus} \rightarrow 0$, see the left-side area of the black vertical dashed line). (b) F_+ versus Δ_{Max} , when the light enters from the LHS (the blue solid curve) or the RHS (the red dashed curve) of the fiber for $S = 400$ Hz, by the counter-clockwise (\odot) encirclement of the EP. The blue shadow area in (b) depicts the enhanced region of the topological nonreciprocity, corresponding to a perfect topological nonreciprocity (i.e., $F_+^{\odot} \rightarrow 0$ and $F_+^{\ominus} \rightarrow 1$). (c) Comparison of the red solid curve of (a) obtained by the standard scheme and the red dashed curve of (b) achieved by our proposal. We clearly see that in a wide parameter region (i.e., $-2.1 < \Delta_{\text{Max}}/\omega_1 < -1.3$), the topological nonreciprocity is strongly suppressed with the standard method but enhanced using our proposal, which yields a perfect topological nonreciprocity.

$\Delta_{\text{Max}}/\omega_1 < -1.3$), as shown in Fig. S3(c). It is clearly shown that with increasing Δ_{Max} , the topological nonreciprocity is strongly *suppressed* with the standard method [S12, S13] but *enhanced* using our proposal, which results in an extremely excellent topological nonreciprocity. These results confirm that compared to the conventional topological nonreciprocity inherently existing a very wide suppression region, our method completely beats this suppression effect and builds an excellent topological nonreciprocity.

In the above-mentioned analysis, the comparison of the standard and our methods, which produce the nonreciprocal topological energy transfer when the EP-encircling control loop is counter-clockwise (\odot), has been studied in detail. Based on the above comparison, we fully break these suppression effects on the nonreciprocal topological response, and realize an excellent one-way topological energy transfer independent of the EP-encircling direction, by introducing the Fizeau light-dragging effect. Below, we study in detail the unidirectional topological phonon transfer by using our method, when the EP-encircling direction is switched to the clockwise (\ominus) direction from the counter-clockwise (\odot) direction.

To this end, we plot in Fig. S4 the topological-phonon-transfer factor F_+ as a function of the maximal driving detuning Δ_{Max} when the light is injected from the LHS (the blue curve) or the RHS (the red curve) of the fiber, in the case where the encircling direction of the EP is clockwise (\ominus). Using our method, we find that when switching to the clockwise-encircling direction (\ominus) from the anticlockwise-encircling direction (\odot) of the EP, the topological transfer of energy can also be observed and especially this energy transfer is non-reciprocal, which is otherwise unattainable in conventional schemes [S12, S13]. This is attributed to the fact that in the standard scheme, no topological response emerges when switching to the other encircling direction of the EP. It indicates that by introducing the Sagnac-Fizeau effect, the unidirectional topological phonon transfer can always occur whatever the direction of winding around the EP is. This demonstrates that our method can completely beat all the limitations in the previous schemes [S12–S26], and paves a route to producing a perfect one-way topological response.

Specifically, we find from Fig. S4 that the nonreciprocal topological phonon transfer occurs in the two regions: (i) Around $\Delta_{\text{Max}}/\omega_1 = -1.45$, we find that for the LHS driving, there exists a valley (see the blue shadow region), corresponding to the topological phonon transfer (see the blue disk); while for the RHS driving, the valley becomes the upper horizontal line (see the red disk), corresponding to no topological transfer of energy, which indicates the emergence of an excellent nonreciprocal topological phonon transfer [i.e., $F_+^{\text{LHS}} \rightarrow 0$ (corresponding to the transfer of energy) and $F_+^{\text{RHS}} \rightarrow 1$ (corresponding to the block of energy)]. (ii) Around $\Delta_{\text{Max}}/\omega_1 = -0.85$, the other valley can be observed (see the red shadow region), and it means that the other nonreciprocal topological transfer of energy happens [i.e., $F_+^{\text{LHS}} \rightarrow 1$ (corresponding to the block) and $F_+^{\text{RHS}} \rightarrow 0$ (corresponding to the transfer)]. Physically, the synergy of the topological operations and the Fizeau drag, leading to the difference of the refractive index that light experiences [S4–S6]. Therefore, the light injected from one chosen side of the fibre experiences a Sagnac-Fizeau shift, whereas the light entering from the other side yields an opposite shift, and this causes an effective nonreciprocity of the topological energy transfer [S4–S6].

These findings indicate that we produce a fundamentally different topological nonreciprocity independent of the encircling direction of the adiabatic loops enclosing the EP. This is otherwise unattainable in conventional schemes [S12–S26], where the dependence on the encircling direction of the EP is the essential requirements for all the standard unidirectional topological

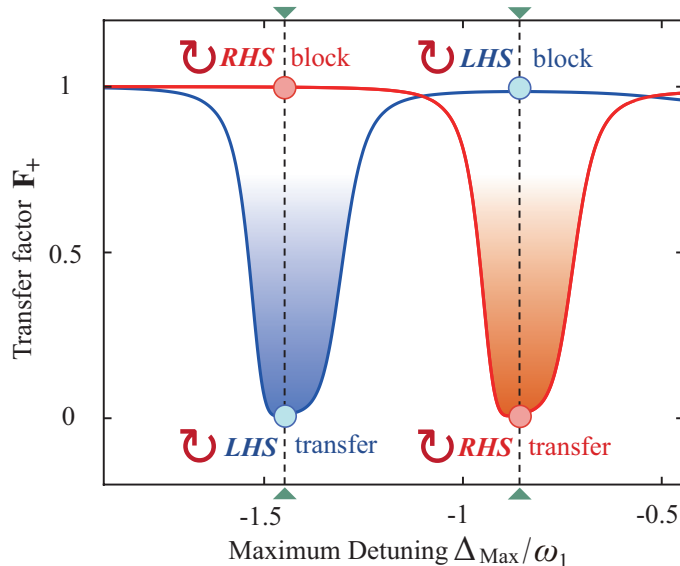


FIG. S4: Topological-phonon-transfer factor \mathbf{F}_+ versus the maximal driving detuning Δ_{Max} when the light enters from the LHS (the blue curve) or the RHS (the red curve) of the fiber for $S = 200$ Hz, when the encircling direction of the EP is clockwise (i.e., \odot). The blue and red shadow areas denote the emergence of the nonreciprocal topological phonon transfer, and the optimal topological nonreciprocity happens at the position of the blue and red disks (see the black dashed vertical lines). Note that the valleys correspond to the topological energy transfer, and the upper horizontal solid lines correspond to no topological transfer of energy (i.e., block).

behaviors (i.e., for the standard schemes, no topological behavior can occur once switching to the other encircling direction of the EP). It demonstrates that by using our method, the one-way topological energy transfer can always happen no matter what the encircling direction of the EP is, and these findings have no correspondence to the previously established demonstrations [S12–S26].

Our work not only opens up a new route to topological control beyond the EP-encircling-direction limitation, but also enables the exploration of other dynamical effects related to the EP, including the behavior of thermal and quantum fluctuations in their vicinity. In a broader view, our study sheds new light on the combination of the topological operations and the Fizeau light-dragging effect, and offers exciting opportunities of empowering new one-way topological behavior, with both independence on the EP-encircling direction and immunity against the suppression effect on the topological nonreciprocity. This work will enable the exploration of the EP physics in system control and energy or state transfer schemes at the crossroads between fundamental research and practical applications.

D. Speed-tunable topological phonon transfer

In this subsection, we reveal that in the adiabatic limit, the optimal topological energy transport can be easily speed-up, but also speed-down. Below, we study in detail this problem by finding out the relation between the topological-energy-transport factor \mathbf{F}_+ and the control-loop duration t .

Concretely, the topological energy-transport factors \mathbf{F}_\pm between the two motional normal modes are plotted as a function of the control-loop duration τ in the LHS-driving [i.e., a_L , see the blue curves in Fig. S5(a)], the standard [i.e., non-spinning, see the green curves in Fig. S5(b)], and the-RHS driving [i.e., a_R , see the red curves in Fig. S5(c)] cases. We find that with rapidly encircling the EP, i.e., $\tau \rightarrow 0$, no energy transfer occurs, i.e.,

$$\mathbf{F}_+ \rightarrow 1 \quad \text{and} \quad \mathbf{F}_- \rightarrow 0; \quad (\text{S55})$$

while with adiabatically winding around this EP, an excellent phonon transport is realized, i.e.,

$$\mathbf{F}_+ \rightarrow 0 \quad \text{and} \quad \mathbf{F}_- \rightarrow 1, \quad (\text{S56})$$

which strongly depends on the duration of the enclosing-EP adiabatic paths. Remarkably, we find that the threshold control-loop duration for preserving a perfect energy transfer, in the RHS (LHS) driving, is nearly 5 (2.5) times faster (slower) than that in the standard case. This indicates that the topological energy transfer can be speed-up but also speed-down, which paves a route to realizing the speed-controllable topological transfer of phonons.

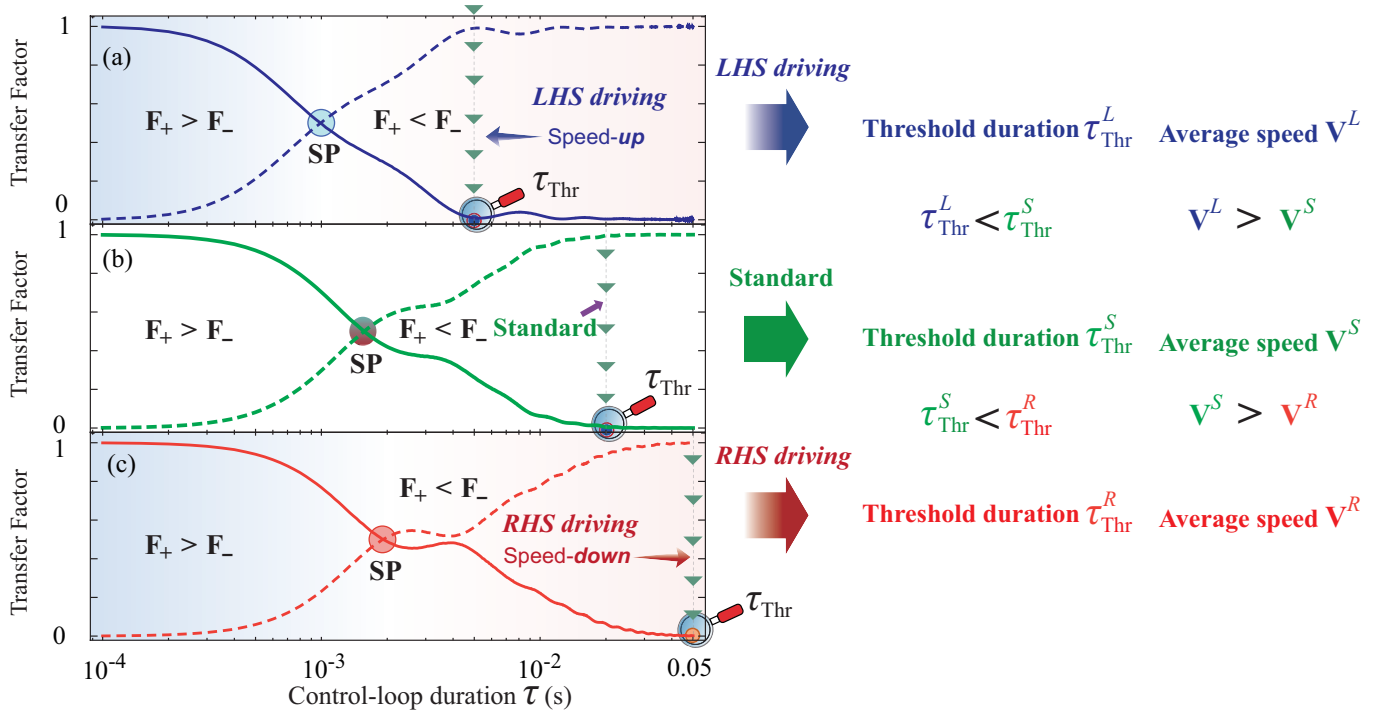


FIG. S5: Topological-energy-transfer quality factor \mathbf{F}_{\pm} versus the control-loop duration τ of executing the closed control loops for: (a) the LHS-driving (see the blue curves), (b) standard (see the green curves), and (c) RHS-driving (see the red curves) cases. In addition, we show the correspondence of the threshold duration τ_{Thr} of the closed adiabatic control loops and the average speed V of the topological energy transfer in the LHS-driving, standard, and RHS-driving cases. We find $\tau_{\text{Thr}}^L < \tau_{\text{Thr}}^S < \tau_{\text{Thr}}^R$ and $V^L > V^S > V^R$.

To clearly demonstrate this counterintuitive behavior, we show the relationship between \mathbf{F}_{+} and τ_{Thr} , and define an average speed of the energy transport:

$$\begin{cases} 0 < \mathbf{F}_{+}(\tau) \leq 1, & (\tau < \tau_{\text{Thr}}) : \text{no or partial topological energy transfer;} \\ \mathbf{F}_{+}(\tau) = 0, & (\tau \geq \tau_{\text{Thr}}) : \text{optimal topological energy transfer;} \end{cases} \quad (\text{S57})$$

and

$$\mathbf{V} = \tau_{\text{Thr}}^{-1}. \quad (\text{S58})$$

Moreover, we analytically show the relationship between the topological-energy-transfer factors $\mathbf{F}_{\pm}(t)$ and the switching-point time τ_{SP} corresponding to the symmetrical energy transfer:

$$\begin{cases} (i) \mathbf{F}_{+}(\tau) > \mathbf{F}_{-}(\tau), & \text{when } \tau < \tau_{\text{SP}}; \\ (ii) \mathbf{F}_{+}(\tau) = \mathbf{F}_{-}(\tau), & \text{when } \tau = \tau_{\text{SP}}; \\ (iii) \mathbf{F}_{+}(\tau) < \mathbf{F}_{-}(\tau), & \text{when } \tau > \tau_{\text{SP}}. \end{cases} \quad (\text{S59})$$

Specifically, we see from Eq. (S59) that: (i) when the duration τ of a control loop is smaller than the switch-point time τ_{SP} , the energy of the b_{+} mode is larger than that of b_{-} ; (ii) when the duration τ of a control loop is equal to the switch-point time τ_{SP} , the energy of the b_{+} is equal to that of b_{-} ; and (iii) when the duration τ of a control loop is larger than the switch-point time τ_{SP} , the energy of the b_{+} mode is smaller than that of b_{-} .

The dependence of the energy-transfer speed on the Sagnac effect can also be seen by plotting the topological energy-transport performances \mathbf{F}_{+} (see the solid curves) and \mathbf{F}_{-} (see the dashed curves) versus the control-loop duration τ of the trajectories when the system operates in the LHS driving [see the blue curves in Fig. S5(a)], the standard [see the green curves in Fig. S5(b)], and the RHS driving [see the red curves in Fig. S5(c)], for the spinning angular velocity $S = 800$ or 0 Hz of the silica sphere. We find that in the LHS-driving (i.e., a_L) regime, both switch-point time τ_{SP} and threshold duration τ_{Thr} are shifted to the left, which leads to a speedup for the topological phonon transport. Especially, the speed-up time is associated with the value of the angular velocity S , corresponding to the emergence of a strong Sagnac effect. However, in the RHS-driving (i.e., a_R) regime, both τ_{SP} and τ_{Thr} are shifted to the right, which shows an opposite phenomenon compared with the LHS-driving, and this means that the topological phonon transfer is slowed down which is switched from being speed-up. In particular, we also show in the

TABLE I: (a) Correspondence of the threshold duration τ_{Thr} of the adiabatic closed control loops (column 2) and the average speed V of the topological energy transfer (column 3) in the LHS-driving, standard, and RHS-driving cases (column 1). (b) Correspondence of the topological energy-transfer factor \mathbf{F}_+ when the time t of the closed control loops is smaller than τ_{Thr} (column 2, corresponding to no or partial energy transfer), τ is equal to τ_{Thr} (column 3, corresponding to an excellent transfer of energy), and τ is larger than τ_{Thr} (column 4, corresponding to a perfect energy transfer). (c) Correspondence of \mathbf{F}_+ when the time τ of the control loops is smaller than the switch-point duration τ_{SP} of the adiabatic control loops (column 2, corresponding to an asymmetric energy transfer), τ is equal to τ_{SP} (column 3, corresponding to a symmetric energy transfer), and τ is larger than τ_{SP} (column 4, corresponding to an asymmetric energy transfer).

(a)	Threshold duration τ_{Thr} of adiabatic control loops		Average speed V of energy transfer	
LHS-driving	Time shortened		Speed-up	
Standard case	Standard		Constant speed	
RHS-driving	Time prolonged		Speed-down	

(b)	$\tau < \tau_{\text{Thr}}$	$\tau = \tau_{\text{Thr}}$	$\tau > \tau_{\text{Thr}}$
Topological transfer	$0 < \mathbf{F}_+ \leq 1$	$\mathbf{F}_+ = 0$	$\mathbf{F}_+ = 0$
performance	No or partial transfer	Perfect transfer	Perfect transfer

(c)	$\tau < \tau_{\text{SP}}$	$\tau = \tau_{\text{SP}}$	$\tau > \tau_{\text{SP}}$
Topological transfer	$\mathbf{F}_+ > \mathbf{F}_-$	$\mathbf{F}_+ = \mathbf{F}_-$	$\mathbf{F}_+ < \mathbf{F}_-$
performance	Asymmetric	Symmetric	Asymmetric

right side of Fig. S5(a,b,c) that the threshold duration τ_{Thr} for maintaining the optimal transfer performance (the average speed V of topological energy transfer) becomes much larger (smaller) from the LHS-driving, standard, to RHS-driving cases. These results are matched well with the following detailed analysis.

To understand this more intuitively, in Table. I(a), we show the correspondence of the threshold duration τ_{Thr} of the adiabatic control loops (see column 2) and the average speed V of topological energy transfer in the LHS-driving, standard, and RHS-driving cases. We find that in the LHS-driving regime, the threshold duration τ_{Thr} for maintaining an optimal topological transfer of energy can be easily shortened, which leads to a speed-up of the topological phonon transport; while in the RHS-driving regime, the threshold duration τ_{Thr} is prolonged, which means a speed-down of topological energy transfer. These findings indicate that the topological transfer of phonons can be speed-up but also speed-down, which paves a route to a speed-tunable topological phononics. Moreover, we show in Table I(b) the topological phonon-transfer factors \mathbf{F}_+ when $\tau < \tau_{\text{Thr}}$, $\tau = \tau_{\text{Thr}}$, and $\tau > \tau_{\text{Thr}}$, correspond to no or partial topological energy transfer, and a perfect topological transfer of energy, respectively.

In addition, we show in Table. I(c) the correspondence of the topological phonon-transfer factor \mathbf{F}_+ when the time τ of the closed control loops is smaller than the switch-point duration τ_{SP} of the control loops, i.e., $\tau < \tau_{\text{SP}}$, which leads to an asymmetric energy transfer, the time of control loops τ is equal to the switching-point duration τ_{SP} of the enclosed control loops, i.e., $\tau = \tau_{\text{SP}}$, associated with a symmetric energy transfer, and the time of control loops τ is larger than the switching-point duration τ_{SP} of the adiabatic control loops, i.e., $\tau > \tau_{\text{SP}}$, which is related to an asymmetric transfer of energy. These findings show the threshold duration of the adiabatic control loops for maintaining optimal energy transfer can be easily prolonged or even shortened, yielding a speed-tunable topological transfer that has no counterpart in previously established demonstrations. Our study paves a quite-general route to exploiting profoundly different topological chirality, both independent of the EP-encircling direction and immune to the masses of practical devices.

E. Topological energy transfer immune to device quality factors

In this subsection, we show in detail how to realize the topological transfer of phonons with the immunity of the quality factors of practical devices. Below, we demonstrate this step by step.

Our approach proposed here not only paves a feasible route for shielding topological resources from the quality factors of practical devices, but also enable the construction of loss-tolerant one-way acoustic devices. In practical devices, the motional

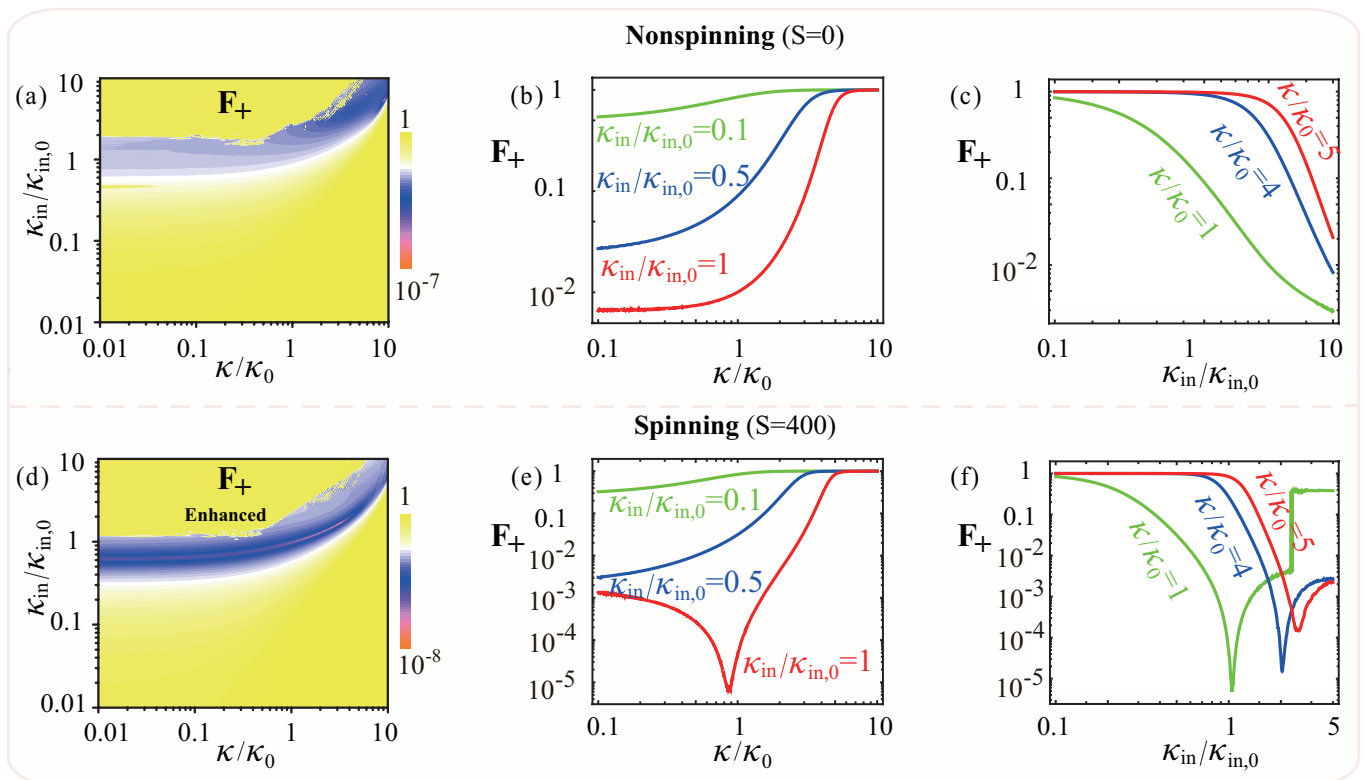


FIG. S6: In the (a-c) standard (i.e., nonspinning) and (d-f) spinning (i.e., LHS-driving, a_L) cases, topological phonon-transfer quality factor F_+ versus the dissipation rate κ and the input coupling rate κ_{in} of the silica microsphere. F_+ versus (b,e) κ when $\kappa_{in}/\kappa_{in,0} = 0.1$ (green curves), 0.5 (blue curves), and 1 (red curves), and versus (c,f) κ_{in} when $\kappa/\kappa_0 = 1$ (green curves), 4 (blue curves), and 5 (red curves), in both standard and spinning cases. Here we assume $\kappa_0/\omega_1 = 0.225$ and $\kappa_{in,0}/\omega_1 = 0.089$, and other parameters are the same as those in Fig. S1.

modes will be thermalized by their thermal baths through their mechanical-decay channels and therefore, the thermal noise can destroy all the topological energy transfer in quantum devices. In addition, a larger cavity-field decay rate in practical quantum devices correspond to a smaller cavity-photon number, which leads to a much worse performance of topological energy transport. Next, we study in detail the dependence of the topological phonon transfer on the cavity-field decay rate κ , the input coupling rate κ_{in} , and the mechanical damping rate γ_2 .

First, we study the effect of the dissipation rate κ and the input coupling rate κ_{in} of the cavity field on the topological energy transfer F_+ , when the system operates in both standard (i.e., non-spinning) and spinning (i.e., LHS-driving, a_L) cases. Concretely, we plot in Figs. S6(a) and S6(d) the topological energy-transfer performance F_+ as functions of the rescaled the total dissipation rate κ and the input coupling rate κ_{in} of the cavity field, in both non-spinning and spinning cases. We clearly see that the topological phonon-transfer performance in the spinning case is much better than that in the standard (i.e., nonspinning) case. In addition, we find that with the increase of the cavity-field decay κ , the topological-energy-transport performance becomes much worse, i.e., $F_+ \rightarrow 1$, while it will become much better for a larger value of κ_{in} , as shown in Figs. S6(b) and S6(e). Especially, we reveal that a more than three-orders-of-magnitude improvement in the topological phonon-transfer performance can be observed with our proposed method, without which it vanishes. In particular, we find that the topological energy transfer can be realized when the system is only in the resolved-sideband regime, i.e., $\kappa \ll \omega_m$, and that the optimal working parameter of the cavity-field decay rate κ (corresponding to the optimal value of F_+) is around $\kappa/\kappa_0 \approx 1$, where the topological energy-transfer performance can be three orders of magnitude better than that in the standard (i.e., nonspinning) case.

As is well-known, the thermal baths thermalize vibrational modes via their decay channels, and then the topological energy transfer is usually easily destroyed by the thermal noise in practical quantum systems. To further study and understand these thermalization effects, we specifically show the topological-energy-transfer factor F_+ as functions of the mechanical decay rate γ_2 of quantum practical devices, when the system operates in both non-spinning (i.e., standard) and spinning (i.e., LHS-driving, a_L) cases. We find that the topological energy transfer in the spinning case is much better than that with the standard schemes. For example, the topological-energy-transfer performance can be nearly two orders of magnitude better than that in the standard demonstrations. Moreover, we see that the topological energy-transfer performance becomes much worse with the increase of the mechanical decay rate γ_2 of mechanical devices. Physically, the thermal-noise-exchange rates between the mechanical vibrations and their heat baths are much slower for a smaller value of the mechanical damping rate γ_2 , and it is good for immunizing all the

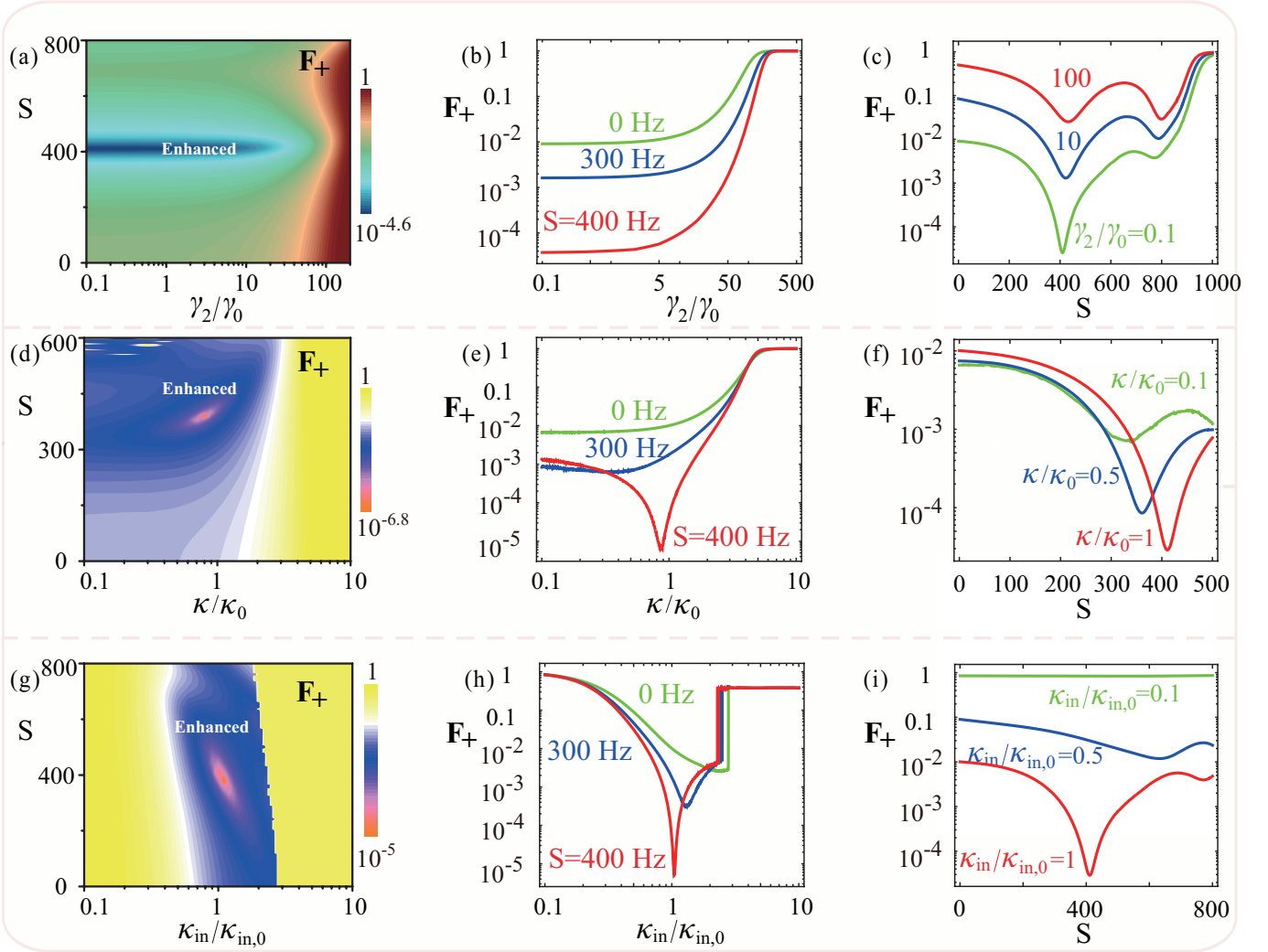


FIG. S7: (a) Topological energy-transfer quality factor \mathbf{F}_+ versus the mechanical damping rate γ_2 and the rotating angular velocity S of the silica microsphere, for $\gamma_0/\omega_1 = 1.78 \times 10^{-6}$. (d) \mathbf{F}_+ versus κ and S . (g) \mathbf{F}_+ versus κ_{in} and S . \mathbf{F}_+ versus (b) γ_2 , (e) κ , and (h) κ_{in} when $S=0, 300$, and 400 Hz. (c) \mathbf{F}_+ versus S when $\gamma_2/\gamma_0=0.1, 10$, and 100 . (f) \mathbf{F}_+ versus S when $\kappa/\kappa_0=0.1, 0.5$, and 1 . (i) \mathbf{F}_+ versus S when $\kappa_{in}/\kappa_{in,0}=0.1, 0.5$, and 1 . Here we assume $\kappa_0/\omega_1 = 0.225$ and $\kappa_{in,0}/\omega_1 = 0.089$, and other parameters are the same as those in Fig. S1.

topological phonon transfer against the environmental thermal perturbations. This indicates that a higher Q -factor mechanical resonator can be beneficial for generating a high-performance topological transfer of phonons. We also demonstrate that a two-orders of magnitude improvement in the energy-transfer performance can be observed by introducing the Fizeau light-dragging effect (i.e., for $S \neq 0$), which yields an excellent topological energy transfer (i.e., corresponding to the minimum value of \mathbf{F}_+) resulting from a smaller the mechanical decay rate γ_2 .

More importantly, the generating nonreciprocal topological transfer of energy, in the independence on the EP-encircling directions, can provide a novel way to enabling practical bad-quality setups to be ideal, and it is reminiscent of that in chiral environment and topological devices. In Figs. S7(a-f), we plot the topological phonon transfer performance \mathbf{F}_+ of the two motional normal modes as functions of either the spinning angular speed S and the cavity-field decay rate κ or the mechanical damping rate γ_2 in practical quantum devices. We observe that with increasing the decay rates κ or γ_2 , the topological energy-transfer performance \mathbf{F}_+ reaches an optimal value around the spinning angular velocity $S \approx 400$, which is related to an excellent topological phonon transfer between the two vibrational normal modes. In addition, we highlight that the topological energy transfer can be achieved for both good- and bad-quality devices, and this means that the decay-immune topological energy transfer can be realized by simply employing the Fizeau light-dragging effect.

To further demonstrate these counterintuitive phenomena which are above mentioned, we show in Figs. S7(c), S7(f), and S7(i) the topological energy-transfer performance \mathbf{F}_+ versus the angular velocity S of the spinning silica sphere, in both good- and bad-quality regimes. It demonstrates that in the bad-quality regime, the topological phonon transfer nearly does not occur almost

at all, i.e., $\mathbf{F}_+ \rightarrow 1$, for the standard (i.e., nonspinning) case, but it becomes feasible, i.e., $\mathbf{F}_+ \rightarrow 0$, for the spinning case (i.e., a_L). In particular, we reveal that the topological-energy-transfer performance becomes much better for a larger value of the angular velocity S of the silica sphere. For example, in the bad-quality regime, the topological phonon-transport performance for the spinning case has been predicted to be 10 (5) times better than those in the nonspinning case. In the good-quality regime, with the decrease of the decay rate κ (γ_2) of quantum devices, an excellent topological energy transfer in the spinning case can be effectively achieved and its topological transfer performance can be improved up to 2.5 (3) orders of magnitude compared with that in the standard scheme (i.e., $S = 0$). These findings show that the application of the Fizeau light-dragging effect to the topological operations can not only lead to a giant enhancement for the isolation, but also indicate the possibility of achieving excellent topological transfer of energy, which is fully beyond the limitations of the quality factors of practical quantum devices.

F. Strength-dependent topological transfer of energy

In this subsection, we show in detail the effect of the light-motion coupling strengths on the topological energy transfer, and demonstrate how to achieve an optimal strength-dependent topological energy transfer via the Fizeau light-dragging effect.

Specifically, we plot the topological-energy-transfer quality factor \mathbf{F}_+ as functions of the optomechanical-coupling strengths g_1 and the spinning angular velocity S of the silica microsphere, as shown in Fig. S8(a). We find that the topological energy-transfer performance in the spinning device is much better than that in the non-spinning case. For example, the phonon-transfer performance in the spinning regime can be three orders of magnitude better than that with the standard method. In the non-spinning regime (i.e., $S = 0$), we see that the topological energy-transfer performance is significantly suppressed with decreasing the optomechanical coupling strength g_1 . In contrast, an opposite phenomenon of the topological energy transfer emerges when switching to the spinning regime from the standard (i.e., non-spinning) regime, and especially, the topological phonon-transfer performance in the spinning regime is largely better than that in the nonspinning regime, as shown in Fig. S8(b). These results indicate that, in the finite region a higher spinning angular velocity of the silica sphere leads to a much stronger Fizeau-drag strength of the light, which can be useful for generating a higher-performance topological transfer of phonons. Moreover, we find that a three orders of magnitude improvement in the energy-transfer performance can be observed by introducing the Fizeau drag of light (i.e., $S \neq 0$).

In addition, in Fig. S8(a) exhibiting the topological energy transfer \mathbf{F}_+ versus the light-motion coupling strength g_1 and the spinning angular velocity S , we show that for the conventional (i.e., nonspinning) scheme, i.e., $S = 0$, no topological energy transfer happens, i.e., $\mathbf{F}_+ \rightarrow 1$, when the optomechanical-coupling strength satisfies $g_1/g_0 < 1$. In stark contrast to this, by introducing the Fizeau light-dragging effect, i.e., $S \neq 0$, an excellent topological transfer of phonons can be achieved no matter how large or small the light-vibration coupling strengths are, i.e., $\mathbf{F}_+ \rightarrow 0$ (see the blue and orange regions in Fig. S8). These results indicate that, in general, by simply employing the Fizeau drag of light, the topological energy transfer can be nearly independent of the coupling strengths between the vibrational modes and the optical mode.

To further show the *immunity* of our approach to engendering the topological energy transfer against the worse strengths of optomechanical couplings, we make a detailed comparison between the previous standard method (see the blue solid curves) and our proposal (see the red curves), as shown in Fig. S8(c). We find that with decreasing the light-vibration coupling strength g_1 , the topological phonon-transfer performance becomes much worse, i.e., $\mathbf{F}_+ \rightarrow 1$; while counterintuitively, introducing the Fizeau light-dragging effect can allow to reach the coupling-immune topological transfer of phonons, i.e., $\mathbf{F}_+ \rightarrow 0$, which was very challenging for the previous demonstrations. This is because the topological transfer performance is reduced due to decreasing the light-motion coupling strength, while it can be tremendously compensated or even amplified by employing the Fizeau-Sagnac mechanism. Our findings indicate that our study paves a route towards exploiting one-way topological phononics, which is immune to the light-motion coupling strengths.

In order to demonstrate the underlying physical mechanism behind these counterintuitive phenomena, we derive the analytical expressions of both the effective light-vibration coupling strength and the mean photon numbers:

$$G_j^{R,L} = g_j \sqrt{N_{R,L}/\rho_j}, \quad (\text{S60})$$

$$N_{R,L} = \frac{P\kappa_{\text{in}}}{(-i\Delta_{R,L} + \frac{\kappa}{2})(i\Delta_{R,L} + \frac{\kappa}{2})\omega_{R,L}\hbar}, \quad (\text{S61})$$

where the parameter $\rho_j = m_j/m_0$ is the ratio of the masses of resonators. We see from Eqs. (S60) and (S61) that the effective optomechanical coupling $G_j^{R,L}$ decreases due to increasing the mass ratio ρ_j , however, the application of the Sagnac effect leads to a significant compensation or even an enhancement in the photon numbers, which considerably compensates or even amplifies the light-vibration coupling strengths, as shown in Figs. 2(c) and 2(d) of the main text. Note that the main idea is analogous to the non-topological nonreciprocity induced by the Doppler effect, which has been studied extensively in various areas of physics [S27, S28]. Here we focus on topological nonreciprocity induced by the Fizeau light-dragging effect. These findings mean that the large-mass-induced reflection can be significantly suppressed by employing the Fizeau drag of the light, and as a result, one can achieve a nearly ideal topological transfer of energy.

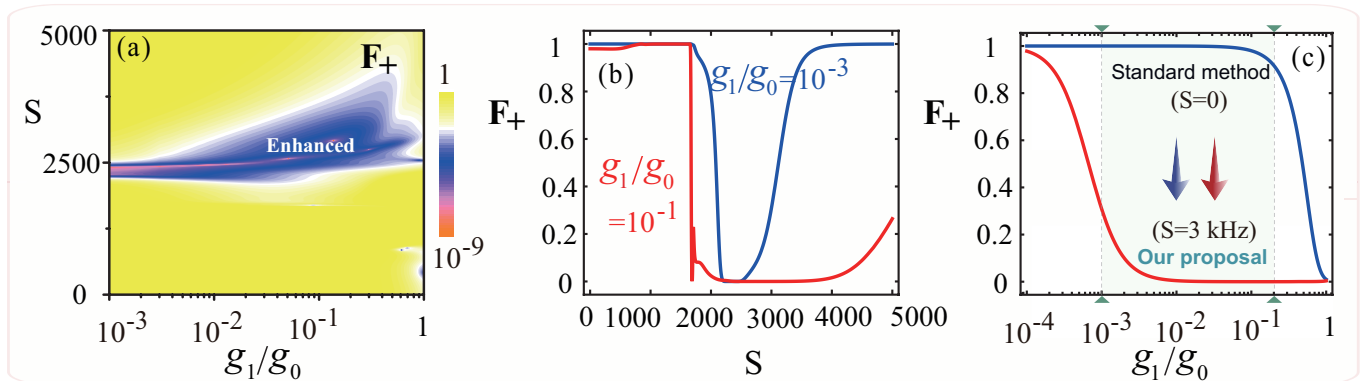


FIG. S8: (a) Topological-energy-transfer quality factor F_+ versus the optomechanical-coupling strength g_1 and the spinning angular velocity S of the silica microsphere, for $g_0/\omega_1 = 1.31 \times 10^{-6}$. (b) F_+ versus S when $g_1/g_0 = 10^{-3}$ (blue curve) and 10^{-1} (red curve). (c) F_+ versus g_1/g_0 when $S=0$ (blue curve) and 3 kHz (red curve). Other parameters are the same as those in Fig. S1.

In particular, to obtain an excellent topological energy transfer, i.e., $F_+ < 0.01$, via the Fizeau drag of the light, we found the analytical expressions on the relationship between the resonator mass ratio ρ and the threshold spinning angular speed S_{Thr} of the silica sphere:

$$S_{\text{Thr}} = \left[-\Delta \pm \sqrt{[4\Delta^2 - (\rho - 1)\kappa^2]/(4\rho)} \right] / \Lambda, \quad (\text{S62})$$

It shows that keeping an optimal topological phonon transfer for a larger value of the resonator mass ratio ρ requires a higher spinning angular speed S of the silica sphere, which is consistent with the results in Fig. S8.

Specifically, we find that for the standard (i.e., nonspinning) scheme, the optomechanical-coupling strengths decrease with increasing the mass of the resonators; while for a rotating device, it is significantly enhanced or even amplified, compared with that in the former case. This counterintuitive phenomenon can be understood via an enhancement in effective photon numbers in the cavity. We show in detail that the effective photon numbers become less with the increase of the mass of the resonators in the non-rotating case. In contrast to this, we reveal that in the spinning case, a multiple orders-of-magnitude amplification in the photon numbers arises from the Sagnac effect, without which it vanishes. These results indicate that the mass-induced reflection can be significantly suppressed in a spinning device and as a result, one can achieve a nearly ideal topological transfer of phonons.

G. Eigenvalue distributions and transient behaviors around EP for different laser powers

Here, we show in detail the eigenvalues distributions around EP for different laser powers, and exhibit the transient behavior of the investigated systems not only in time domain but also in the parameter space, as shown in Figs. S9 and S10.

Firstly, we provide a detailed depiction of the eigenvalue distributions around the EP for various laser powers. Physically, the real and imaginary parts of the complex eigenvalues of the two motional normal modes are the resonance frequencies, $\omega_{\pm}^{R,L}(\Delta, P) = \text{Re}(\lambda_{\pm}^{R,L})$, and the linewidths, $\gamma_{\pm}^{R,L}(\Delta, P) = -2\text{Im}(\lambda_{\pm}^{R,L})$, respectively. Note that in our model, the control of the optomechanical system is achieved by a separate laser, and its driving power P and driving detuning Δ are set by an acousto-optic modulator. The vibration spectra of the mechanical motions as functions of the driving detuning Δ and the driving power P can be measured, so that the presence of the EP in our system can be accurately established. In addition, these spectra are acquired by driving the vibrations and monitoring its response via a heterodyne signal. We fit each spectrum to determine the two motional damping rates, $\gamma_{\pm}^{R,L}(\Delta, P)$, and the two vibrational resonance frequencies, $\omega_{\pm}^{R,L}(\Delta, P)$. Note that the subscripts “ \pm ” refer to the vibrational normal modes of the resonators, when the optical field is introduced to the physical system.

Specifically, we see from Figs. S9(a) and S9(b) that, when $P < P_{\text{EP}} \approx 185$ uW, the eigenfrequencies have two different real parts (i.e., $\text{Re}[\tilde{\lambda}_-] > \text{Re}[\tilde{\lambda}_+]$) and an identical imaginary part (i.e., $\text{Im}[\tilde{\lambda}_-] = \text{Im}[\tilde{\lambda}_+]$). This indicates that the system possesses two different mechanical frequencies and an identical mechanical linewidth, as shown in the left-hand sides of Figs. S9(a) and S9(b). In addition, Figs. S9(a) and S9(b) show that when $P > P_{\text{EP}}$, the eigenfrequencies have two different real parts (i.e., $\text{Re}[\tilde{\lambda}_-] < \text{Re}[\tilde{\lambda}_+]$) and two different imaginary parts (i.e., $\text{Im}[\tilde{\lambda}_-] > \text{Im}[\tilde{\lambda}_+]$). This means that both mechanical frequencies and mechanical linewidths are different, as shown on the right-hand sides of Figs. S9(a) and S9(b). In particular, it is seen that the phase transition of the system is clearly exhibited around the border point $P = P_{\text{EP}} \approx 185$ uW, which is an EP [see the yellow discs in Figs. S9(a) and S9(b)]. Here we note that it is a semiclassical EP, corresponding to a spectral degeneracy of a

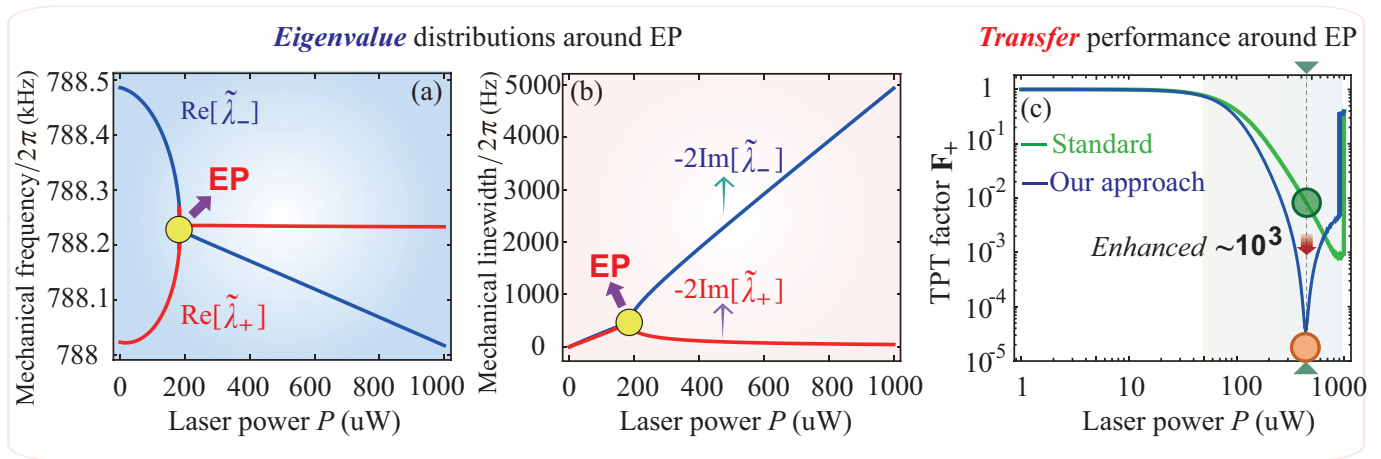


FIG. S9: Complex eigenvalues of the two motional modes. (a) Mechanical resonance frequencies $\text{Re}[\tilde{\lambda}_{\pm}]$ and (b) mechanical decay rates $-2\text{Im}[\tilde{\lambda}_{\pm}]$ of the two motional modes as a function of the driving laser power P , when the system is driven by a laser from the left-hand side (LHS) of the fibre, for the driving detuning $\Delta/(2\pi) = -1020.99$ kHz and the angular velocity $S = 400$ Hz of the spinning silica microsphere. By tuning the laser power P , the EP occurs which is described by the yellow discs. (c) Topological phonon transfer (TPT) quality factor as a function of the driving laser power P for the standard method (i.e., $S = 0$ Hz, see the green curves) and our approach (i.e., $S = 400$ Hz when light enters from the LHS of the fiber, see the blue curves). The TPT behavior in our approach shows an agreement with the standard results, i.e., the adiabatic trajectories enclosing the EP will yield the TPT, whereas the adiabatic paths not enclosing the EP will not. In addition, the topological energy transfer in our method (spinning) case is much better than that with the standard (non-spinning) schemes. For example, the topological-energy-transfer performance can be nearly *three orders of magnitude* better than that in the standard demonstrations. Our analyses indicate that the present scheme is experimentally accessible under current experimental conditions, and that the proposed phenomena are relevant for the state-of-the-art experiments. Specifically, the mechanical frequencies and the mechanical linewidths are, respectively, denoted by the real and imaginary parts of $\tilde{\lambda}_{\pm}$. Specifically, we see that when $P \neq P_{\text{EP}}$, the eigenfrequencies have two different real parts, and that when $P < P_{\text{EP}}$ ($P > P_{\text{EP}}$), we obtain $\text{Re}[\tilde{\lambda}_{-}] > \text{Re}[\tilde{\lambda}_{+}]$ ($\text{Re}[\tilde{\lambda}_{-}] < \text{Re}[\tilde{\lambda}_{+}]$). Moreover, it shows that for $P = P_{\text{EP}}$, the eigenfrequencies have an identical real part, i.e., $\text{Re}[\tilde{\lambda}_{-}] = \text{Re}[\tilde{\lambda}_{+}]$. In addition, we find that when $P < P_{\text{EP}}$ and $P > P_{\text{EP}}$, the eigenfrequencies have an identical imaginary part and two different imaginary parts, respectively. This indicates that when $P < P_{\text{EP}}$ and $P > P_{\text{EP}}$ the system possesses two different mechanical frequencies and an identical mechanical linewidth (two different mechanical linewidths), respectively. In particular, the EP (e.g., at $P = P_{\text{EP}}$, see yellow discs), where the eigenstates coalesce, emerges due to switching the laser powers P .

non-Hermitian Hamiltonian. However, for the prediction of a quantum EP, it requires the inclusion of quantum noise by finding degeneracies of, e.g., a Liouvillian, as proposed in Ref. [S29].

Now, we detailedly show the transient behavior of our investigated systems **not only** (i) in the time domain **but also** (ii) in the parameter space. In principle, to demonstrate the transient behavior of the studied systems, it is indeed appropriate to plot the TPT performance versus time. However, in our case, the TPT is resulted from the dynamical encirclement of the EP in the parameter space (e.g., the detuning Δ and power P of the driving laser). Therefore, we here study the dynamic behavior not only (i) in the time domain but also (ii) in the parameter (Δ and P) space, because it encapsulates the transient characteristics of the TPT when the EP is encircled by closed trajectories in this parameter space (Δ and P). We believe that this approach offers a comprehensive understanding of the system's dynamics and evolution, as it provides insights into the interplay between the TPT performance and the parameter space dynamics.

(i) In the time domain, the TPT dynamics can be seen in Fig. S10. We reveal that by rapidly encircling the EP ($\tau \rightarrow 0$), no TPT happens ($F_{+} \rightarrow 1$, $F_{-} \rightarrow 0$); while with adiabatically winding around this EP ($\tau \gg 1$ ms [S12]), an excellent TPT is observed ($F_{+} \rightarrow 0$, $F_{-} \rightarrow 1$). Remarkably, in the LHS-injecting case, the *threshold* duration τ_{Thr} of the adiabatic control loops for preserving a perfect TPT, is nearly 5 times less than that in the standard schemes. Note that the threshold duration corresponds to a *top speed* of the perfect TPT. These findings pave a route to a top-speed tunable TPT.

(ii) In the parameter space, the transient behavior can be illustrated in Figs. S9(c). Specifically, we plot the TPT quality factor F_{+} as a function of the driving laser power P with the standard method (i.e., $S = 0$ Hz, see the green curves) and our approach (i.e., $S = 400$ Hz, when injecting light from the LHS of the fiber, see the blue curves), as shown in Fig. S9(c). We reveal that the TPT behavior with our method agrees with that in the standard situation, where the adiabatic trajectories enclosing the EP will yield the TPT, whereas the adiabatic paths not enclosing the EP will not. Moreover, we find from in Fig. S9(c) that with our method, the TPT performance can be improved up to 3 orders of magnitude compared with that in the standard scheme. This demonstrates that a giant improvement in the TPT performance can be observed by introducing the Fizeau light-dragging effect, which yields an excellent TPT (i.e., $F_{+} \rightarrow 0$). Note that the TPT quality factor F_{+} versus the driving detuning Δ has been studied in detail, as shown in Fig. (1c) of the main text. These results show that the application of the Fizeau light-dragging effect to the topological operations can lead not only to a giant enhancement for the isolation, but also indicate the possibility of achieving

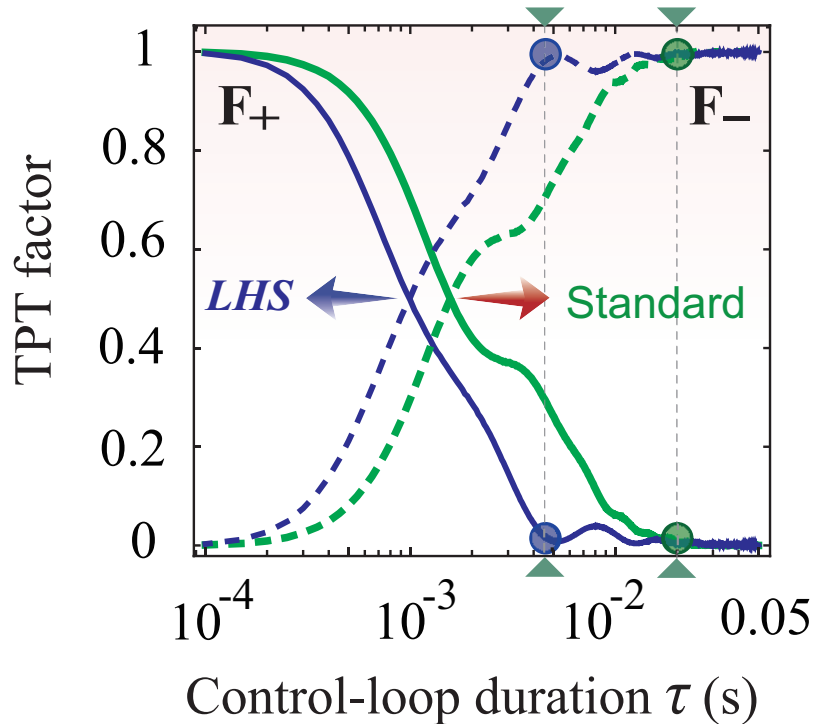


FIG. S10: F_+ (solid curves) and F_- (dashed curves) versus the control-loop duration τ in the standard (green curves) and LHS-driving (blue curves) cases when $S = 800$ Hz.

an excellent topological transfer of energy, which is fully beyond the limitations of the present practical quantum devices.

H. Temperature effect on the nonreciprocal topological phonon transfer

In cavity optomechanics, a high temperature can dramatically suppress the TPT performance. Based on the previous well-known experimental demonstrations focusing on the semi-classical EP [S12, S30–S33], the cryogenic optomechanical platforms can be employed in practical experiments to minimize the impact of temperature. In these mature experimental studies [S12, S30–S33], even though considering the semi-classical EP, the experimental results are in complete agreement with theoretical predictions. Note that our method dealing with the temperature effect on the nonreciprocal TPT are entirely based on these well-established experimental works [S12, S30–S33]. In addition, in practical experimental setups, it is essential to monitor and control the temperature of the system accurately [S12, S30–S33]. This is because the changes in temperature can alter the dynamics of the optomechanical system and influence the observed nonreciprocal TPT. In our scheme, building upon widely recognized experimental works [S12, S30–S33], we conduct a comprehensive and detailed analysis of how to suppress the impact of the temperature effects on the TPT performance. In particular, we have briefly shown how to consider the temperature effect on the nonreciprocal TPT by studying the quantum EPs of non-Hermitian Hamiltonians and Liouvillians [S29].

Firstly, we show not only in detail how the nonreciprocal TPT is affected by the environment temperature, based on the following four aspects, and but also exhibit how to minimize the impact from the temperature effect by using widely recognized experimental methods [S12, S30–S33].

(i) Thermal vibrations and expansion: At finite temperatures, the mechanical resonators will experience thermal vibrations. The temperature of the system affects the phonon occupation numbers and, consequently, the mechanical noise in the system. In particular, the environmental vibrations add unwanted noise to the measurement of the mechanical motion, as well as introduce cavity frequency noise which can be difficult for the laser feedback to track. As the temperature increases, the population of thermal phonons in the mechanical resonator also increases. This can affect the overall dynamics of the system, including the nonreciprocal TPT. In addition, changes in temperature can lead to thermal expansion or contraction of the materials in the optomechanical system. This can alter the mechanical properties of the resonators, affecting the phonon frequencies and topological characteristics of the system. Thermal expansion and contraction of the material can induce strain variations, affecting the optomechanical coupling and the overall phonon transfer properties.

(ii) Thermalization and equilibrium: At higher temperatures, achieving and maintaining thermal equilibrium becomes

important. The system's behavior, including nonreciprocal topological phonon transfer, needs to be analyzed in the context of thermalization processes. In this case, the mechanical modes of the system are thermalized by the high environmental temperature, which affects the nonreciprocal transfer of phonons in the system.

(iii) Dissipation and decoherence: Temperature can influence the damping mechanisms in the system. Higher temperatures typically lead to increased dissipation, affecting the lifetime and coherence of mechanical excitations. This, in turn, can impact the nonreciprocal behavior of the phonon transfer. Moreover, higher temperatures generally lead to increased thermal noise and dissipation in the mechanical resonator. This can affect the coherence and nonreciprocal behavior of the phonon transfer.

Based on the above facts that the environmental temperature made a destructive impact on the nonreciprocal TPT, during practical experiments, we can utilize the cryogenic optomechanical platforms to minimize the impact from the temperature effect as much as possible [S12, S30–S33]. Furthermore, in practical experimental devices, precise monitoring and controlling system's temperature are crucial. This is due to the fact that the temperature can impact the dynamics of the optomechanical system, thereby influencing the nonreciprocal TPT. Below, drawing on well-established experimental studies, we conduct a thorough and detailed analysis of methods to mitigate the impact of environmental temperature on the performance of TPT. In a well-known experiment [S12] on the standard TPT using two-vibration cavity optomechanics, the practical experimental setup includes the cryogenic optomechanical device (the optical cavity, vibrational modes, and associated support hardware), as well as the optical and electrical systems used to interrogate the optomechanical system. In this cryogenic optomechanical platform, to reduce the thermal occupation of the resonators, the system is housed in a 'wet' ^3He cryostat. The operation of this cryostat relies on a multi-stage system involving evaporative cooling of separate reservoirs of ^3He and ^4He . The outermost layer of the cryostat is a vacuum-jacketed ^4He bath, into which is submersed an inner vacuum chamber containing the refrigeration and experimental device. By pumping/cooling the 1K pot, one triggers condensation of the gaseous He-3, forming a volume of liquid ^3He in the coldest section of the cryostat. A high-surface-area material in the ^3He space (charcoal) results in adsorptive pumping of the ^3He , further reducing its temperature to a 'base' temperature of ~ 300 mK. Considering these facts, cryogenic optomechanical platforms are employed in practical experiments to minimize the impact of temperature effects as far as possible.

Secondly, we now briefly outline the approach to account for temperature effects on the nonreciprocal TPT. This is accomplished through the examination of quantum EPs in non-Hermitian Hamiltonians and Liouvillians [S29]. As is well known, Hamiltonian EPs, in classical and semi-classical methodologies, are typically characterized as degeneracies of non-Hermitian Hamiltonians. This occurs when at least two eigenfrequencies coincide, leading to the simultaneous coalescence of their corresponding eigenstates. The resulting Hamiltonian EPs arise from continuous, predominantly gradual, nonunitary evolution, characterized by the absence of quantum jumps. Certainly, for a fully quantum approach to achieve equivalence with, for instance, the Lindblad master equation approach, it is imperative to incorporate quantum jumps into the framework. Consequently, the EPs can be defined by identifying degeneracies within a Liouvillian superoperator, which encompasses the complete Lindbladian term, thereby introducing the concept of Liouvillian EPs [S29]. This approach can allow for a clearer elucidation of the connections between Hamiltonian EPs and Liouvillian EPs.

In our discussion, we focus on the delineation of EPs within the fully quantum regime, encompassing the incorporation of quantum jumps. Conventional EPs align with the spectra of non-Hermitian Hamiltonians, rendering quantum jumps inconsequential to their manifestation. While Hamiltonian EPs can be formally extended to systems far beyond the semiclassical limit, the pertinent query arises regarding their aptitude in capturing the genuine quantum characteristics of nonconservative systems. Our approach for defining EPs within the quantum regime hinges on scrutinizing the degeneracies in eigenfrequency and eigenstates within the spectra of Liouvillians. Consequently, these EPs are denoted as Liouvillian EPs [S29]. Our methodology draws inspiration from the conventional Lindblad master equation and its quantum trajectory interpretation, encompassing both the continuous and nonunitary dissipation terms $[\Gamma_\mu^\dagger \Gamma_\mu \rho(t) + \rho(t) \Gamma_\mu^\dagger \Gamma_\mu]$, as well as the quantum jump terms $[\Gamma_\mu \rho(t) \Gamma_\mu^\dagger]$. It is noteworthy that the computation of an EP using non-hermitian Hamiltonians incorporates the continuous nonunitary dissipation term but omits the quantum jump term. The pivotal findings of this project revolve around the juxtaposition of the Liouvillian and Hamiltonian EPs.

Specifically, the temporal evolution of an open quantum system, that weakly interacts with a Markovian (memoryless) environment, can be articulated through the Lindblad master equation ($\hbar = 1$):

$$\frac{\partial \rho(t)}{\partial t} = \mathcal{L}\rho(t) = -i[H, \rho(t)] + \sum_{\mu} \mathcal{D}[\Gamma_{\mu}] \rho(t), \quad (\text{S63})$$

where $\rho(t)$ represents the density matrix of the system at time t , and $\mathcal{D}[\Gamma_{\mu}]$ denotes the dissipators linked to the jump operators Γ_{μ} . Meanwhile, \mathcal{L} refers to the Liouvillian superoperator (for a comprehensive discussion on superoperators). The density matrix $\rho(t)$ has the capacity to represent both pure states $|\varphi\rangle\langle\varphi|$ and probabilistic mixtures $\sum_i p_i |\varphi_i\rangle\langle\varphi_i|$. Each dissipator is characterized by the Lindbladian:

$$\mathcal{D}[\Gamma_{\mu}] \rho(t) = \Gamma_{\mu} \rho(t) \Gamma_{\mu}^{\dagger} - \frac{\Gamma_{\mu}^{\dagger} \Gamma_{\mu}}{2} \rho(t) - \rho(t) \frac{\Gamma_{\mu}^{\dagger} \Gamma_{\mu}}{2}. \quad (\text{S64})$$

The Lindblad master equation offers an intriguing interpretation as the time evolution of a system continuously monitored by an environment. In this context, the impact of $\mathcal{D}[\Gamma_{\mu}]$ on the density matrix $\rho(t)$ can be divided into two components within the

quantum-trajectory or quantum-jump approaches: the continuous nonunitary dissipation terms, i.e.,

$$\Gamma_{\mu}^{\dagger}\Gamma_{\mu}\rho(t) + \rho(t)\Gamma_{\mu}^{\dagger}\Gamma_{\mu}, \quad (\text{S65})$$

and the quantum jump terms, i.e.,

$$\mathcal{J}[\Gamma_{\mu}]\rho(t) = \Gamma_{\mu}\rho(t)\Gamma_{\mu}^{\dagger}. \quad (\text{S66})$$

Dissipation accounts for the ongoing losses of energy, information, and coherence from the system into the environment. Meanwhile, the quantum jumps depict the impact of measurements on the state of the system. The term $\mathcal{J}[\Gamma_{\mu}]$ is termed a quantum jump, as in a quantum trajectory approach (such as a wave-function Monte Carlo method Ref. [1]), these terms play a pivotal role in inducing sudden stochastic changes in the wave function. In this context, when provided with a Lindblad master equation elucidating the microscopic physics of a specific system, obtaining the corresponding ‘‘semiclassical limit’’ is straightforward. This involves neglecting the influence of quantum jumps and introducing an effective non-Hermitian Hamiltonian of the form:

$$H_{\text{eff}} = H - i \sum_{\mu} \frac{\Gamma_{\mu}^{\dagger}\Gamma_{\mu}}{2}. \quad (\text{S67})$$

Below, it is noteworthy that the master equation can be reformulated in terms of H_{eff} as depicted below Ref. [S29]:

$$\frac{\partial\rho(t)}{\partial t} = \mathcal{L}\rho(t) = -i[H_{\text{eff}}\rho(t) - \rho(t)H_{\text{eff}}^{\dagger}] + \sum_{\mu} \Gamma_{\mu}\rho(t)\Gamma_{\mu}^{\dagger}. \quad (\text{S68})$$

Consequently, with a non-Hermitian Hamiltonian H_{eff} and the quantum jump terms $\Gamma_{\mu}\rho(t)\Gamma_{\mu}^{\dagger}$, a comprehensive depiction of the quantum dynamics of a dissipative system can be achieved within the Lindblad formalism.

In summary, the temperature effect on nonreciprocal TPT will open avenues for further exploration in combining quantum EPs with the temperature effect on non-reciprocal topology, contributing novel insights to the unique one-way topology. We are optimistic about the potential of integrating this concept, foreseeing its substantial promise for future applications in topological physics. Nevertheless, it is apparent that addressing this thoroughly would necessitate a substantial and time-intensive revision of the current paper. While we acknowledge the importance of the proposed idea, we propose deferring its exploration to our subsequent paper, allowing for a more in-depth investigation and discussion beyond the scope of the current manuscript. Consequently, the project is currently underway by us.

I. Clarifying the relationship between energy bands and topological phonon transfer

We here need to emphasize that in our few-mode (e.g., three-mode) cavity optomechanical systems consisting of two vibrational modes coupled to a common optical mode, the traditional concept of ‘‘energy bands’’ as seen in band structures is not directly applicable. This is because our model is a three-mode optomechanical system not a solid lattice, which refers to the ordered arrangement of atoms, molecules, or ions within the structure of a solid material. Moreover, our few-mode (three-mode) optomechanical system studied here is not the optomechanical lattices and/or optomechanical crystals, which enable the synthesis of non-trivial band structures and have been actively studied in the field of topological phononics [S14, S34]. Note that yet nearly all previous schemes have used optomechanical lattices and/or crystals for studying the TPT. By contrast, new dynamics and applications in the TPT are expected when using few-mode (e.g, three-mode) optomechanics, that is, systems that use a small number of optomechanical degrees of freedom. Our work on the TPT differs from what is known in the optomechanical lattices/crystals (with energy bands), mainly because we are not focused on a one-dimensional (1D) chain with a topological band structure exhibiting topologically protected edge states [S34], a two-dimensional (2D) honeycomb lattice realizing the strained graphene model with edge states [S34], or multiscale optomechanical crystals comprising over 800 cavity-optomechanical elements fabricated on the surface of a silicon microchip [S14], but on the few-mode cavity optomechanical system (without energy bands) consisting of the two vibrational modes coupled to a common optical mode [S12].

So far, in cavity optomechanics, the TPT has been realized by either (i) using optomechanical lattices, through a mechanically mediated coupling, similar to studies of mechanical metamaterials, or (ii) using few-mode optomechanics as studied here through the topological operations encircling an EP:

(i) Specifically, in optomechanical lattices [S14, S34], some theoretical works have predicted a significantly richer and new dynamics, including: topological phases of light and sound, collective and quench dynamics, quantum many-body dynamics and entanglement, and standard TPT. For example, the produced optomechanical lattices demonstrate topological microwave modes in one-dimensional circuit optomechanical chains realizing the Su-Schrieffer-Heeger model, and realize the strained graphene model in a two-dimensional optomechanical honeycomb lattice [S34]. To realize optomechanical lattices that include

the excitation transport, it is imperative that the disorder in the optical (or microwave) cavity is sufficiently small to enable the building of lattice models. This enables one to reconstruct the full underlying lattice Hamiltonian and to directly measure the existing residual disorder. Such optomechanical lattices, accompanied by measurement techniques, offer an avenue to explore collective, quantum many-body and quench dynamics, topological properties and, more broadly, emergent nonlinear dynamics in complex optomechanical systems with a large number of degrees of freedom.

(ii) In few-mode cryogenic optomechanical systems [S12], imposing topological operations encircling an EP on this few-mode system can lead to the nonreciprocal phonon transfer between two vibrational modes. These results open up new directions in system control and the possibility of exploring other dynamical effects related to exceptional points, including the behavior of thermal and quantum fluctuations in their vicinity. Despite achieving significant accomplishments, the previous proposals of one-way TPT strictly depend on the direction of EP-inclusive control loops and is inherently confined to the small-mass regime of practical resonators [S12–S26]. In terms of these long-standing limitations, where the unidirectional topological physics is not only dependent on the EP-encirclement direction but also can be easily destroyed in the large-mass regime, the exploitation of a new nonreciprocal topology independent of the winding direction of the EP, as well as shielding the topological behavior from the mass disturbances in practical setups, is highly desirable. Our work shows how to beat these limitations and predicts a mass-tolerant unidirectional topological phonon transfer by combining topological operations with the Fizeau light-dragging effect, which splits countercirculating optical modes. Our study paves a new and general route to exploiting profoundly different chiral topological effects, independent of both the EP-encircling direction and the device mass.

III. INNOVATIVENESS, IMPORTANCE AND TIMELINESS OF OUR PROPOSAL

Now, we highlight the innovativeness, importance, and timeliness of our work:

(i) Innovativeness of our results: Our study is the first to shed new light on the pioneering synergy of the *burgeoning* multi-vibration optomechanics, the *emerging* topological operations encircling an EP, and the *leading-edge* light-Fizeau-drag effect. It can pave a quite-general route to exploiting profoundly different nonreciprocal topological effects, being both independent of the EP-encircling direction and immune to the device mass. We believe in the efficacy of our theory of encircling-orientation-independent and mass-free one-way topological physics as based on the synergy of these three hot-research fields. Our study can help to exploit new and general unidirectional topology.

(ii) Importance of our work: We have overcome the long-standing limitations, where the unidirectional TPT is not only dependent on the EP-encirclement direction but also can be easily destroyed in the large-mass regime of the practical setups. This means that we have predicted a fundamentally different topological nonreciprocity independent of the encirclement direction of the adiabatic loops enclosing the EP, and shield the topological behavior from the mass disturbances in practical devices. These results are otherwise unattainable in conventional schemes [S12–S26], where the dependence on the encircling direction of an EP is the essential requirement for all the standard schemes of the unidirectional TPT.

(iii) Timeliness of our study: The previous one-way topological effects [S12–S26] are naturally limited by the dependence on the encirclement direction of an EP in the parameter space, and this leads to a strong *suppression* effect on both topological responses and their nonreciprocities. Specifically, in the previous schemes, switching to the other encircling direction of the EP-enclosing control loop results in no TPT [S12, S13], and the standard topological nonreciprocity relying on the EP-encircling direction is generally suppressed or even fully destroyed in a very wide parameter region [S12, S13]. Here, we overcome these long-standing limitations and suppression effects, and propose a method for an excellent TPT and its nonreciprocity, independent of the EP-encircling direction, by just employing the Fizeau light-dragging effect [S4–S6].

IV. PHYSICAL MECHANISM OF OUR APPROACH

In this section, we elaborate on the physics of how exactly the light induces vibrational modes, and show the underlying physics of our findings.

A. Mechanism of light-induced vibrations

Cavity optomechanical systems enable controlling and inducing the motional mode through the radiation-pressure interaction, and have contributed to the quantum control of engineered mechanical systems ranging from kilogram-scale Laser Interferometer Gravitational-wave Observatory (LIGO) mirrors to nanomechanical systems, enabling the ground-state preparation, entanglement, squeezing of mechanical objects, and position measurements at the standard quantum limit and quantum transduction [S2, S12, S35–S45]. Below, we illustrate in detail on the physical mechanism of how exactly the light induces vibrational modes.

Currently, vibrational modes can be induced or controlled by the radiation-pressure interactions between the cavity-field mode and vibrational modes, and it has been experimentally implemented in both optical [S2, S12, S35–S40] and microwave [S2, S39–S45]:

(i) In the optical domain, vibrational modes can be induced by the light-motion interactions, which has been experimentally implemented using a Fabry-Pérot-type optomechanical configuration, where a silicon-nitride (SiN) membrane (or a movable mirror) is positioned inside a high-finesse Fabry-Pérot optical cavity [S2, S12, S37–S40]. The vibrational eigenmodes of the SiN membrane include near-degenerate pairs that are well-separated in frequency from all the other eigenmodes. The vibration of the SiN membrane (or movable mirror) can tune the resonance frequency of the cavity-field mode; and then, the radiation-pressure interactions (i.e., optomechanical couplings) are induced between the vibrational modes and a common cavity-field mode.

(ii) In the optical domain, it has also been experimentally achieved using a microresonator [whispering-gallery-mode (WGM) resonator], consisting of an optical mode and the breath (vibrational) modes, which are exploited to form an optomechanical system [S2, S35, S36, S39, S40]. Therefore, the light-vibration couplings of an optical mode to the vibrational breath modes are produced by the modulation of the resonant frequency of the cavity field, and this modulation is owing to the vibration of the breath mechanical modes. Specifically, via the geometry effect and the photoelastic effect, the motion of the breath mode of the microresonator changes the optical-mode resonance frequency, which leads to the optomechanical interaction between the breath vibration and the cavity-field mode.

(iii) In the microwave domain, the vibrational modes can be induced by the optomechanical interaction, which has been experimentally realized using electromechanical circuit systems, involving micromechanical drum oscillators and a superconducting on-chip circuit acting as an electromagnetic cavity [S2, S39–S45]. The positions of the micromechanical resonators affect the total capacitance and thus, modulate the resonant frequency of the electromagnetic cavity. This creates the effective radiation-pressure couplings similar to those between the movable mirror/resonator (breath mechanical mode) and an optical mode in an optomechanical system.

B. Underlying physics behind our results

In earlier investigations [S13], the distinct visualization of asymmetric mode transfer concerning the encircling direction of the EP was demonstrated on the Riemann surfaces. In principle, our approach to create a versatile yet unique one-way TPT, independent of the EP encircling direction, can be characterized through the Riemann surfaces. To this end, we have diligently attempted to utilize the Riemann surfaces to elucidate our counterintuitive findings. However, our endeavors have revealed that because of the spinning of our silica microsphere, this approach remains challenging for readers to grasp effectively. Recognizing the importance of ensuring comprehension among a broader audience regarding the physical mechanisms behind our findings, we engaged in extensive and profound discussions with some experts in this field. Consistently, they have highlighted that due to mechanical rotating our microsphere cavity, explaining through the Riemann surfaces posed difficulties and lacked intuitiveness. Consequently, they have advised us unanimously to embrace the Fizeau light-dragging effect [S4] as a more accessible and coherent framework for interpretation. We are committed to ensuring that the underlying physics behind our results are comprehensible to a broader audience. Thus, based on this collective advice, we are inclined to adopt the Fizeau light-dragging effect [S4] for our explanation.

We here need to emphasize that our unparalleled unidirectional TPT occurs because of combining the topological operations with the Fizeau light-dragging effect [S4], splitting countercirculating light modes and leading to the difference of the refractive indices that light experiences. Physically, the light entering from one chosen side of the fibre experiences a Sagnac-Fizeau shift and however, the light entering from the other side leads to an opposite shift. For example, the laser injected from the LHS of the fibre undergoes a Sagnac-Fizeau shift, which engenders the phonon transfer; in stark contrast to this, the light entering from the RHS of the fibre leads to an opposite shift, which yields no transfer of phonons. As a result, this leads to the following advantages:

(i) Introducing light from a selected side of the fiber yields a TPT, whereas doing so from the opposite side does not. This gives rise to a fundamentally distinct topological nonreciprocity, regardless of the direction of the encirclement of the adiabatic loop surrounding the EP, which was unachievable using conventional methods [S12, S13].

(ii) Within a broad parameter range, the nonreciprocity of TPT is significantly *attenuated* by the conventional methods, whereas it is *amplified* by our approach, resulting in an impeccable TPT nonreciprocity.

(iii) In contrast to previous studies [S12–S26], where the topological responses generally degrade or even completely disappear with the increase in either mass or decay of practical setups, our proposal is nearly *immune* to these drawbacks. This immunity is achieved without the necessity of employing high-cost, low-loss materials, or noise filters, albeit at the expense of increased system complexity. Its underlying physics is analogous to the *Doppler effect* extensively demonstrated in various non-topological areas [S27, S28], and this mechanism leads to a complete compensation for the mass-induced and damping-induced detrimental reflections, owing to a drastic enhancement in the intracavity relative photon number.

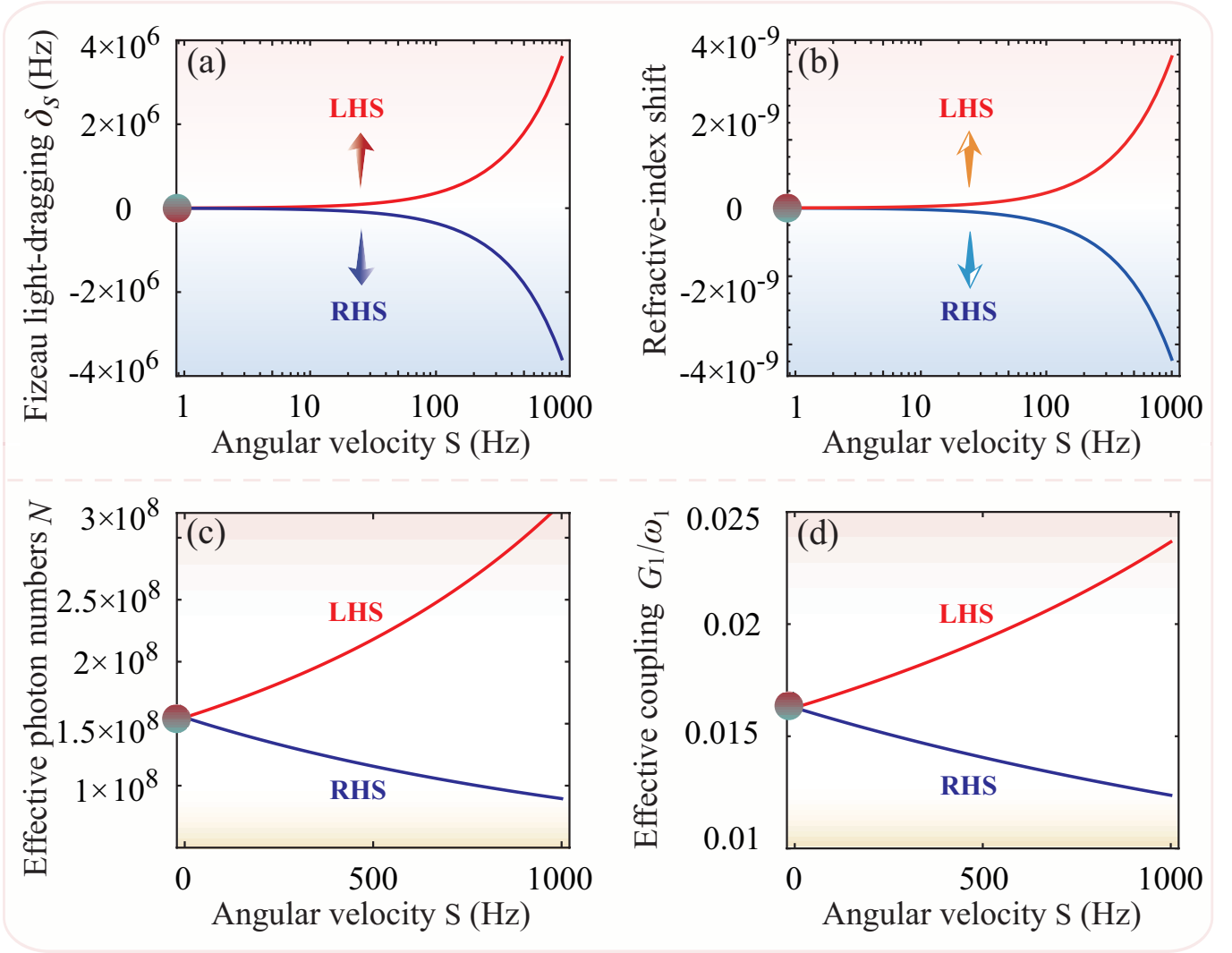


FIG. S11: (a) Fizeau light-dragging δ_s [see Eqs. (S70-S73)] versus the angular velocity S of the silica microsphere for the LHS driving ($\delta_s > 0$, red curves) and the RHS driving ($\delta_s < 0$, blue curves) of the fibre. (b) Changes of the refractive index [see Eq. (S74)] of the material versus S when the spinning microsphere is driven by a laser from the LHS and RHS of the fibre. (c) Effective photon numbers N [see Eq. (S75a)] versus S for the LHS- and RHS-driving cases. (d) Effective light-vibration coupling rate G [see Eq. (S75b)] versus S in both the LHS- and RHS-driving cases. We can see that with the increase of the angular velocity, an opposite frequency shift for the counter-propagating modes happens, and that for the same input laser, owing to this opposite light-frequency shift, the TPT emerges nonreciprocally.

(iv) Notably, an adjustability in the threshold control-loop time required to maintain an excellent TPT is observed, leading to the achievement of a top-velocity-controllable perfect TPT.

(v) In a broader perspective, our study illuminates the connection between topological operations and the Fizeau light-dragging effect, opening up exciting opportunities to uncover novel one-way topological behaviors. These findings are characterized by their independence from the direction of EP encirclement and their immunity against both mass and decay of the practical devices.

In following, we present a comprehensive examination of the physical mechanism underlying our approach, and detailedly exhibit the differences of our scheme compared to previous proposals:

An effective light frequency can experience a Sagnac-Fizeau shift [S4] in our spinning microsphere system. Specifically, owing to the spinning of the silica microsphere with an angular velocity S , the Sagnac-Fizeau shift is experienced by the light, i.e.,

$$\omega_c \rightarrow \omega_c + \delta_s, \quad (\text{S69})$$

where ω_c is the non-spinning (i.e., standard) system and

$$\delta_s = \pm S\Lambda \quad (\text{S70})$$

denotes the Sagnac-Fizeau shift of the driving detuning, with

$$\Lambda = \zeta r \omega_c [1 - 1/\zeta^2 - (\lambda/\zeta)d\zeta/d\lambda]/c, \quad (\text{S71})$$

where the parameters r , ζ , c , and λ are the silica-sphere radius, the refractive index, the speed of light in vacuum, and the wavelength of light, respectively. In fact, the relativistic origin of the Sagnac effect is characterized by the dispersion term (i.e., $d\zeta/d\lambda$), which is small in typical materials (up to $\sim 1\%$). By mechanically rotating the silica microsphere along only in the clockwise direction,

$$\delta_s > 0 \quad (\delta_s < 0) \quad (\text{S72})$$

corresponds to the case, where the driving laser is injected from its left-hand side (LHS) or right-hand side (RHS) of the fibre, leading to an optical mode a_L or a_R , respectively. Therefore, the clockwise (a_R) and anticlockwise (a_L) optical frequencies are, respectively, defined as

$$\omega_c^{R,L} = \omega_c \pm |\delta_s|. \quad (\text{S73})$$

Note that $\delta_s = 0$ (i.e., $S = 0$) denotes the nonspinning (i.e., standard) case, where we obtain $a_{R,L} = a$ and $\omega_c^{R,L} = \omega_c$. This means that when the microsphere cavity does not spin, the Fizeau drag is equal to zero, owing to the same resonance frequency of the light injected from the LHS or RHS of the fibre, and that when increasing the angular velocity S results in an opposing frequency shift for the light, which comes from an opposite orientation.

Specifically, it is shown in Eq. (S73) that with increasing the angular velocity S , the frequency of light is enhanced or suppressed when the silica microsphere is driven from the RHS or LHS of the fibre, respectively. This is due to the fact that the Fizeau light-drag effect caused by the spinning of the microsphere leads to the shift of the light frequency. In order to reveal the underlying physical mechanisms, we plot in Fig. S11(a) the Fizeau light dragging δ_s as a function of the spinning angular velocity S of the silica microsphere when the microsphere is driven by a laser from the LHS ($\delta_s > 0$, red curves) and RHS ($\delta_s < 0$, blue curves) of the fibre. It is shown that with increasing the angular velocity of the spinning microsphere, an opposite frequency shift for the counterpropagating light modes occurs, and that for the same input laser, the TPT appears unidirectionally because of the opposite light-frequency shift for the counterpropagating modes.

To further explore how the Fizeau drag of light causes nonreciprocity fundamentally, the relativistic addition of velocities is taken into account when the periphery of the spinning sphere is moving away/towards from the output/input ports. In light of these considerations, optical paths of counterpropagating light beams are different attributed to the rotation, leading to the irreversible refractive indices for $a_{R,L}$,

$$\zeta_{R,L} = \zeta \left[1 \pm S\zeta r(\zeta^2 - 1)/c \right]. \quad (\text{S74})$$

We find from Eq. (S74) that the refractive index of the material is increased or decreased when light is injected from the RHS or LHS of the fibre, respectively. This is because the Fizeau light-drag effect induced by spinning results in the change of the refractive index of the material. Specifically, in Fig. S11(b), we plot the changes of the refractive index of the material as a function of the angular velocity S , when the laser enters from the LHS and RHS of the fibre. We observe that the change of the refractive index of the material is induced by the Fizeau light-dragging effect resulted from spinning the silica microsphere.

In addition, the Fizeau drag of light can lead to a significant amplification in both intracavity relative photon numbers and effective light-motion couplings. In view of elucidating and verifying the underlying physical mechanism behind these counterintuitive phenomena, the effective mean photon numbers $N_{R,L}$ and the effective light-motion couplings $G_j^{R,L}$ are, respectively, defined by:

$$N_{R,L} = \frac{P_{\kappa_{\text{in}}}/(\omega_j \hbar)}{(\Delta_{\text{eff}}^{R,L})^2 + (\kappa/2)^2}, \quad (\text{S75a})$$

$$G_j^{R,L} = g_j \sqrt{\frac{N_{R,L}}{\rho_j}}. \quad (\text{S75b})$$

where

$$\Delta_{\text{eff}}^{R,L} = \Delta \mp |\delta_s|. \quad (\text{S76})$$

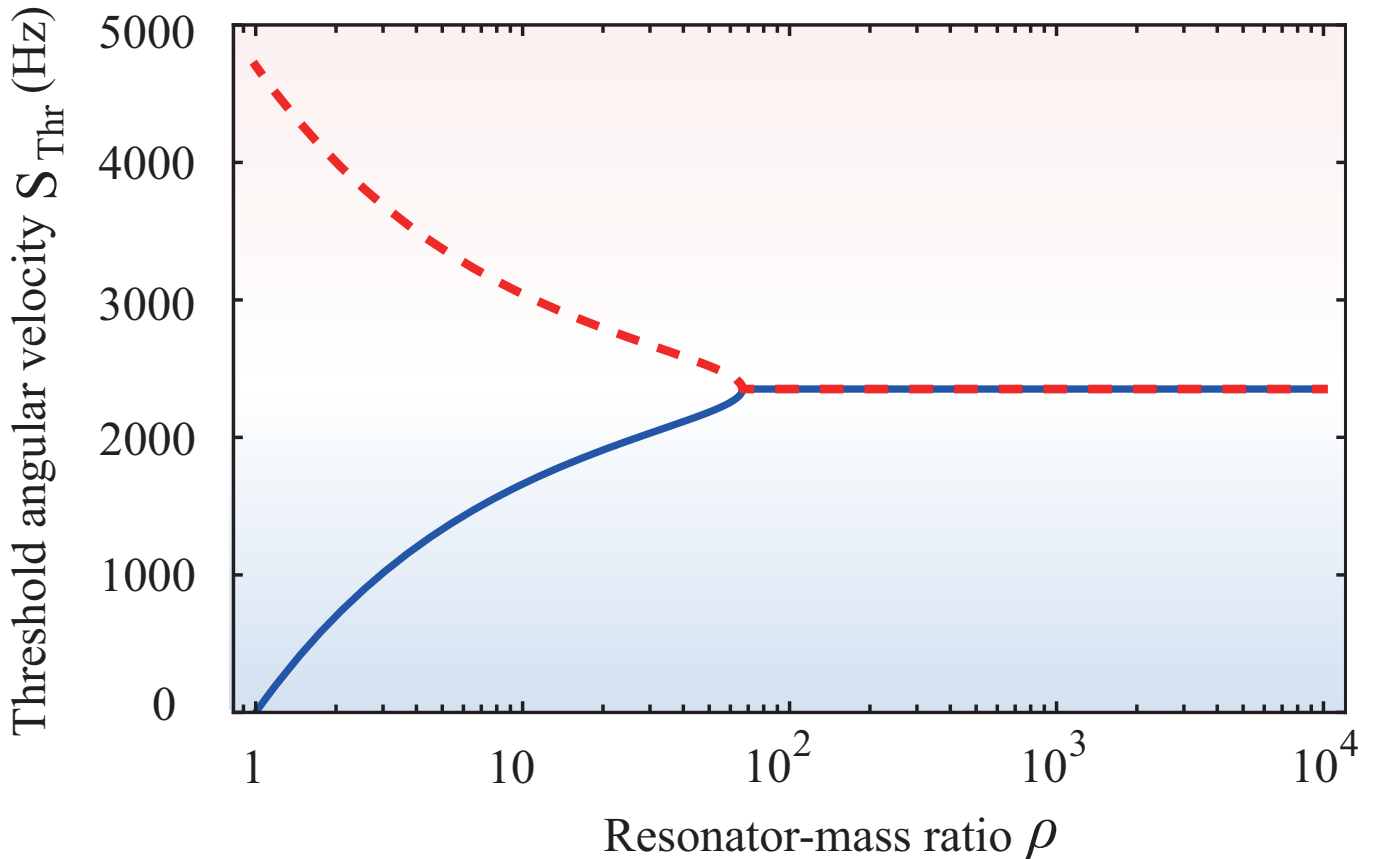


FIG. S12: Threshold angular velocity S_{Thr} [see Eq. (S77)] of the spinning silica microsphere versus the resonator-mass ratio ρ . It shows that a mass-tolerant unidirectional TPT can be achieved by combining topological operations with the Fizeau light-dragging effect splitting countercirculating optical modes. Note that through analytical analysis of Eqs. (S75), (S76), and (S77), we have discovered that theoretically, there is no anomaly region because, at this point, we have not taken into account the experimental anomalies on “Self-adjustment” effect present in actual experiments. However, if we consider the actual experimental conditions, the anomalous region still emerges.

It is obviously shown in Eqs. (S75) and (S76) that increasing either the mass ratio ρ_j or the optical decay rate κ of the practical devices leads to the suppression of the effective light-vibration coupling rates $G_j^{R,L}$; while by using a spinning device, both mass- and damping-induced detrimental disturbances can be fully neutralized. Specifically, increasing optical dissipation κ reduces the effective light-motion coupling strength $G_j^{R,L}$, with the underlying physics being the reduction in the effective photon numbers $N_{R,L}$ inside the cavity due to the increased optical dissipation. Similarly, the increase of the mass ratio ρ_j also decreases the effective optomechanical coupling strength $G_j^{R,L}$, because larger oscillator masses are less prone to resonances. Furthermore, we clearly see from Eqs. (S75) and (S76) that by enhancing the Fizeau light-dragging effect, the effective mean photon numbers $N_{R,L}$ can be significantly decreased (increased), which leads to a diminishment (an enhancement) of the effective light-motion couplings $G_j^{R,L}$, when the system is driven by a laser injected from the RHS (LHS). Physically, applying the Fizeau drag effect to topological operations can result in a significant improvement in the effective mean photon numbers of the cavity, and it corresponds to a giant amplification in the effective light-vibration interactions. To further demonstrate this point, we plot in Figs. S11(c) and S11(d) the effective photon numbers and the effective light-motion couplings versus the angular velocity S when the light is injected from the LHS or RHS of the fibre, respectively. Figures S11(c) and S11(d) show that in the LHS- and RHS-driving cases, the effective photon numbers in the cavity can be significantly increased (decreased) with increasing the angular velocity S of the spinning silica microsphere. Our main concept is akin to the Doppler effect, extensively showcased across various nontopological domains [S27, S28], and this mechanism results in a significant augmentation of the intracavity relative photon number. These results mean that the application of the Fizeau light-dragging effect to the topological operations establishes not only a giant enhancement in the phononic isolation, but also offers the possibility of immunizing the topological behavior against detrimental disturbances from both mass and decay in practical devices. These findings are entirely matched with the analytical results shown in Eqs. (S75) and (S76).

In particular, to achieve an optimal topological energy transfer through the Fizeau drag of light, we derived analytical expressions that establish the relationship between the threshold angular velocity S_{Thr} of the silica microsphere and the resonator-





	Standard methods		Our approach	
EP-encircling orientation				
Phonon transfer	Yes	<i>No</i>	Yes	<i>Yes</i>
Nonreciprocity	No	No	<i>Yes</i>	<i>Yes</i>
	<i>Suppressed region</i>		<i>Enhanced region</i>	
Mechanism	Topological operations		Topological operations + Fizeau light-dragging effect	
EP-encircling-direction dependence	<i>Dependent</i>		<i>Independent</i>	
Dependence on mass	<i>Dependent</i>		<i>Independent</i>	
Dependence on optical/mechanical decay	<i>Dependent</i>		<i>Independent</i>	

TABLE II: Correspondence of the EP-encircling orientations (row 2), the ability of topological phonon transfer (row 3), the nonreciprocity (row 4), the underlying physical mechanism (row 5), the EP-encircling-direction dependence (row 6), and the mass dependence (row 7), for the standard method (row 1 and column 2) and our approach (row 1 and column 3). Rows 2, 3, and 6 are evident that in the standard (i.e., non-spinning) method, the TPT inherently relies on the EP-encircling orientation. However, in our approach (i.e., the spinning case), this constraint is overcome, signifying its independence of the encircling directions of the EP. These findings suggest that the TPT is consistently achievable regardless of the EP-encircling directions, opening avenues for exploring new related topologies. Row 4 reveals that in the previous representations, achieving TPT nonreciprocity is attainable in neither the counterclockwise nor clockwise direction, and that in contrast, our approach can make it feasible in both directions. Furthermore, our observations highlight that within a significantly broad parameter range, the TPT nonreciprocity is *suppressed* with the standard method, whereas it is *enhanced* through the adoption of our proposed approach, resulting in a notable improvement in the TPT nonreciprocity. Row 5 shows that in the previous representations, the unconventional one-way TPT arises through the imposition of topological operations encircling an EP, and that in contrast to the prior depictions, our study marks the first instance of shedding new light on the groundbreaking synergy between the *emerging* topological operations encircling an EP and the *cutting-edge* light-Fizeau-drag effect. Rows 7 and 8 reveal that in the standard schemes, the TPT is inherently susceptible to disruption with an increase in either resonator mass or decay rate; while our method exhibits immunity against both mass and decay of the practical device, ensuring the preservation of TPT.

mass ratio ρ :

$$S_{\text{Thr}} = \left[-\Delta \pm \sqrt{[4\Delta^2 - (\rho - 1)\kappa^2]/(4\rho)} \right] / \Lambda. \quad (\text{S77})$$

It shows that keeping an optimal topological phonon transfer for a larger value of the resonator mass ratio ρ requires a higher angular velocity S of the silica microsphere, as shown in Fig. S12. Through analytical analysis of Eqs. (S75), (S76), and (S77), we have found that theoretically there is no anomalous range. This is because, at this stage, we have not taken into account the experimental anomalies on ‘‘Self-adjustment’’ effect that exists in actual experiments. However, if we consider the actual experimental conditions, anomalous ranges will emerge. Specifically, we find that for the standard (i.e., non-spinning) scheme,

the optomechanical-coupling strengths decrease with increasing either the mass or the damping rate of the practical devices; while for a spinning quantum device, it is significantly enhanced or even amplified, compared with that in the nonspinning case. This counterintuitive phenomenon can be understood via an enhancement in the effective photon numbers in the cavity. We show in detail that in the non-rotating case, the effective optomechanical-coupling strengths become smaller with the increase of either the mass or the decay rate. In stark contrast to this, for the spinning case, a multiple-order-of-magnitude amplification in the photon numbers arises from the Sagnac effect, without which it vanishes. These results indicate that both mass- and decay-induced reflections can be significantly suppressed in a spinning device and, as a result, one can achieve nearly an ideal topological transfer of phonons.

Now, we show the differences of our method compared to previous representations. We first highlight that the EP-encircling-direction-independent outcomes using our approach are unattainable in conventional schemes, as the dependence on the encircling direction of the EP is an essential requirement for all standard unidirectional TPT occurrences. We also emphasize that the nonreciprocity of TPT is *diminished* in the standard method, whereas it is *amplified* through our proposed approach. In a broader view, our study sheds new light on the synergy of the topological operations and the Fizeau light-dragging effect, and lays the foundation for a broadly applicable approach to harnessing profoundly different topological nonreciprocity, which is characterized by its independence of EP-encircling directions and by its immunity to both mass and damping of practical devices.

Specifically, to understand this more intuitively, we show in Table II the correspondence of the EP-encircling orientations (see row 2), the ability of TPT (row 3), the nonreciprocity (row 4), the underlying physical mechanism (row 5), the EP-encircling-direction dependence (row 6), and the mass dependence (row 7), when the system operates in the standard method ($S = 0$, row 1 and column 2) and our approach ($S = 400$, row 1 and column 3). Now, we delve into the following four aspects in detail:

(i) We show in Table II that in the non-spinning case, the TPT naturally depends on the EP-encircling directions; while in our spinning approach, it breaks this limitation, i.e., it is independent of the encircling directions of the EP, as shown in Table II. These findings indicate that the TPT can always occur no matter which direction the encircling takes, which paves a route to exploring new topology independent of the EP-encircling directions. Specifically, in the standard method, the TPT can be achieved only in the counterclockwise direction of encircling the EP but not in the clockwise direction. In stark contrast to this, by introducing the Sagnac-Fizeau effect, the phonon transfer can always happen in both counterclockwise and clockwise directions. This means that by using our method, the phonon transfer can always occur no matter whatever the direction of winding around the EP is applied.

(ii) We reveal in Table II that in the previous representations, the TPT nonreciprocity is unachievable in either counterclockwise or clockwise direction; while in our spinning approach, it becomes feasible in both directions. Moreover, we find from Table II that in a very wide parameter region, the TPT nonreciprocity is *suppressed* with the standard method but *enhanced* using our proposal, yielding a perfect TPT nonreciprocity. Specifically, the previous one-way topological behaviors [S12–S26] are naturally limited by the strict dependence on the encirclement direction of the EP in the parameter space, and this leads to a strong *suppression* effect on both topological responses and their nonreciprocities. For the previous schemes, switching to the other encircling direction of the EP-enclosing control loop results in no TPT [S12, S13]; thus the standard topological nonreciprocity relying on the EP-encircling direction is generally suppressed or even fully destroyed in a very wide parameter region [S12, S13]. Here, we break these long-standing limitations and suppression effects, and build an excellent TPT and its nonreciprocity, independent of the EP-encircling directions, by just employing the Fizeau light-dragging effect [S4–S6].

(iii) Physically, we show in Table II that in the previous representations, the unconventional one-way TPT is induced by imposing topological operations encircling an EP. Compared to previous representations, our study is the first to shed new light on the pioneering synergy of the *emerging* topological operations encircling an EP and the *leading-edge* light-Fizeau-drag effect. It can pave a quite-general route to exploiting profoundly different nonreciprocal topological effects, with both independence of the EP-encircling directions and the immunity against the device mass. We believe that there is a need of guiding theory toward encircling-orientation-independent and mass/decay-free one-way topological physics using our proposed pioneering synergy of these three hot-research fields, and here it comes. Our study can help to exploit a new and general unidirectional topology.

(iv) We demonstrate in Table II that in the standard schemes, the TPT inherently can be easily destroyed with increasing the resonator mass; while in our method, it is immune to the mass of the practical device. Note that by utilizing our method, we fully overcome the long-standing limitations maintaining in the previous schemes, where the unidirectional TPT is not only strictly dependent on the EP-encirclement direction, but also can be easily destroyed in the large-mass regime of the practical setups. By employing our method, we induce a fundamentally different topological nonreciprocity independent of the encirclement direction of the adiabatic loops enclosing the EP, and shield the topological behavior from the mass disturbances in practical devices. These results are otherwise unattainable in conventional schemes [S12–S26], where the dependence on the encircling direction of the EP is the essential requirements for all the standard unidirectional TPT. Our study paves a quite-general route to exploiting profoundly different topological chirality, both independent of the EP-encircling direction and immune to the masses and decays of practical devices.

V. DETAILED DISCUSSIONS ON EXPERIMENTAL FEASIBILITY USING REALISTIC STATE-OF-THE-ART EXPERIMENTS

In this section, we detailedly show some discussions on (i) the experimental feasibility using realistic state-of-the-art experimental conditions, (ii) detailed derivation of the “self-adjustment” effect, and (iii) detailed analysis of the microscopic-level forces

A. Experimental feasibility analysis using realistic state-of-the-art experimental conditions

Although what we have proposed a purely theoretical scheme, our approach is completely experimentally feasible, based on the state-of-the-art experimental conditions (see Table III, Figs. S13 and S14).

Here, we have engaged in in-depth discussions on the feasibility analysis of experiments, and we believe that our proposed theoretical scheme is entirely feasible for experimentations under the realistic given state-of-the-art experimental conditions. In order to further demonstrate this point, we have extensively enlarged the discussions on possible experimental implementations of the physical effects that we have predicted using the realistic given state-of-the-art experimental systems. Specifically, we have presented detailed analyses on both the simulation parameters and experimental parameters, based on the proposed state-of-the-art experiments, as shown in Table. III. Our analyses indicate that the present scheme is fully experimentally accessible under current experimental conditions, and that the proposed phenomena are relevant for the state-of-the-art experiments based on multi-mode cavity optomechanics, as shown in Figs. S13 and S14. We believe that our proposed TPT scheme, being independent the EP-encircling orientations, is clear and experimentally achievable using the present realistic given state-of-the-art experimental conditions.

In addition, we have extensively enlarged the discussions on the experimental feasibility of the physical effects that we have predicted, based on the realistic state-of-the-art experimental parameters [S4, S12]. By adding experimental analyses and numerical estimations with experimental accessible parameters, the relevance of our proposed phenomena, under the realistic state-of-the-art experimental conditions, can be confirmed. In addition, an excellent agreement between the proposed and simulated results indicates that the proposed phenomena are relevant for the realistic state-of-the-art experiments. Specifically, we have added detailed analyses of experimental realizations, based on the realistic state-of-the-art experimental components consisting of: (i) the two-vibration optomechanical platform of Ref. [S12] and (ii) the spinning optical cavity of Ref. [S4].

Actually, the proposed physical model is general and hence, in principle, our scheme can be realized in standard optomechanical systems. To implement the nonreciprocal TPT independent of both EP-encircling direction and device mass, two elements are needed: (i) the in-parallel light-motion couplings of the two vibrations to a common optical cavity, and (ii) the tunable spinning of the optical cavity. Therefore, these two kinds of elements should be implementable in our candidate experimental systems. It should be pointed out that, though until now the two kinds of elements have been realized in separate experiments, the implementation of them in the same experimental setup has not been reported. Nevertheless, the two kinds of interactions can be implemented in our system, under the current realistic state-of-the-art experimental conditions. Note that experimental capabilities in this field have improved enormously over the past decade and will surely continue to improve in the next decade, enabling a vastly improved experimental feasibility.

(i) Currently, the in-parallel optomechanical couplings between multiple vibrational modes and a common optical mode have been experimentally implemented using either optical [S2, S12, S35–S40] or microwave [S2, S39–S45] domains:

(1) In the optical domain, the in-parallel light-motion interactions have been experimentally achieved using microresonators or whispering-gallery-mode (WGM) resonators consisting of an optical mode and two vibrational modes, which are exploited to form a multi-mode optomechanical system. Therefore, the in-parallel light-vibration couplings of an optical mode to the two vibrational modes are produced by the modulation of the resonance frequency of the cavity field, and this modulation is owing to the vibration of the mechanical breath modes [S2, S35, S36, S39, S40]. We here need to emphasize that using the ultrahigh- Q crystalline microresonators, more than 20 mechanical modes with the vibrational frequencies ranging from approximately 500 kHz to 2 MHz were experimentally observed [S2, S35, S39, S40].

(2) In the optical domain, the in-parallel optomechanical couplings have also been experimentally implemented using multi-vibrational-mode optomechanical configurations, consisting of a high-finesse optical mode and the multi-motion modes [S2, S12, S37, S39, S40]. Physically, the vibration of the mechanical resonators can tune the resonance frequency of the cavity-field mode; and then, the in-parallel radiation-pressure couplings are simultaneously induced between these vibrational modes and a common optical mode.

(3) In addition, an alternative approach to the mechanical resonators is to exploit near-field effects close to the surface of optical microresonators, where the optical field allows dispersive coupling to other mechanical structures. In essence, the mechanical motions modulate the distance between the interfaces. Because of the near-field character, the optomechanical coupling strengths scale exponentially with the distance, and hence it allows one to generate large values for optomechanical coupling strengths [S1, S46–S50]. This has been used to demonstrate the optomechanical coupling between a toroidal microcavity and the

Symbol	Physical quantity	Experimental parameters of Nature 537, 80 (2016); 558, 569 (2018) [S4, S12]	Our simulation parameters	Experimental feasibility
c	Vacuum light speed	3×10^8 m/s	3×10^8 m/s	Yes
λ	Laser wavelength	1064 nm	1064 nm	Yes
$\kappa/2\pi$	Total dissipation rate	177 kHz	177 kHz	Yes
$\kappa_{\text{in}}/2\pi$	Input coupling rate	70 kHz	70 kHz	Yes
P	Laser power	2 uW to 750 uW	2 uW to 750 uW	Yes
$g_{1(2)}/2\pi$	Single-photon coupling rate	1.03 (1.14) Hz	1.03 (1.14) Hz	Yes
Δ	Driving detuning	-1200 kHz to -400 kHz	-1800 kHz to 0 kHz	Yes
T	Bath temperature	300 mK	300 mK	Yes
$Q_{1(2)}$	Phononic quality factors	$1.3(0.56) \times 10^6$	$1.3(0.56) \times 10^6$	Yes
Q_c	Optical quality factor	1.6×10^9	1.6×10^9	Yes
$\omega_{1(2)}/2\pi$	Mechanical frequencies	788.024 (788.487) kHz	788.024 (788.487) kHz [S36]	Yes
$\gamma_{1(2)}/2\pi$	Mechanical linewidths	0.6 (1.4) Hz	0.6 (1.4) Hz	Yes
$m_{0(j=1,2)}$	Effective masses	10 ng	100 ng	Yes
$\epsilon_{0(j=1,2)}$	Dielectric constants of air (taper, silica sphere)	1 (3.9)	1 (3.9)	Yes
$\zeta_{0(j=1,2)}$	Refractive indexes of air (taper, silica sphere)	1 (1.48)	1 (1.48)	Yes
$r(r_0)$	Sphere (fiber) radii	1.1 mm (544 nm)	1.1 mm (544 nm)	Yes
S	Spinning angular velocity	0 to 10 kHz	0 to 10 kHz	Yes
E	Young modulus of silica	75 GPa	75 GPa	Yes
Υ	Elastic limit of silica	9 GPa	9 GPa	Yes

TABLE III: Parameters of the two-vibrational-mode optomechanical devices reported in the literature [S12], the spinning-cavity setup reported in the literature [S4], and used in our simulations. The columns 1 and 2 present the notation and physical meaning of the used parameters, respectively. The parameters in columns 3 and 4 are, respectively, used in the experimental works [S4, S12] and our numerical simulations. The column 5 shows a full experimental feasibility between the realistic parameters reported in the experiments and the parameters used in our numerical simulations, indicating that the proposed phenomena are relevant for the current state-of-the-art experiments. Note that in ultrahigh- Q crystalline microresonators [S2, S35, S39, S40], more than 20 vibrational modes were experimentally observed, exhibiting mechanical resonance frequencies ranging from approximately 500 kHz to 2 MHz.

nearby SiN nanomechanical resonators [S1, S3]. Another related possibility is to couple two mechanically vibrating microdisk resonators [S46–S48] or two photonic crystal cavities [S49, S50] via their optical near field.

(4) In the microwave domain, the in-parallel optomechanical interaction can be experimentally realized using electromechanical circuit systems, which involve multiple micromechanical drum oscillators and a superconducting on-chip circuit acting as an electromagnetic cavity [S41–S45]. The positions of the mechanical resonators affect the total capacitance

Using realistic state-of-the-art *experimental* parameters

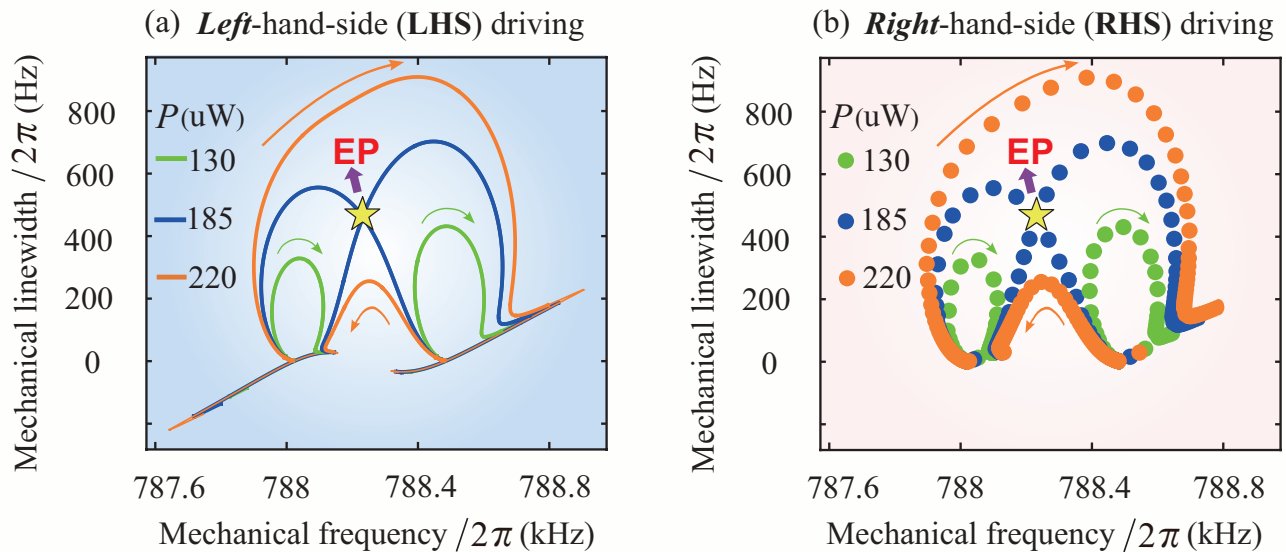


FIG. S13: Complex eigenvalues of the two motional modes. Vibrational decay rate (mechanical linewidth) and the vibrational resonance frequency of the two motional modes as functions of the driving detuning Δ and the driving laser power P , when the system is driven by a laser from the left-hand side (LHS) or right-hand side (RHS) of the fibre, for the angular velocity $S = 400$ Hz of the spinning silica microsphere. The green, blue, and orange curves (disks) denote the complex eigenvalues for $P = 130$ uW, 185 uW, and 220 uW, respectively. That is for the spinning case, we consider the situations where the rotating silica sphere is driven from the LHS or RHS of the fibre. Here the complex eigenvalues of the quantum system are varied with the driving detuning $\Delta \in [-1800 \text{ kHz}, 0 \text{ kHz}]$. Note that for lower values of the laser power P , each eigenvalue follows a closed trajectory, which ends and begins at the same point. In stark contrast to the case of the low powers, for higher values of the driving power P , the eigenvalues follow open trajectories, each of which ends at the starting point of the other. By tuning the laser power P and the driving detuning Δ , the EP which is described by the yellow star occurs. Our analyses indicate that the present scheme is experimentally accessible under current experimental conditions, and that the proposed phenomena are relevant for the state-of-the-art experiments.

and thus, modulate the resonance frequency of the cavity. This creates effective in-parallel optomechanical interactions similar to those between multiple movable mirrors and a common optical mode in an optomechanical cavity.

(ii) Recently, the tunable mechanical spinning of an optical cavity has been experimentally implemented using a spinning silica-microsphere cavity, which was positioned close to a tapered region of a single-mode telecommunication fibre. The evanescent coupling of the light into this spinning setup is caused by the tapered region of the fibre, and via the same coupler, the light can be coupled out through the other side of the fibre [S4]. Consequently, both input and output ports can be simultaneously served by each side of the fibre, and relying on the input port, the light circulates in the silica sphere in either clockwise or counter-clockwise direction, resulting in an optical mode a_R or a_L (with resonance frequencies $\omega_c^{R,L}$), respectively. Experimentally, the aerodynamic process plays a vital role in fiber-resonator interactions in a rotating setup, which drags air into the region between the sphere and tapered fiber, yielding an air-lubrication layer in this region. The thin air film then enables the fiber to fly at a few nanometres above the sphere. Owing to the “self-adjustment” process, the taper floats back to its initial position, once it is caused to rise higher than the stable-equilibrium height by any perturbation. The critical coupling of light into the silica sphere is enabled via the “self-adjustment” behavior, whereby an optical drag, identical in size but opposite in sign, is experienced by the countercirculating light.

In the above, we have added the detailed discussions on the experimental implementation of our physical model based on the realistic state-of-the-art experimental conditions. To provide further supporting experimental arguments demonstrating the feasibility of the main conclusions and potential applications, we now present detailed analyses on both experimental and simulation parameters based on the proposed state-of-the-art experimental systems, and especially, we also added Table III to compare the parameters used and the parameters reported. We see from Tab. III that the parameters used and those reported show the experimental feasibility, and the numerical data indicates that the proposed phenomena are relevant for state-of-the-art experiments.

(i) Specifically, by employing realistic state-of-the-art experimental parameters (see Tab. III), we show in Fig. S13 that the complex eigenvalues of the two vibrational normal modes. This demonstrates that our present scheme is experimentally

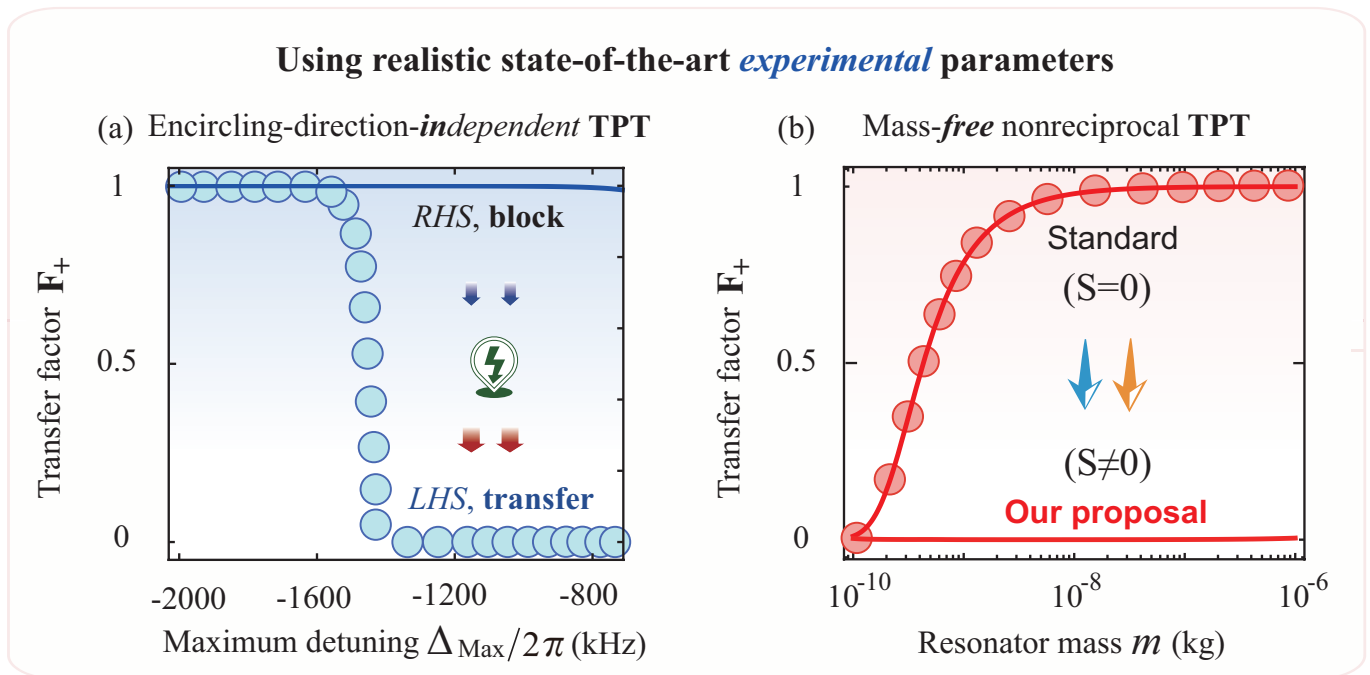


FIG. S14: By using realistic state-of-the-art experimental parameters, we show (a) the encircling-direction-independent unidirectional TPT and (b) the mass-free nonreciprocal TPT. (a) Topological energy-transfer quality factor F_+ versus the maximal driving detuning Δ_{Max} , when the light enters from the LHS (blue symbols) or RHS (blue curves) of the fiber, for the angular velocity $S = 400$ Hz of the spinning silica microsphere. We see that by using realistic state-of-the-art experimental parameters, the TPT occurs when the silica sphere is driven in one chosen side but not in the other, and this leads to a unique topological energy-transfer nonreciprocity, without depending on the direction of winding around the EP. (b) TPT quality factor F_+ versus the mass m of the mechanical resonator for both standard ($S = 0$) and our approaches ($S = 3$ kHz), in the LHS-driving case. By adding experimental analyses and numerical estimations with experimental accessible parameters, the relevance of our proposed phenomena under the state-of-the-art or near-future experimental conditions can be confirmed.

accessible under current state-of-the-art experimental conditions, and that our main conclusions and potential applications are relevant for the state-of-the-art experiments.

(ii) Based on these state-of-the-art experimental parameters shown in Tab. III, Fig. S14 exhibits in detail how to achieve the one-way TPT independent of the encircling orientation of the EP. Our simulations using experimental parameters of Refs. [S4, S12] demonstrate that our main conclusions and potential applications of the predicted effect are relevant for the state-of-the-art experiments.

(iii) By utilizing these state-of-the-art experimental parameters (see Tab. III), we show in Fig. S14(b) that our approach paves a feasible route to protecting or even immunizing topological resources against the mass disturbances in practical setups, and enables the construction of mass-free phononic devices. By adding experimental analyses and numerical estimations with experimental accessible parameters, the relevance of our proposed phenomena under the state-of-the-art or near-future experimental conditions can be confirmed.

In a summary, by adding these detailed parameter analyses and numerical estimations, we have demonstrated that our proposed scheme, main results, and potential applications are experimentally accessible under the realistic state-of-the-art experimental conditions. Through these efforts, we believe that our work is now more experimentally grounded.

B. Detailed analysis of the “self-adjustment” effect

Based on the experimental work [S4], a silica microsphere, mounted on a turbine and spins along its axis with an experimentally feasible value of an angular velocity, is considered. In practical experiments, by utilizing levitated nanomechanical rotors [S51, S52], a faster or slower spinning device has been demonstrated. Subsequently, the driving laser is coupled into/out of the silica sphere evanescently, when a single-mode telecommunication fiber is positioned near this rotating silica sphere.

The aerodynamic process in this rotating silica sphere plays a crucial part in the stable fiber-vibration interacting. Concretely, the air can be dragged into the region between the vibration and the tapered fiber by fast rotating silica microsphere and therefore, it produces an air lubrication layer in this region. Whereafter, the fiber can be made to fly above the silica sphere with the

separation of a few nanometres, by the thin film of air, which applies the pressure on the surface of the tapered fiber facing the silica sphere. Consequently, the taper can be caused by any perturbation to rise higher than the stable-equilibrium height float back to its original position, on condition that the taper is caused to rise higher than the stable-equilibrium height by any perturbation, and this floats back to its initial position, called as “self-adjustment process”. The fiber, therefore, does not stick or touch to the silica sphere, even though it is pushed towards the rotating setup [S4]. To further clearly demonstrate this point, the air pressure can be written as

$$\Delta T_{\text{air}} = (\rho \Delta \theta) T_{\text{air}} / L, \quad (\text{S78})$$

where the parameters θ and ρ are, respectively, the angle and radius of the winding shape in the deformation region. We then obtain an analytical expression of the total air pressure T_{air} on the taper as:

$$T_{\text{air}} = 6.19 \mu r^{5/2} \mathbf{S} \int_0^{r_0} \left(h - \sqrt{r_0^2 - x^2} + r_0 \right)^{-3/2} dx, \quad (\text{S79})$$

in which the parameters r_0 and r are, respectively, the radiuses of the taper and silica sphere. In addition, the parameters $h = h_0 + d$ and μ , respectively, denote the taper-resonator separation and the air viscosity, with the parameter h_0 representing the stationary gap between the silica sphere and the fiber. Then, a tension on the infinitesimal cylinder of the fiber is resulted from the local deformation and, therefore, it is derived as:

$$\Delta T_{\text{ela}} = 2\mathcal{F} \sin(\Delta\theta/2) \approx \mathcal{F} \Delta\theta, \quad (\text{S80})$$

in which the parameter \mathcal{F} denotes the elastic force applied on the taper, and it satisfies $\sigma = \mathcal{F}/(\pi r_0^2) = \epsilon E$, with the used parameters E depicting the Young modulus of the silica, σ being the uniaxial stress, $\delta_L = L' - L$ representing the variation of the original length L of the deformation region, and $\epsilon = \delta_L/L$ denoting the strain. In addition, we can straightforwardly derive the analytical expression of the parameter δ_L based on the following analytical relations:

$$(L/2)^2 + (\rho - d)^2 = \rho^2, \quad L' = \rho\theta, \quad \sin(\theta/2) = L/(2\rho). \quad (\text{S81})$$

Therefore, the parameter T_{air} in the case of equilibrium, i.e.,

$$\Delta T_{\text{air}} = \Delta T_{\text{ela}} \quad (\text{S82})$$

can be obtained with another form:

$$T_{\text{air}} = 2\pi r_0^2 E [\arcsin(\phi) - \phi] \approx \pi r_0^2 \phi^3 E / 3, \quad (\text{S83})$$

where the parameter ϕ can be defined as:

$$\phi = 4Ld / (L^2 + 4d^2). \quad (\text{S84})$$

Thus, the elastic force (i.e., the strain), positively associated with the taper-resonator separation, is shown as:

$$\frac{\partial \mathcal{F}}{\partial h} = \pi r_0^2 E \frac{\partial \epsilon}{\partial d} = 16\pi r_0^2 E L^2 d (L^2 - 4d^2) / [3(L^2 + 4d^2)^3] > 0, \quad (\text{S85})$$

where the reduced the strain of the taper $\epsilon = \arcsin(\phi)/\phi - 1 \approx \phi^2/6$, and the analytical expression of the displacement $d = L(\beta - \sqrt{\beta^2 - 1})/2$, with the parameter β being $\beta = [\pi r_0^2 E / (3T_{\text{air}})]^{1/3}$. Considering the limit of the parameter $|\phi| \ll 1$, we can safely make an approximation, $\arcsin(\phi) = \phi + \phi^3/6 + \dots$, physically indicating that we require a comparatively small distortion.

We can clearly see from Eq. (S85) that when the stable-equilibrium distance is much smaller than the air gap, a much stronger strength of the elastic force can be achieved and as a result, we can largely suppress the air pressure acted on the taper. Therefore, a self-adjustment behavior emerges, because the taper is dragged back to its initial position once any perturbation induces it away from the spinning device. the critical coupling of light into or out of the resonator can be enabled by the self-adjustment of the tapered fiber and then, using this mechanism, the counter-propagating light experiences an optical drag identical in size, but opposite in sign.

Concerning a practical experiment, we consider the case where the spinning silica sphere is not touching the taper, even though the rotating device is pushed towards the taper. Here we show the exhibitions that the rotating sphere is veered away from the taper as it is pushed towards the taper. For practical experiments, we assume that there is no wear of both silica sphere and taper, even after undergoing a long period of operation, and that the taper is not been stucked to the spinning silica sphere, even when the rotating configuration is pushed towards the taper. By contrast to this, the taper does stick to a stationary silica sphere via

van der Waals forces, in a control experiment where the silica sphere is non-spinning, and this taper requires to be pulled back to break the connection. Then the micrometre-scale craters on the surfaces of the silica sphere and the taper are observed under a microscope. This indicates that no any adhesion or abrasion occurs in the spinning-resonator case.

It should be pointed out that fluid air-film lubrication [S53] between surfaces offers a feasible way for realizing a desired motion of a machine element with no wear and minimal friction. Such bearings have been revealed to be enough robust, based on the fact that they have been studied for almost a century. In more detail, it has been demonstrated that the gas-film and liquid-film lubrications [S54] have been used for the sand-proof bearings in marine vessels dating back to 1932 [S55], and especially, these lubrications [S54] have enabled flying heights of less than 10 nm in recently, demonstrated helium-filled hard drives.

Note that though it is generally stable for such fliers, the effects (e.g., lubricant compressibility and intermolecular forces) should be considered by modelling these fliers. Employing the boundary conditions of a foil wrapping a rotating cylinder can easily solve the Reynolds equation [S56]. That means that we can use similar methods, but with some modifications [S53], to derive the analytical expression on the gap between the foil and the surface of the spinning cylinder:

$$h = 0.643r^{5/3}(6\mu\mathbf{S}/t')^{2/3}, \quad (\text{S86})$$

where \mathbf{S} and r are, respectively, the angular velocity and the radius of the cylinder, t' is the tension of the foil per unit width, and μ is the viscosity of the fluid. In our case, the curvature of the sphere along the polar direction is so small compared with the width of the film-lubricated region of interest that it thins by only 1 Å by the end of this region. For this reason, we can estimate our rotating sphere using equation (S86), even though it was originally developed for a rotating cylinder. Because Eq. (S86) deals with flat foil, whereas our flyer is a wire, we break the circular cross-section of our wire into a set of infinitesimal flat stairs. We integrate the tension over these stairs to obtain the total tension T as a function of the minimum taper–sphere separation h .

In addition, we find that there exists a sharp variation around $S \approx 1600$ Hz, corresponding to an anomalous region of the “self-adjustment” process. Physically, in this anomalous region, the critical evanescent coupling of the spinning microsphere to a single-mode-telecommunication tapered fiber is dramatically disturbed by the radial breathing of the resonator, because the effect of the mechanical displacement is non-negligible. To demonstrate this point, we here consider the influence of the radial breathing of the resonator on the stable fiber-resonator coupling. Specifically, we detailedly compare the mean mechanical displacement x_s with the air-induced displacement d , i.e.,

$$\eta = x_s/d = q_s x_{zp}/d, \quad (\text{S87})$$

where $x_{zp} = \sqrt{\hbar/(m\omega_m)}$ denotes the standard deviation of the zero-point motion of the mechanical mode. We see from Eq. (S87) that:

(i) if the effect of the mechanical displacement is negligible (i.e., $\eta \rightarrow 0$, $x_s \ll d$), the radial breathing of the resonator does not disturb the critical evanescent coupling;

(ii) if the effect of the mechanical displacement is non-negligible (i.e., $\eta \rightarrow 1$, $x_s \rightarrow d$), the critical evanescent coupling of the spinning microsphere to a single-mode-telecommunication tapered fiber is dramatically disturbed by the radial breathing of the resonator, which indicates the breaking of the “self-adjustment” effect.

Note that the “self-adjustment” behavior describes that the taper can be dragged back to its original position when any perturbation causes it away from the spinning resonator. The “self-adjustment” of the tapered fiber enables the critical coupling of light into or out of the resonator, by which the counter-propagating beams can experience an optical drag identical in size, but opposite in sign.

C. Detailed analysis of the microscopic-level forces

Now we discuss whether the stable fiber-resonator couplings could be affected by other microscopic-level forces (e.g., the Casimir and van der Waals forces). To this end, we can describe this kinds of microscopic-level forces in our system as [S4]:

$$T_{\text{int}} = r_0 r \left[-\mathbb{A}/(6\pi h^3) + \mathbb{B}/(45\pi h^9) - \pi^2 c \hbar / (240 h^4) \right], \quad (\text{S88})$$

where we can calculate the Hamaker constant \mathbb{A} as [S57]:

$$\mathbb{A} = 3\varepsilon_-^{(1)}\varepsilon_-^{(2)}k_B T / \left[4\varepsilon_+^{(1)}\varepsilon_+^{(2)} \right] + \nu \left[\zeta_-^{(1)}\zeta_-^{(2)} \right]^2 / \left\{ \zeta_+^{(1)}\zeta_+^{(2)} \left[\zeta_+^{(1)} + \zeta_+^{(2)} \right] \right\}, \quad (\text{S89})$$

with the parameters $\varepsilon_{\pm}^{(u)}$, ν , and $\zeta_{\pm}^{(u)}$ being, respectively, defined as

$$\varepsilon_{\pm}^{(u)} = \varepsilon_u \pm \varepsilon_0, \quad \nu = 3\sqrt{2}\hbar\nu_e/16, \quad \zeta_{\pm}^{(u)} = \sqrt{\zeta_u^2 \pm \zeta_0^2}, \quad (\text{S90})$$

for $u = 1, 2$, where the parameters ζ_0 , ζ_1 , and ζ_2 are, respectively, used to denote the refractive index of the air, taper, and spinning silica microsphere. Moreover, the parameters ε_0 , ε_1 , and ε_2 are the dielectric constants of the air, taper, and spinning silica sphere, respectively. In addition, the parameter T is the temperature of the mechanical bath, and the parameter k_B is the Boltzmann constant. We should point out that for the convenience, the parameter ζ_2 is replaced with the parameter ζ in the main text. In addition, the constant parameter \mathbb{B} is typically of the order of 10^{-76} Jm^6 for couplings between condensed matter phases across the air or vacuum [S58]. Here other microscopic-level forces (e.g., the Casimir and van der Waals forces) are taken into account and then, we obtain the total force between the silica microsphere and the taper as:

$$\begin{aligned} T_{\text{total}} &= T_{\text{air}} + T_{\text{inte}} \\ &= 6.19\mu r^{5/2} \mathbf{S} \int_0^{r_0} (h - \sqrt{r_0^2 - x^2} + r_0)^{-3/2} dx + r_0 r \left[-\frac{\mathbb{A}}{6\pi h^3} + \frac{\mathbb{B}}{45\pi h^9} - \frac{\pi^2 c \hbar}{240 h^4} \right], \end{aligned} \quad (\text{S91})$$

where the first (second) term denotes the air pressure (microscopic-level forces, e.g., the Casimir and van der Waals forces). The critical coupling of light into the silica sphere is enabled via the self-adjustment behavior, whereby an optical drag identical in size but opposite in sign is experienced by the countercirculating light.

In our work, experimentally accessible parameters have been chosen [S59]. As a result, we can neglect other microscopic-level forces (e.g., the Casimir and van der Waals forces) owing to its negligibility, and it is still repulsive for the taper-resonator couplings. Therefore, we can safely omit the effects of the Casimir and van der Waals forces on the critical interactions. Moreover, the critical couplings may be also affected by other factors, e.g., the tapered-fiber stiffness, lubricant compressibility, and the wrap angle of a fiber, and while, we have confirmed that these factors can be negligible in practical experiments. Thus, in our all discussions, we can safely ignore these factors too [S4].

We here need to further emphasize that in the above, we detailedly study how the stable fiber-resonator couplings could be affected by other microscopic-level forces, in which we only consider the most representative forces: the Casimir and van der Waals forces [S60–S62]. In physics, the Casimir and van der Waals forces are two types of interactions at the microscopic level. Actually, the Casimir and van der Waals forces are commonly associated with the interactions between molecules, but they **are not limited** exclusively to molecules [S60–S62]. These forces can also act between atoms, non-conductive materials, and even larger structures. While molecular interactions are a typical context for the Casimir and van der Waals forces, it is important to note that they can extend beyond specific molecules [S60–S62].

In particular, we have emphasized that in our work, the effects of other microscopic-level forces (e.g., the Casimir and van der Waals forces) can be safely omitted for the critical coupling because they are negligible compared to the air-pressure force. To further demonstrate and elucidate its underlying physical mechanisms, we have conducted both numerical simulations and analytical analysis by choosing experimentally accessible parameters [S4, S59]. Based on these realistic state-of-the-art experimental conditions, we can see that other microscopic-level forces (e.g., the Casimir and van der Waals forces) can be safely ignored as they are negligible compared with the air-pressure force. Therefore, we can safely omit the effects of the Casimir and van der Waals forces on the critical interactions. Moreover, the critical couplings may also be affected by other factors, e.g., the tapered-fiber stiffness, lubricant compressibility, and the wrap angle of a fiber, and while, we have confirmed that these factors can be negligible in practical experiments. Thus, in our all discussions, we can safely ignore these factors too [S4]. In a word, the enhancement of the experimental analyses provide a better insight to experimentalists. By adding experimental analyses and numerical estimations with experimental accessible parameters, the relevance of our proposed phenomena under the state-of-the-art or near-future experimental conditions can be well confirmed.

In conclusion, we showed that the mass-immune and velocity-tunable topological one-way energy transfer arises from the Sagnac effect, without which it vanishes. We revealed that our approach is completely independent of the encircling directions of the EP, and this is usually impossible with all the conventional protocols. In particular, our simulations indicated that the threshold duration of the control loop for preserving the optimal one-way transfer of phonons can be easily prolonged but also shortened, which has no counterpart in previously reported demonstrations [S12–S26]. The study enables constructing novel topological chiral acoustics, with both device-mass tolerance and energy-transfer-velocity tunability.

VI. APPLICATION OF OUR APPROACH TO NON-HERMITIAN N -STATE SYSTEMS AND ITS COMBINATION WITH NON-ABELIAN NATURE

Here, we show how to implement the application of EP encircling-independent TPT, implemented through the Fizeau effect, to non-Hermitian three-state (or even N -state) systems, and to study the potential unique effects or phenomena arising from its combination with the non-Abelian nature inherent in such systems. In fact, our approach can be extended to a more general N -state system beyond the three-state case. Specifically, we here focus on an N -vibration optomechanical device, where N motional modes are coupled to a spinning optical-microsphere cavity [S1–S3], which is positioned close to a tapered region of a single-mode telecommunication fibre, as shown in Fig. S15. The evanescent coupling of light into this rotating configuration is induced by the tapered region of the fiber. Similarly, using the same coupler, light can be coupled out through the opposite side

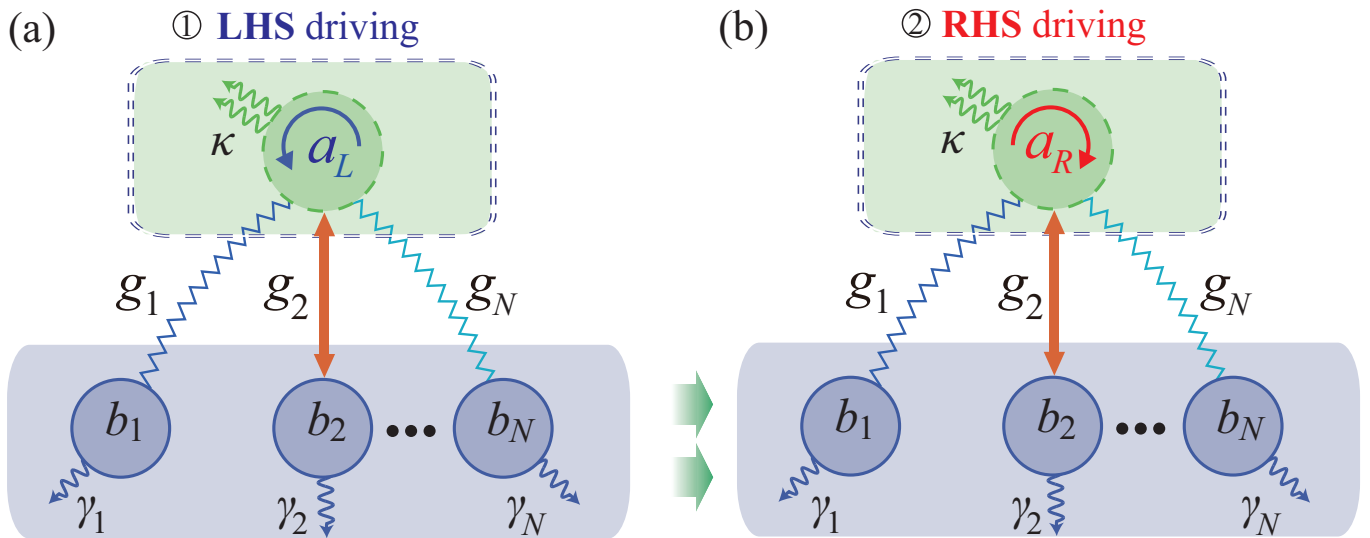


FIG. S15: Application of our method to non-Hermitian N -state systems. Schematic of the device consisting of a clockwise spinning silica-microsphere cavity $a_{R,L}$ (with angular velocity S and dissipation rate κ) coupled to N vibrations $b_{j=1,\dots,N}$ (with decay rates γ_j) through light-motion interactions g_j . The spinning microsphere is driven by a laser from the LHS or RHS of the fibre, yielding an anti-clockwise (a_L) or a clockwise (a_R) optical mode, respectively. (a,b) Simplified model diagrams for the case of the (a) LHS and (b) RHS drivings of the spinning microsphere.

of the fiber [S4]. As a result, each side of the fiber can simultaneously access both input and output ports. Depending on the input port, light circulates in the microsphere either clockwise or counterclockwise, leading to an optical mode a_R or a_L (with resonance frequencies $\omega_c^{R,L}$), respectively. The Hamiltonian of the spinning system is expressed as follows ($\hbar = 1$)

$$\mathcal{H}^l = \omega_c^l a_l^\dagger a_l + \sum_{j=1}^N [\omega_j b_j^\dagger b_j + g_j a_l^\dagger a_l (b_j^\dagger + b_j)] + i \sqrt{\kappa_{\text{in}}} \epsilon_{\text{in}} (a_l^\dagger e^{-i\omega_l t} - \text{H.c.}), \text{ for } l = R, L, \quad (\text{S92})$$

where b_j (b_j^\dagger) is the annihilation (creation) operator of the j th vibrational mode, with the resonance frequencies ω_j , for $j = 1, \dots, N$. The optomechanical interactions are denoted by the g_j terms, and the system driving is depicted by the $\epsilon_{\text{in}} = \sqrt{P/(\hbar\omega_l)}$ term, with κ_{in} (κ) denoting the input-coupling rate (linewidth) of the optical field and $P(\omega_l)$ being the power (frequency) of the laser. In the experimental setup, the aerodynamic process plays a crucial role in the interactions between the fiber and the resonator during rotation. This process draws air into the region between the sphere and tapered fiber, forming an air-lubrication layer in this region. The thin air film then allows the fiber to levitate a few nanometers above the sphere. Due to the “self-adjustment” process, the taper returns to its initial position when lifted higher than the stable equilibrium height by any perturbation. The critical coupling of light into the microsphere is facilitated by the “self-adjustment” effect, where countercirculating light experiences an optical drag of an identical size but an opposite sign. By adiabatically eliminating the optical mode, we can obtain an effective Hamiltonian for the non-Hermitian N -state systems.

Below, we analyze them in detail by illustrating the following two aspects:

(i) Applicability to non-Hermitian N -state systems: We expect to thoroughly study the application of EP encircling-independent TPT, facilitated by the Fizeau effect, to non-Hermitian N -state systems. We expect that in the non-Hermitian N -state systems, higher-order EPs can appear. In this N -state systems, symmetry and topology play a major role in classifying and protecting EPs, with the topological invariant associated to an EP being the eigenvalue braiding on an encircling loop in the space of Hamiltonian parameters, corresponding to an element of the non-Abelian braid group [S63–S65]. Our findings expect that this approach is indeed applicable in such systems, revealing a range of intriguing effects.

(ii) Integration with non-Abelian nature: We expect to study the non-Abelian braidings characterizing EPs in our non-Hermitian N -state systems, i.e., exceptional degeneracies can be distinguished from normal degeneracies through the braiding of eigenvalues on a loop enclosing the EP in parameter space [S63–S65]. In addition, we expect to study that the generalization is the braiding of N eigenvalues on a loop enclosing the N th order exceptional points, and that the non-Abelian braiding properties of exceptional lines in parameter space. Our results will demonstrate that the combination of EP encircling-independent TPT with the non-Abelian property leads to the emergence of additional unique effects, due to the combination of the Fizeau light-dragging effect and the non-Abelian braiding properties of exceptional lines in parameter space.

In summary, this study can open avenues for further exploration in the intersection of the Fizeau effect, non-Hermitian N -state systems, and non-Abelian nature, and contribute novel insights to the unique one-way topology. We believe the integration of

EP encircling-independent TPT with non-Hermitian N -state systems, particularly when combined with their non-Abelian nature, holds significant promise for future applications in topological physics. However, it seems that adequately addressing it would require a major and time-consuming revision of the paper. This can be the topic of our next paper, but not in this manuscript. Thus, this project is being done by us.

-
- [S1] G. Anetsberger, O. Arcizet, Q. P. Unterreithmeier, R. Rivière, A. Schliesser, E. M. Weig, J. P. Kotthaus, and T. J. Kippenberg, Near-field cavity optomechanics with nanomechanical oscillators, *Nature Physics* **5**, 909 (2009).
- [S2] M. Aspelmeyer, T. J. Kippenberg, and F. Marquardt, Cavity optomechanics, *Rev. Mod. Phys.* **86**, 1391 (2014).
- [S3] E. Gil-Santos, M. Labousse, C. Baker, A. Goetschy, W. Hease, C. Gomez, A. Lemaître, G. Leo, C. Ciuti, and I. Favero, Light-Mediated Cascaded Locking of Multiple Nano-Optomechanical Oscillators, *Phys. Rev. Lett.* **118**, 063605 (2017).
- [S4] S. Maayani, R. Dahan, Y. Kligerman, E. Moses, A. U. Hassan, H. Jing, F. Nori, D. N. Christodoulides, and T. Carmon, Flying couplers above spinning resonators generate irreversible refraction, *Nature (London)* **558**, 569 (2018).
- [S5] R. Fleury, D. L. Sounas, C. F. Sieck, M. R. Haberman, and A. Alù, Sound isolation and giant linear nonreciprocity in a compact acoustic circulator. *Science* **343**, 516 (2014).
- [S6] Z. Yang *et al.*, Topological acoustics. *Phys. Rev. Lett.* **114**, 114301 (2015).
- [S7] R. Huang, A. Miranowicz, J.-Q. Liao, F. Nori, and H. Jing, Nonreciprocal Photon Blockade *Phys. Rev. Lett.* **121**, 153601 (2018).
- [S8] Y.-F. Jiao, S.-D. Zhang, Y.-L. Zhang, A. Miranowicz, L.-M. Kuang, and H. Jing, Nonreciprocal Optomechanical Entanglement against Backscattering Losses, *Phys. Rev. Lett.* **125**, 143605 (2020).
- [S9] L. Xu, G. Xu, J. Huang, and C.-W. Qiu, Diffusive Fizeau Drag in Spatiotemporal Thermal Metamaterials *Phys. Rev. Lett.* **128**, 145901 (2022).
- [S10] G. C. Righini, Y. Dumeige, P. Féron, M. Ferrari, G. N. Conti, D. Ristic, and S. Soria, Whispering gallery mode microresonators: Fundamentals and applications, *Riv. Nuovo Cimento* **34**, 435 (2011).
- [S11] H. Jing, Ş. K. Özdemir, X.-Y. Lü, J. Zhang, L. Yang, and F. Nori, \mathcal{PT} -Symmetric Phonon Laser, *Phys. Rev. Lett.* **113**, 053604 (2014).
- [S12] H. Xu, D. Mason, L. Jiang, and J. G. E. Harris, Topological energy transfer in an optomechanical system with exceptional points, *Nature (London)* **537**, 80 (2016).
- [S13] J. Doppler, A. A. Mailybaev, J. Böhm, U. Kuhl, A. Girschik, F. Libisch, T. J. Milburn, P. Rabl, N. Moiseyev, and S. Rotter, Dynamically encircling an exceptional point for asymmetric mode switching. *Nature (London)* **537**, 76 (2016).
- [S14] H. Ren, T. Shah, H. Pfeifer, C. Brendel, V. Peano, F. Marquardt, and O. Painter, Topological phonon transport in an optomechanical system, *Nat. Comm.* **13**, 3476 (2022).
- [S15] M. Abbasi, W. Chen, M. Naghiloo, Y. N. Joglekar, and K. W. Murch, Topological Quantum State Control through Exceptional-Point Proximity, *Phys. Rev. Lett.* **128**, 160401 (2022).
- [S16] A. U. Hassan, B. Zhen, M. Soljačić, M. Khajavikhan, and D. N. Christodoulides, Dynamically encircling exceptional points: exact evolution and polarization state conversion. *Phys. Rev. Lett.* **118**, 093002 (2017).
- [S17] H. Wang, S. Assaworarat, S. Fan, Dynamics for encircling an exceptional point in a nonlinear non-Hermitian system. *Opt. Lett.* **44**, 638 (2019).
- [S18] A. U. Hassan, G. L. Galmiche, G. Harari, P. LiKamWa, M. Khajavikhan, M. Segev, and D. N. Christodoulides, Chiral state conversion without encircling an exceptional point. *Phys. Rev. A* **96**, 052129 (2017).
- [S19] Q. Zhong, M. Khajavikhan, D. N. Christodoulides, and R. El-Ganainy, Winding around non-Hermitian singularities. *Nat. Commun.* **9**, 4808 (2018).
- [S20] J. Feilhauer, A. Schumer, J. Doppler, A. A. Mailybaev, J. Böhm, U. Kuhl, N. Moiseyev, and S. Rotter, Encircling exceptional points as a non-Hermitian extension of rapid adiabatic passage. *Phys. Rev. A* **102**, 040201(R) (2020).
- [S21] H. Nasari, G. Lopez-Galmiche, H. E. Lopez-Aviles, A. Schumer, A. U. Hassan, Q. Zhong, S. Rotter, P. LiKamWa, D. N. Christodoulides, and M. Khajavikhan, Observation of chiral state transfer without encircling an exceptional point, *Nature (London)* **605**, 256 (2022).
- [S22] I. I. Arkhipov, A. Miranowicz, F. Minganti, Ş. K. Özdemir, and F. Nori, Dynamically crossing diabolic points while encircling exceptional curves: A programmable symmetric-asymmetric multimode switch, *Nat. Commun.* **14**, 2076 (2023).
- [S23] R. Uzdin, A. Mailybaev, and N. Moiseyev, On the observability and asymmetry of adiabatic state flips generated by exceptional points. *J. Phys. A* **44**, 435302 (2011).
- [S24] E.-M. Graefe, A. A. Mailybaev, and N. Moiseyev, Breakdown of adiabatic transfer of light in waveguides in the presence of absorption. *Phys. Rev. A* **88**, 033842 (2013).
- [S25] Y. Choi, C. Hahn, J. W. Yoon, S. H. Song, and P. Berini, Extremely broadband, on-chip optical nonreciprocity enabled by mimicking nonlinear anti-adiabatic quantum jumps near exceptional points. *Nat. Commun.* **8**, 14154 (2017).
- [S26] J. W. Yoon *et al.*, Time-asymmetric loop around an exceptional point over the full optical communications band. *Nature (London)* **562**, 86 (2018).
- [S27] H. Ramezani, P. K. Jha, Y. Wang, and X. Zhang, Nonreciprocal Localization of Photons, *Phys. Rev. Lett.* **120**, 043901 (2018).
- [S28] *Spin Wave Confinement: Propagating Waves*, ed. S. O. Demokritov (CRC Press, Singapore, 2017).
- [S29] F. Minganti, A. Miranowicz, R. W. Chhajlany, and F. Nori, Quantum exceptional points of non-Hermitian Hamiltonians and Liouvillians: The effects of quantum jumps, *Phys. Rev. A* **100**, 062131 (2019).
- [S30] B. Peng, Ş. K. Özdemir, S. Rotter, H. Yilmaz, M. Liertzer, F. Monifi, C. M. Bender, and F. Nori, L. Yang, Loss-induced suppression and revival of lasing, *Science* **346**, 328 (2014).
- [S31] B. Peng, Ş. K. Özdemir, F. Lei, F. Monifi, M. Gianfreda, G. Lu Long, S. Fan, F. Nori, C. M. Bender, and L. Yang, Parity-time-symmetric

- whispering-gallery microcavities, *Nat. Phys.* **10**, 394 (2014).
- [S32] Ş. K. Özdemir, S. Rotter, F. Nori, and L. Yang, Parity-time symmetry and exceptional points in photonics, *Nat. Mater.* **18**, 783 (2019).
- [S33] T. Kuang, R. Huang, W. Xiong, Y. Zuo, X. Han, F. Nori, C.-W. Qiu, H. Luo, H. Jing, and G. Xiao, Nonlinear multi-frequency phonon lasers with active levitated optomechanics, *Nat. Phys.* **9**, 1444 (2023).
- [S34] A. Youssefi, S. Kono, A. Bancora, M. Chegnizadeh, J. Pan, T. Vovk, and T. J. Kippenberg, Topological lattices realized in superconducting circuit optomechanics, *Nature (London)* **612**, 666 (2022).
- [S35] J. Hofer, A. Schliesser, and T. J. Kippenberg, Cavity optomechanics with ultrahigh-Q crystalline microresonators, *Phys. Rev. A* **82**, 031804(R) (2010).
- [S36] Note that more than 20 mechanical modes with the vibrational frequencies ranging from approximately 500 kHz to 2 MHz were experimentally observed using a ultrahigh-Q crystalline microresonator [S35].
- [S37] H. Xu, L. Jiang, A. A. Clerk, and J. G. E. Harris, Nonreciprocal control and cooling of phonon modes in an optomechanical system, *Nature (London)* **568**, 65 (2019).
- [S38] M. Bhattacharya and P. Meystre, Multiple membrane cavity optomechanics, *Phys. Rev. A* **78**, 041801(R) (2008).
- [S39] T. J. Kippenberg and K. J. Vahala, Cavity optomechanics: Back-action at the mesoscale, *Science* **321**, 1172 (2008).
- [S40] P. Meystre, A short walk through quantum optomechanics, *Ann. Phys. (Berlin)* **525**, 215 (2013).
- [S41] F. Massel, T. T. Heikkilä, J.-M. Pirkkalainen, S. U. Cho, H. Saloniemi, P. J. Hakonen, and M. A. Sillanpää, Microwave amplification with nanomechanical resonators, *Nature (London)* **480**, 351 (2011).
- [S42] F. Massel, S. U. Cho, J.-M. Pirkkalainen, P. J. Hakonen, T. T. Heikkilä, and M. A. Sillanpää, Multimode circuit optomechanics near the quantum limit, *Nat. Commun.* **3**, 987 (2012).
- [S43] C. F. Ockeloen-Korppi, M. F. Gely, E. Damskägg, M. Jenkins, G. A. Steele, and M. A. Sillanpää, Sideband cooling of nearly degenerate micromechanical oscillators in a multimode optomechanical system, *Phys. Rev. A* **99**, 023826 (2019).
- [S44] C. F. Ockeloen-Korppi, E. Damskägg, J.-M. Pirkkalainen, M. Asjad, A. A. Clerk, F. Massel, M. J. Woolley, and M. A. Sillanpää, Stabilized entanglement of massive mechanical oscillators, *Nature (London)* **556**, 478 (2018).
- [S45] L. M. de Lépinay, C. F. Ockeloen-Korppi, M. J. Woolley, and M. A. Sillanpää, Quantum mechanics-free subsystem with mechanical oscillators, *Science* **372**, 625 (2021).
- [S46] X. Jiang, Q. Lin, J. Rosenberg, K. Vahala, and O. Painter, *Opt. Express* **17**, 20 911 (2009).
- [S47] Q. Lin, J. Rosenberg, X. Jiang, K. Vahala, and O. Painter, *Phys. Rev. Lett.* **103**, 103601 (2009).
- [S48] G. S. Wiederhecker, L. Chen, A. Gondarenko, and M. Lipson, *Nature (London)* **462**, 633 (2009).
- [S49] M. Eichenfield, R. Camacho, J. Chan, K. J. Vahala, and O. Painter, *Nature (London)* **459**, 550 (2009).
- [S50] Y.-G. Roh, T. Tanabe, A. Shinya, H. Taniyama, E. Kuramochi, S. Matsuo, T. Sato, and M. Notomi, *Phys. Rev. B* **81**, 121101(R) (2010).
- [S51] R. Reimann, M. Doderer, E. Hebestreit, R. Diehl, M. Frimmer, D. Windey, F. Tebbenjohanns, and L. Novotny, GHz Rotation of an Optically Trapped Nanoparticle in Vacuum, *Phys. Rev. Lett.* **121**, 033602 (2018).
- [S52] J. Ahn, Z. Xu, J. Bang, Y.-H. Deng, T. M. Hoang, Q. Han, R.-M. Ma, and T. Li, Optically Levitated Nanodumbbell Torsion Balance and GHz Nanomechanical Rotor, *Phys. Rev. Lett.* **121**, 033603 (2018).
- [S53] W. A. Gross *et al.* *Fluid Film Lubrication* (John Wiley and Sons, New York, 1980).
- [S54] W. A. Gross, *Gas Film Lubrication* (Wiley, New York, 1962).
- [S55] W. F. Busse and W. H. Denton, Water-lubricated soft-rubber bearings, *Trans. Am. Soc. Mech. Eng.* **54**, 3 (1932).
- [S56] H. Blok and J. J. Van Rossum, The foil bearing—a new departure in hydrodynamic lubrication, *Lubr. Eng.* **9**, 316 (1953).
- [S57] J. Chen, G. Zhou, L. Zhang, and W. Sun, Influence of Intermolecular Force on the Head-Disk Interface of HDD with High Recording Density, in *2009 Symposium on Photonics and Optoelectronics* (IEEE, 2009) pp. 1-4.
- [S58] L. Wu and D. B. Bogy, Effect of the Intermolecular Forces on the Flying Attitude of Sub-5 NM Flying Height Air Bearing Sliders in Hard Disk Drives, *J. Tribol.* **124**, 562 (2002).
- [S59] R. J. Joyce, H. F. Sterling, and J. H. Alexander, Silicon oxide and nitride films deposited by an r.f. glow-discharge, *Thin Solid Films* **1**, 481 (1968).
- [S60] M. Bordag, G. L. Klimchitskaya, U. Mohideen, and V. M. Mostepanenko, *Advances in the Casimir effect*, Advances in the Casimir Effect, Oxford University Press (2009).
- [S61] M. Kardar and R. Golestanian, The ‘friction’ of vacuum, and other fluctuation-induced forces, *Reviews of Modern Physics*, **71**, 1233-1245 (1999).
- [S62] V. A. Parsegian, *Van der Waals Forces: A Handbook for Biologists, Chemists, Engineers, and Physicists*, Cambridge University Press (2006).
- [S63] K. Ding, C. Fang, and G. Ma, Non-hermitian topology and exceptional-point geometries, *Nature Reviews Physics* **4**, 745-760 (2022).
- [S64] P. Delpierre, T. Yoshida, and Y. Hatsugai, Symmetry protected multifold exceptional points and their topological characterization, *Phys. Rev. Lett.* **127**, 186602 (2021).
- [S65] K. Kawabata, T. Bessho, and M. Sato, Classification of exceptional points and non-hermitian topological semimetals, *Phys. Rev. Lett.* **123**, 066405 (2019).